Nanostructure and Nanomechanics of Collagen Self-Assemblies

by

©Chuan Xu

A Dissertation submitted to the School of Graduate Studies in partial fulfillment of the requirements for the degree of

Doctor of Philosophy

Department of Chemistry

Memorial University of Newfoundland

May, 2014

St. John's Newfoundland

Abstract

This thesis outlines the development and application of methods for characterization of nanostructured biomaterials, specifically, collagen. Collagen is the most abundant protein in the human body and plays an important structural role. Therefore, research on the structural and mechanical properties of this protein is beneficial for disease treatment and health improvement, including the development of new materials for bioengineering. These newly developed techniques and methods demonstrated their merit in this research. They can potentially find the way to applications in broader areas, e.g. bio-engineering, medical science, nano technology and industry.

A novel method called minimum indentation, which I developed, extracts the mechanical properties of superficial layers or nanometer scale objects in a sample with high precision. This is a true surface measurement with a detection depth of less than 10 nanometers. During sample testing, an atomic force microscope (AFM) tip jumps to contact with the sample surface when the tip-sample attractive force gradient increases and exceeds the cantilever spring constant. The jump-to-contact distance is determined by the sample mechanical properties and tip-sample surface adhesion. Hence proper interpretation of the jump-to-contact phenomenon yields sample surface mechanical properties. I present different models to suit for hydrophilic and hydrophobic surfaces.

The minimum indentation method requires a different treatment in the presence

of strong capillary effects. I develop this in the context of a study of segment-long-spacing collagen crystallites (SLS). A combination of morphological and nanomechanical data yields a more complete picture of SLS nanostructure, including proposed growth mechanism and internal structure.

Nanoidentation and persistence length are different methods to access complementary mechanical information. I apply them to investigate the fibrillogenosis of type I and type II collagens, demonstrating distinct growth stages and structure transition phenomena. Type I collagen fibrils are much longer than type II collagen fibrils and present different internal structures, with consequently different mechanical properties.

Acknowledgements

First of all, I would like to give my sincere appreciation to my supervisor and mentor Dr. Erika Merschrod. She is the person who brought me here in the first place and introduced me into this multidisciplinary area. She is patient and always takes her time to guide me through the projects and teach me LaTeX. She trusts me and gives me freedom to explore new areas. She is brilliant, thoughtful and considerate, I benefit tremendously from both of her academical and non-academical advice. She is also supportive and generous. With her support, I attended several national and international conferences. I feel real lucky to work with her.

I am deeply grateful to my supervisory committee members Dr. Travis Fridgen and Dr. Peter Warburton. They spent valuable time to evaluate my progress and gave me advice during supervisory committee meetings and comprehensive exam. They also read through my thesis and offered me great suggestion.

I owe my candid thanks to Dr. Nancy Forde from Simon Fraser University for providing us valuable type II collagen samples. This makes the type I and II collagen comparison study possible and forms a indispensable part of my thesis.

I would like to take this opportunity to say thanks to my group members, Ramesh Kumar Mani, Behrang Moazez, Shaheen Fathima, Alina Stetco, Ant Muyi Xu, Jordon Keats, Lawson Miller, Liam Whelan, Tiber Reardon, Munmun Sarkar, M. Majibur Rahman, Sepideh Mehrani and Jiaqi Cheng from Dr. Kristin M. Poduska's group for sharing their wisdom, providing suggestions and helping me in the lab.

I feel indebted to my families, my wife Xueqin Kou, my daughter Meijia Xu, my mother Ping Cao, my father Shaoyun Xu, my sister Yan Xu and other relatives. Their endless love, support and encourage fill my life with joys, delight and cheers, help me to overcome difficulties and challenges and make me a better man.

Last but not lest, I would like to express gratitude to Department of Chemistry, Memorial University of Newfoundland, Canadian Institutes of Health Research (CIHR), Canada Foundation for Innovation (CFI) and the Natural Sciences and Engineering Research Council of Canada (NSERC) for their financial support.

Table of Contents

List of Tables

List of Figures

Chapter 1

Introduction*

1.1 Application of Force Spectroscopy Methods to the Study of Biomaterials

Characterization tools from surface science are increasingly applied to study systems beyond traditional inorganic thin films. These techniques can shed new light on structure and properties of proteins, keeping in mind the caveat that the proteins must be surface bound or otherwise interfacially confined, if only momentarily at the time of detection. Interfacial interactions can impact the structure of the proteins being studied,[1] but there are of course many protein systems that are inherently interfacial since surfaces and interfaces abound in biology. Protein-based materials are often in thin-film form as in bioactive coatings,[2] and biofilm formation is an important area of fundamental as well as applied biology.[3] Therefore, there are significant opportu-

---

*Portions of this chapter have been published as "Application of Force Spectroscopy Methods to the Study of Biomaterials", Chuan Xu and Erika F. Merschrod S., in *Proteins in Solution and at Interfaces: Methods and Applications in Biotechnology and Materials Science* (eds J. M. Ruso and A. Piñeiro), John Wiley and Sons: Hoboken NJ, 2013. Chuan Xu performed the literature review, developed the concepts, prepared the first draft of the chapter, and revised the chapter with feedback from the co-author.

nities for the fruitful application of surface characterization techniques to the study of proteins.

One method finding increasing use in the study of proteins is nanoindentation, particularly when coupled with atomic force microscopy. In this chapter, I outline several approaches to measuring and analyzing nanoindentation data, with an emphasis on applications to protein-based biomaterials (both artificial and natural). I present and explain equations where necessary, but my approach is primarily conceptual and I illustrate all methods with examples related to protein-based systems. I also provide links to articles and books with more details about the measurement and modeling of nanoindentation data.

Indentation tests are commonly used in materials engineering to determine sample mechanical properties, by investigating the deformation of a material under an indenter. Table 1.1 lists the characteristics of four classes of indentation techniques: traditional indentation, depth sensing indentation, nanoindentation, and atomic force microscopy (AFM) nanoindentation. Although their instrumentation varies dramatically, the methods share the same principle: by measuring or calculating the force applied, the indentation depth, and the indenter shape, the mechanical properties of the samples can be deduced. The applications to biological structures are many; we provide a few representative examples in this chapter.

One major difference between traditional indentation and depth sensing indentation is the way to determine indentation depth. Traditional indentation depth is calculated from the residual indentation pattern after indentation by microscopic imaging while depth sensing indentation can sense the indentation depth when the indentation is taking place. Nanoindentation employs almost the same approach as depth sensing indentation. It can measure mechanical properties at the nanometer scale by utilizing supersharp indenters (around several nanometers in radius). The

Table 1.1: Characteristics of four types of indentation techniques

	Traditional indentation	Depth sensing indentation	Nanoindentation	AFM nanoindentation
indenter size	micrometre	micrometre	nanometre	nanometre
contact area detection	microscope image	calculated from indentation depth	calculated from indentation depth	calculated from indentation depth
load	micronewton	micronewton	nanonewton	nanonewton
indent visualization	microscope	microscope	SEM, TEM, AFM	AFM

indentation pattern created by such supersharp tips is too tiny to measure at high accuracy, thus requiring depth sensing measurements during indentation.

This high-resolution nanoindentation has very practical applications, particularly for biological systems. For example, nanoindentation can measure the mechanical properties of very tiny objects like cells,[4] collagen fibrils,[5] proteins, and even viruses.[6] AFM-aided nanoindentation takes the nanoindentation technique to a whole new level, where the same probe is used to image the sample and to carry out the indentation measurement. With AFM, a nanometer resolution image of the sample surface is taken first. Then based on that image, one can decide which location(s) to indent. After indentation, another image can be taken at the same place to check the impact of the indentation. This visualization process is very controllable and reliable at nanometer precision.

Indentation and nanoindentation are based on contact mechanics. Contact mechanics is the study of the material mechanical properties like elasticity, plasticity, or viscoelasticity in contact.[7] There are many different ways to model the interactions or contacts between two approaching objects. They can be divided into two categories: nonadhesive methods and adhesive methods. The former treat the contact as rigid

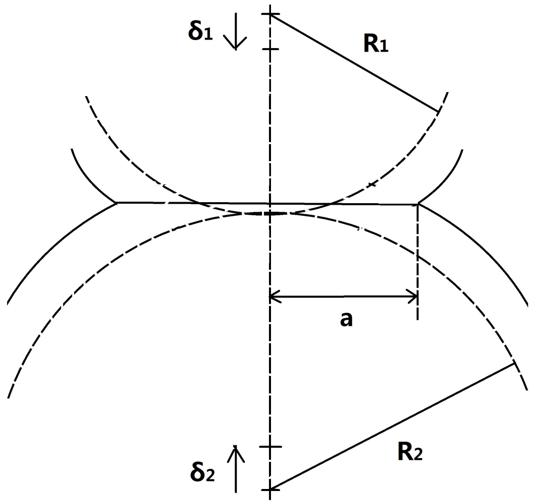

Figure 1.1: The contact geometry between two spheres. Spheres 1 and 2 have radii of R_1 and R_2 respectively. The dashed partial circles represent the point where the two spheres make contact. After the point of contact, the total displacement is the sum of sphere 1 displacement and sphere 2 displacement: $\delta = \delta_1 + \delta_2$. The contact between the two spheres forms a circle with a radius of a, called the contact radius.

without intermolecular forces, while the latter consider intermolecular forces at short distance.

1.2 Nonadhesive Methods

Nonadhesive methods are applied when the samples are rigid, so the adhesive force is very small compared with the total force applied. Hard materials like metal, glass, and hard tissues (*e.g.*, bone, dentin, cartilage) are usually treated by this method. Soft materials like plastics, rubber, soft tissues (*e.g.*, cell, collagen fibril, membrane) are sometimes also treated by this method, since ignoring the adhesive contributions can simplify the analysis.

1.2.1 Hertz Model and Sneddon Expansion

The study of contact mechanics can be traced back to the 19th century, when Hertz published his paper “On the contact of elastic solids”.[8] In that paper, Hertz deduced the pressure distribution on the deformed contact surface between two spheres (see Figure 1.1, sphere 1 and sphere 2 with Young’s moduli E_1 and E_2, Poisson’s ratios ν_1 and ν_2 and radii R_1 and R_2, respectively). Poisson’s ratio is the ratio of the transverse strain (normal to the load) to the axial strain (along the load). Poisson’s ratios for biomaterials are always around 0.2 to 0.5.[9–11]

Hertz related the load (F, the amount of force applied to the two spheres) to the displacement (δ) of the two spheres by introducing the reduced modulus (E^*):[12]

$$F = \left(\frac{16RE^{*2}\delta}{9}\right)^{\frac{3}{2}} \tag{1.1}$$

R is the effective radius defined as

$$\frac{1}{R} = \frac{1}{R_1} + \frac{1}{R_2} \tag{1.2}$$

Young’s moduli (E_1 and E_2 for sphere 1 and sphere 2, respectively) are related to the reduced modulus (E^*) by

$$\frac{1}{E^*} = \frac{(1-\nu_1^2)}{E_1} + \frac{(1-\nu_2^2)}{E_2} \tag{1.3}$$

Alternatively, the Hertz model can be expressed by relating the contact radius a to the load:

$$a = \frac{3RF}{4E^*} \tag{1.4}$$

From Hertz’s deduction (Equations 1.1 and 1.3), the Young’s modulus of a material (with known Poisson's ratio) can be calculated by pressing it against a material with known Young's modulus and Poisson's ratio. This method for elasticity determination is called the Hertzian model. The Hertzian model is directly used when the sample and indenter can both be treated as spheres with similar diameters.

Using this Hertzian approach, Jin-Won Park[13] found the Young's modulus of negatively charged glycosphingolipid sulfatide vesicles to be around 75×10^6 Pa. In the Hertzian model, the deformation of the half sphere in contact with the indenter is used for the calculation. In the vesicle calculations, the deformation of the whole vesicle was used, however, which lead to overestimate of the Young's modulus due to substrate effect. Other errors in applying the Hertzian model to this system come from the fact that the vesicle would not be a perfect sphere when it sticks to the substrate surface. Van der Waals forces and other forces will deform the vesicle, especially as it is soft. These deformation phenomena are addressed in Section 1.3 (*e.g.*, with the JKR model in Section 1.3.1). These inaccuracies can also be addressed by finite element models (Section 1.5).

In the indentation tests, the samples and indenters may not necessarily be spherical. In fact, samples are often flat while indenters may be cylindrical, conical or pyramidal (*e.g.*, Berkovich or Vickers indenters).[8] In these cases, Sneddon expanded the Hertzian model by deriving a more general form for load-displacement ($F - \delta$) relationship:[14]

$$F \propto \delta^m \tag{1.5}$$

In the indentation m is a constant depending on the indenter shape, with $m = 1$ for a cylindrical indenter, $m = 1.5$ for a spherical indenter, and $m = 2$ for a conical indenter.[15] If the sample surface is isotropic, flat, homogeneous, and semi-infinitely large, and the indenter is axisymmetrical, Sneddon showed that there is a simple relationship between the reduced elasticity (E^*) and the stiffness (S) at the beginning of the unloading force curve:[14]

$$S = \frac{dF}{d\delta} = \frac{2\sqrt{A}}{\sqrt{\pi}} E^* \tag{1.6}$$

A is the projected area of contact between the sample and indenter and could be obtained by imaging the residual indent after indentation. However, the contact area at loading is not exactly the same as the residual area after loading due to elastic recovery after loading (see Figure 1.2a). A can also be calculated from the contact indentation depth (h_c, as defined in Figure 1.2) if the geometry of the indenter is known, but the contact depth can be even harder to measure directly. Doerner and Nix, and Oliver and Pharr extract the contact depth from indentation depth at maximum load ($h_{\max}$, as defined in Figure 1.2), and this is described in the next section.

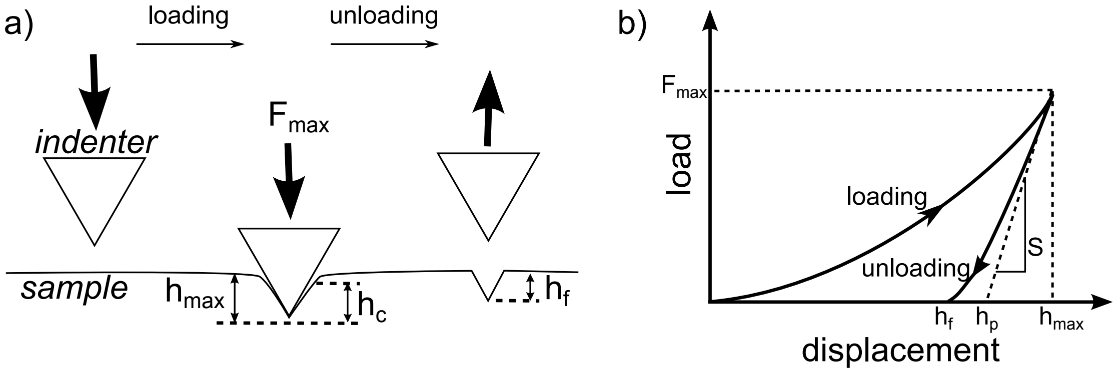

Figure 1.2: a) Indentation process showing deformation and subsequent elastic recovery. b) Corresponding schematic loading and unloading curves.

1.2.2 Doerner-Nix and Oliver-Pharr Models

From Figure 1.2 we can see that after the indenter is pulled off the sample, a permanent indent is left as a result of plasticity. Hardness (H) is introduced to account for this property:

$$H = \frac{F_{\max}}{A_{\max}} \tag{1.7}$$

$F_{\max}$ is the maximum load and $A_{\max}$ is the projection of contact area at maximum load. $A_{\max}$ can be measured by imaging the residual indent. Because of plasticity shown above and the viscous properties (Section 1.4) of the material, the indentation depth is not the contact depth. Based on Sneddon's solution for the Vickers indenter, Doerner and Nix deduced that the contact area can be calculated from the plastic depth (h_p).[16]

$$S = \frac{1}{2h_p E_r}\left(\frac{\pi}{24.5}\right)^{\frac{1}{2}} \tag{1.8}$$

$$h_c = h_{\max} - \frac{F_{\max}}{S} \tag{1.9}$$

h_p is the intercept of the line tangent to the maximum load of the unloading force curve (Figure 1.2b).

Oliver and Pharr made a slight change to the contact depth at maximum load (h_c) to account for different tip shapes:

$$h_c = h_{\max} - \varepsilon\frac{F_{\max}}{S} \tag{1.10}$$

Therefore, the fundamental difference between the Doerner-Nix and Oliver-Pharr methods is the way the contact depth is calculated (Equations 1.9 and 1.10). The factor ε is introduced in Oliver and Pharr's method to account for the effect of indenter geometry: $\varepsilon = 0.72$, 0.75, and 1 for conical, spherical, and cylindrical indenter, respectively.[17] In either case, h_c is then used to calculate the contact area A and the Sneddon equation (Equation 1.6) can be solved for the reduced modulus.

The Oliver-Pharr method is widely used for its simplicity and accuracy. For example, it has been applied to study tooth enamel, a very hard material primarily composed of hydroxyapatite (HAp). He and Swain used this method to find Young's modulus of human tooth enamel to be 105.5 ± 3 GPa.[18] Darnell found that the tooth enamel of *Alouatta palliata* (a type of monkey) has a much lower Young's modulus mostly due to the young age.[19] Other studies have recorded decreases in Young's moduli of enamel repaired with amorphous calcium phosphate[20] or treated with hydrogen peroxide (which exists in some tooth bleaching agents).[21] Yeau-Ren Jeng *et al.* found that NaF (which exists in anticaries agents) has a minor effect on enamel elasticity[22] although it reacts with HAp to form amorphous calcium fluoride.

The Oliver-Pharr method has also been applied to a softer class of materials based on type I collagen. Type I collagen fiber bundles form the substrate for HAp mineralization in dentin and bone. Kumar *et al.* found that dried type I collagen films have Young's moduli ranging from 0.2 to 3 GPa,[23] while Wenger *et al.* found that individual type I collagen fiber Young's moduli are between 5 and 11.5 GPa.[5] The discrepancies may relate to the different higher-order structure in the two systems; Wenger's work measures individual fibers whereas Kumar's measurements reflect the mechanical response of a fiber network.

Another interesting phenomenon is that Young's moduli for bones fall just between those of their two major components: HAp and type I collagen. A number of studies have applied the Oliver-Pharr method to study effects of hormones,[24] disease,[25] age,[26] and bone type[27] on bone mechanical properties. Despite their differences, all of these studies suggest that bones have very similar Young's moduli (between 15 and

25 GPa) regardless of their origin. This can be attributed to the facts that all the bones share the same two major components – collagen and HAp – and they have similar hierarchical structures.

Soft samples from animals and plants are also interesting subjects for study and have been approached using the Oliver-Pharr method. Müller investigated the range of mechanical properties of structures in insect cuticle (exoskeletal components) and found that components of the gula (head-neck joint) of *Pachnoda marginata* (a beetle) have Young's moduli between 5 and 10 GPa.[28] Scholz studied the toe pad epithelium of a tree frog and found that the mean value of effective elastic modulus is 14 MPa.[29] These two materials are several orders of magnitude different in terms of Young's moduli. These differences are essential for their functions: the stiff gula is good protection for insects while soft toe pad epithelium helps the tree frog stick on trees.

1.3 Adhesive Methods

Hertz's model and other methods for determining material properties are sufficient when the contact is between two rigid surfaces and the applied force is high. The adhesive force is too small to be accounted for compared with the force applied. When at least one of the two contact surfaces is soft and the applied force is low, then adhesive forces (*e.g.*, van der Waals force) between the two contact surfaces cannot be neglected. This can be seen from the force curve in Figure 1.3.

When the indenter approaches the sample, the tip is attracted to the sample surface, so the measured force increases negatively (point A in Figure 1.3). After the sample and indenter come into contact, the measured force increases during the rest of the loading point. At point B, the indenter begins to retract. The hysteresis between the subsequent unloading segment and the previous loading segment is most

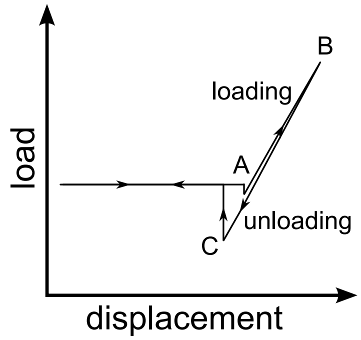

Figure 1.3: Schematic force curve showing significant adhesion effects at A and C. For comparison, the force curves from Figure 1.2b would fall in the right-hand region of this plot (large displacement of the indenter).

dramatic at C, where adhesion between the sample and the indenter again causes the measured force to increase negatively.

The surface energy (U_s) is related to the work of adhesion ($\Delta\gamma$) and the interacting area (A) by Equation 1.11.

$$U_s = \Delta\gamma A \tag{1.11}$$

$\Delta\gamma$ can be calculated by Equation 1.12.

$$\Delta\gamma = \gamma_1 + \gamma_2 - \gamma_{12} \tag{1.12}$$

Where γ_1 is the indenter surface energy, γ_2 is the sample surface energy and γ_{12} is the indenter-sample surface energy. Because of sample deformation during loading, the contact area upon retraction is larger than upon loading. Therefore, at the same indentation depth, the adhesive force during unloading is larger than that during loading.

The significant presence of van der Waals forces in the force curve necessitates the inclusion of adhesive forces in analyzing the indentation data. Several models are

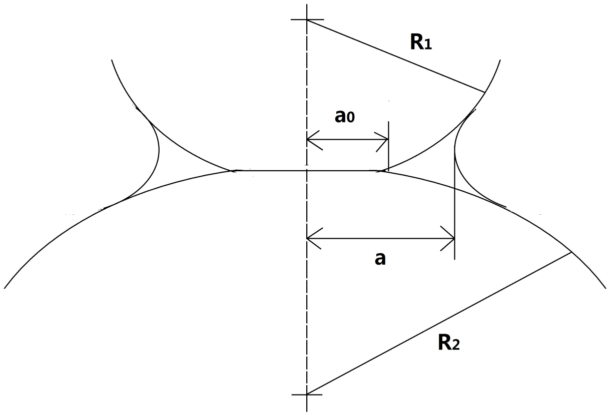

Figure 1.4: The contact geometry between two spheres when adhesion is considered. The adhesion force results in a larger actual contact radius a than the nominal contact radius a_0.

available such as the JKR, Bradley, DMT, MD, and COS models described below.

1.3.1 JKR Model

Johnson, Kendall, and Roberts proposed a model to include short-range adhesive forces in the Hertzian contact.[30] They suggested that the actual contact radius (a_1) under force F_0 is larger than that calculated from Hertzian model (a_0) because of deformation due to adhesion. Furthermore, they recognized that this adhesion and deformation lead to tensile forces near the edge of the contact area in addition to the compressive forces at the center of the contact between sample and indenter. All this results in a larger apparent load F_1 if one assumes a Hertzian contact area and also explains the negative load ("pull-off force") during retraction. By quantifying the adhesive contributions to the load-displacement curve one can more accurately extract the mechanical data, and one can also access important material properties such as adhesion energies from said pull-off force.

Considering the adhesion force, the contact between two spheres is illustrated in Figure 1.4. When two elastic spheres are pressed against each other by a force F_0, the total energy (U$_t$, Equation 1.13) is the sum of elastic storage energy (U$_e$, Equation 1.14), mechanic energy (U$_m$, Equation 1.15) and surface energy (U$_s$, Equation 1.16):

$$U_t = U_e + U_m + U_s \tag{1.13}$$

$$U_e = \frac{1}{(\frac{4}{3}E^*)^{\frac{2}{3}} R^{\frac{1}{3}}} (\frac{1}{15} F_1^{\frac{5}{3}} + \frac{1}{3} {F_0}^2 F_1^{-\frac{1}{3}}) \tag{1.14}$$

$$U_m = -\frac{1}{(\frac{4}{3}E^*)^{\frac{2}{3}} R^{\frac{1}{3}}} (\frac{1}{3} F_0 F_1^{\frac{2}{3}} + \frac{2}{3} F_0^2 F_1^{-\frac{1}{3}}) \tag{1.15}$$

$$U_s = -\Delta\gamma\pi \frac{R^{\frac{2}{3}} F_1^{\frac{2}{3}}}{(\frac{4}{3}E^*)^{\frac{2}{3}}} \tag{1.16}$$

$\Delta\gamma$ is the work of adhesion. At equilibrium the following relationship should apply:

$$\frac{dU_t}{dF_1} = 0 \tag{1.17}$$

This gives us the actual contact force (F$_1$) at the load force F$_0$

$$F_1 = F_0 + 3\Delta\gamma\pi R + \sqrt{6\Delta\gamma\pi R F_0 + (3\Delta\gamma\pi R)^2} \tag{1.18}$$

Compared to the generalized Hertz equation ($a_0^3 = \frac{3R}{4E^*} F_0$), this equation can be rewritten as:

$$a^3 = \frac{3R}{4E^*} (F_0 + 3\Delta\gamma\pi R + \sqrt{6\Delta\gamma\pi R F_0 + (3\Delta\gamma\pi R)^2}) \tag{1.19}$$

From Equation 1.19, the contact radius is the smallest when the load force F_0 satisfies the following condition:

$$6\Delta\gamma\pi R F_0 + (3\Delta\gamma\pi R)^2 = 0 \tag{1.20}$$

Solving this equation, the loading force to maintain the smallest contact radius is obtained:

$$F_0 = -\frac{3}{2}\pi\Delta\gamma R \tag{1.21}$$

A negative sign means the load should be a pull off force to get the smallest contact radius. So if a pull off force $> \frac{3}{2}\pi\Delta\gamma R$ is applied, the smallest contact radius can't be maintained and the two spheres will be separate. $\frac{3}{2}\pi\Delta\gamma R$ thus is the smallest force needed to separate the two spheres.

According to Equation 1.19, the critical contact radius (a_c) at separation can also be calculated:

$$a_c^3 = \frac{9R^2\Delta\gamma\pi}{8E^*} \tag{1.22}$$

Based on the geometry of the indenter shape, for weak adhesion (where the indentation depth caused by adhesion is small), the critical indention depth is

$$d_c = \frac{a_c^2}{R} = (\frac{9}{8})^{\frac{2}{3}}(\Delta\gamma)^{\frac{2}{3}}(\frac{\pi^{\frac{2}{3}}R^{\frac{1}{3}}}{E^{*\frac{2}{3}}}) \tag{1.23}$$

The contact at zero load is also of interest. Similarly, the contact radius at zero load ($F_0 = 0$) a_s can be derived:

$$a_s^3 = \frac{9R^2\Delta\gamma\pi}{2E^*} \tag{1.24}$$

The indentation depth at zero load a_s is calculated as

$$d_c = \frac{a_s^2}{R} = (\frac{9}{2})^{\frac{2}{3}}(\Delta\gamma)^{\frac{2}{3}}(\frac{\pi^{\frac{2}{3}}R^{\frac{1}{3}}}{E^{*\frac{2}{3}}}) \tag{1.25}$$

Park studied the mechanical properties of bilayers made from dipalmitoyl phosphatidylethanolamine and dipalmitoyl phosphatidylcholine lipids.[31] Nanoindentation force curves show different surface interactions among different bilayers, and adhesion energies between the probes and samples were calculated according to JKR theory. Zhang *et al.* were able to quantify differences in surface energies between crystalline and amorphous solid lactose from pull-off energies between indenter and lactose extracted from indentation curves.[32] Liu *et al.* used JKR theory to identify pH and drug-loading effects on adhesion between drug delivery particles and the extracellular matrix.[33] Peisker and Gorb applied JKR theory to interpret the reduced pull-off force from nanoindentation force curves on cuticular nanostructures in insect eyes, concluding that these structures do serve an anti-contamination function.[34]

1.3.2 The Tabor Coefficient and Models of Intermediate and Long-Range Adhesive Interactions

Bradley also studied the forces between two rigid spheres, using the Lennard-Jones potential to describe the adhesive interactions.[35] Derjaguin modeled these longer-range interactions as well, although with different boundary conditions and hence a different functional form.[36] Barthel provides an excellent review of the evolution of these and related theories.[37] Not surprisingly, these models resulted in different measures of adhesion. For the particular geometry of two rigid spheres of radius R, with the same surface energy, γ, JKR theory finds the minimum pull-off force due to the short-range adhesive interactions to be $\frac{3}{2}\pi\gamma R$. Bradley's approach using the longer-range Lennard-Jones interactions leads to a pull-off force of $2\pi\gamma R$.

Tabor, Maguis, and others have provided a mathematical and conceptual link between these two extremes by introducing a parameter which at small or zero limit reduces to JKR theory while at large or infinite limit resolves to Bradley's expression.[38]

In Tabor's formulation, the factor is called the Tabor number and is defined as:

$$\mu = \frac{R\Delta\gamma^2}{E^{*2}\epsilon} \tag{1.26}$$

Because it depends on both the elastic modulus E^*, and the surface energy, γ, the Tabor number provides a balance between the deformation effects and the adhesion effects. (ϵ in this equation is the energy minimum in the Lennard-Jones potential.)

JKR theory and Bradley theory are two extreme examples of adhesive contact. In between, the Derjaguin-Muller-Toporov (DMT), Maugis-Dugdale (MD), Carpick-Ogletree-Salmeron (COS) models are developed. Each of them emphasizes a specific range of forces.[39] Boukallel *et al.* studied epithelial HeLa cells with JKR, DMT, and Hertz models.[40] The JKR and DMT models agree well with the force curves of the cells while the Hertzian model does not, indicating the importance of adhesion in interpreting force curves for these systems. Synytska *et al.* applied DMT theory to examine adhesive properties in thermoresponsive polymers, a very important consideration in biomaterials design.[41]

1.4 Creep

Up to now, we have treated elasticity and plasticity as instantaneous properties; that is, a stress will induce elastic or plastic deformation immediately with negligible time delay. In reality, time dependent deformation can be significant. For example, if an indenter is held after loading (before unloading), it can continue to sink into the sample where the material has some viscoelasticity or viscoplasticity. This subsequent indentation is called creep (Figure 1.5).

Viscoelastic response in a material can be modeled with a circuit diagram of mechanical components.[42] Elasticity can be represented by springs since force changes

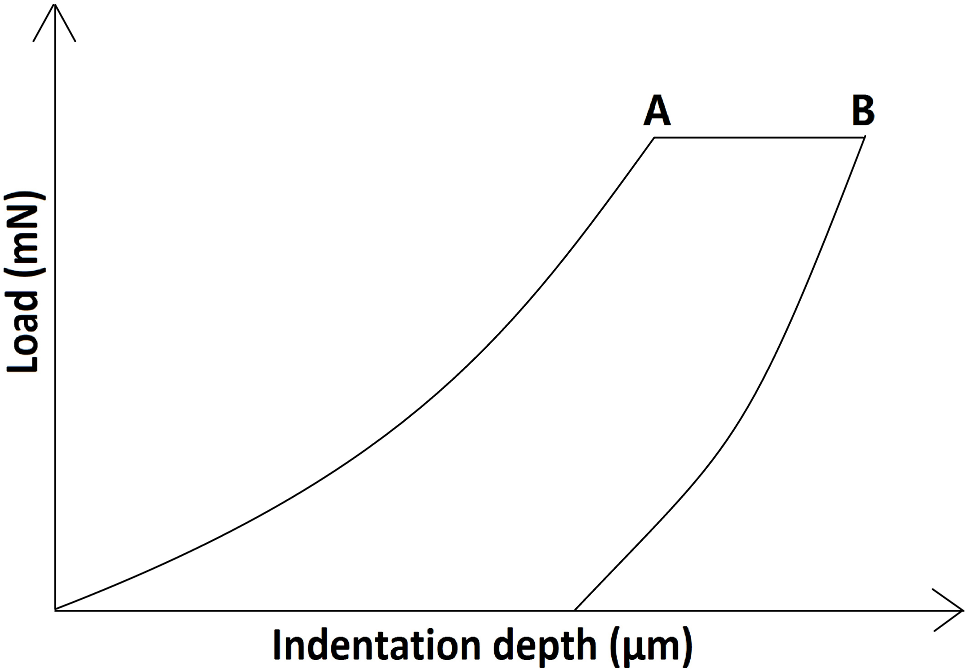

Figure 1.5: Creep test. From A to B, the load is kept constant. Because of material viscosity, the indenter continue to penetrate the material. The indentation depth increases accordingly.

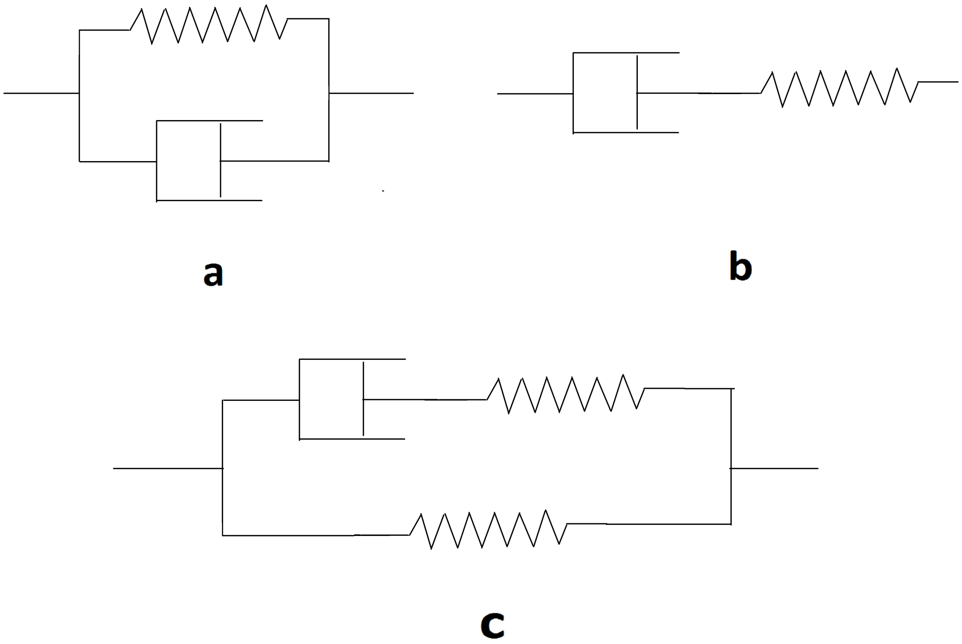

Figure 1.6: Different methods of modeling viscoelasticity: a) Kelvin-Voigt Model, b) Maxwell Model and c) Standard Linear Solid Model. Springs represent the elasticity components and dashpots represent the viscosity component.

linearly with the displacement of the spring (Hooke's Law, $F = kx$). Viscosity can be represented by dashpots, whose force changes linearly with the rate of displacement of the dashpot ($F = \eta\dot{x}$, where η is viscosity). There are many models to deal with viscoelastic problems, differing in how springs and dashpots are combined (Figure 1.6).[42, 43] One solution for the Voigt model (Figure 1.6 a) using Berkovich indenter is:[44]

$$h^2(t) = \frac{\pi}{2} F_{max} cot\alpha \left(\frac{1}{E}\left(1 - e^{-tE/\eta}\right)\right) \tag{1.27}$$

$h(t)$ is the creep distance over time, F_{max} is the maximum load, α is the equivalent cone semi-angle to the indenter face angle, t is time, E is the elasticity component and η is the viscosity component.

These relatively simple assemblies of springs and dashpots can successfully model the viscoelastic response of even very complex systems such as bone[42, 44, 45] and teeth,[46] with the ability to detect differences by tissue type (trabecular *vs.* cortical bone; peritubular *vs.* intertubular dentin), age, and other factors. The viscoelastic properties of soft tissues[47] and biofilms[48] can also be modeled in this fashion. Measurements on single cells[43, 49, 50] can provide information about effects of differentiation, age, and cell membrane chemical composition on viscoelasticity.

1.5 Finite Element Method

All of the methods mentioned above have analytical solutions, but the finite element approach is a numerical method. In the finite element method, a grid or lattice is defined on a material, with properties defined for each node. Stress, displacement, *etc.*, are calculated at each node, and the whole deformation process can be simulated and visualized. In this way, a finite element approach can link local properties to larger scale response. Furthermore, structural contributions to the indentation response can be assessed: by comparing the predicted force curves for various structures to the measured force curve, the internal structure of the material can be elucidated.

For example, models for the complex structures of virus capsids (the outer protein shells of viruses) can be assessed in comparison to nanoindentation data. The results of finite element analyses of force curve data indicate that there are significant differences in the way in which different viruses are constructed internally on a smaller scale as well as their obvious external larger scale shape differences, from the tubular tobacco mosaic virus (TMV)[51] to the spherical Hepatitis B virus (HBV)[52, 53] and Cowpea chlorotic mottle virus (CCMV).[54] Other large protein assemblies are also studied by this method, such as microtubules.[55]

Finite element analysis can also simulate materials with viscous (Section 1.4) and plastic properties (Section 1.3). These properties would introduce extra parameters that will make the system much more complicated. Carnelli *et al.* investigated elastic-plastic deformation of human tibial cortical tissue.[56] The mechanical properties are directionally dependent: both Young's modulus and hardness in the axial direction are larger than that in the transverse direction. Zhang *et al.* studied viscoelastic and plastic behavior of various types of bone.[57] The finite element modeling provided insights into the heterogeneities and anisotropies which must be present in the model to mimic the experimentally observed response to indentation, and the same group has published other work analyzing the effects of heterogeneity using finite element models.[58]

1.6 Methods and Applications in this Thesis

This thesis presents work on new and established methods for nanostructural and nanomechanical characterization of biomaterials. The Chapter 2 establishes a new method for measuring Young's moduli in soft materials which is particularly well suited for nanostructures and thin films. Chapter 3 to chapter 5 focus on collagen self-assemblies. Although the collagen samples are partially dried to facilitate characterization, they are still highly hydrated since only mild drying techniques are used and the obtained Young's moduli are close to the literature values of hydrated samples.[59] Chapter 3 extends the method in chapter 2 to samples where capillary forces are dominant and presents results on type I collagen segment-long-spacing crystallites (SLS). Chapters 4 and 5 compare the fibrillogenesis, structure and nanomechanics of type I and type II collagen fibrils, using measurements of traditional force curves and persistence length.

Bibliography

[1] M. Sun, A. Stetco, and E. F. Merschrod S. Surface-templated formation of protein microfibril arrays. *Langmuir*, 24:5418–5421, 2008.

[2] F. Höök, B. Kasemo, M. Grunze, and S. Zauscher. Quantitative biological surface science: challenges and recent advances. *ACS Nano*, 2:2428–2436, 2008.

[3] R. Bos, H. C. van der Mei, and H. J. Busscher. Physico-chemistry of initial microbial adhesive interactions - its mechanisms and methods for study. *FEMS Microbiology Reviews*, 23:179–230, 1999.

[4] Y. F. Dufrêne. Atomic force microscopy of fungal cell walls: an update. *Yeast*, 27:465–471, 2010.

[5] M. P. E. Wenger, L. Bozec, M. A. Horton, and P. Mesquida. Mechanical properties of collagen fibrils. *Biophysical Journal*, 93:1255–1263, 2007.

[6] J. L. Cuellar, F. Meinhoevel, M. Hoehne, and E. Donath. Size and mechanical stability of norovirus capsids depend on pH: a nanoindentation study. *Journal of General Virology*, 91:2449–2456, 2010.

[7] V. L. Popov. *Contact Mechanics and Friction: Physical Principles and Applications*. Springer, Berlin, 2008.

[8] A. C. Fischer-Cripps. *Introduction to Contact Mechanics*. Springer, New York, 2nd edition, 2006.

[9] B. Nowak and J. Najar. Numerical simulation of influence of chosen parameters on tensile stresses in bone cement layer in total hip arthoplastry. *Advances in Materials Science and Engineering*, 6:9–17, 2006.

[10] R. Shahar, P. Zaslansky, M. Barak, A. A. Fresem, J. D. Currey, and S. Weiner. Anisotropic Poisson's ratio and compression modulus of cortical bone determined by speckle interferometry. *Journal of Biomechanics*, 40:252–264, 2007.

[11] A. P. C. Choi and Y. P. Zheng. Estimation of Young's modulus and Poisson's ratio of soft tissue from indentation using two different-sized indentors: finite element analysis of the finite deformation effect. *Medical & Biological Engineering & Computing*, 43:258–264, 2005.

[12] K. L. Johnson. *Contact Mechanics*. Cambridge University Press, Cambridge, 1985.

[13] J.-W. Park. Sulfatide incorporation effect on mechanical properties of vesicles. *Colloids and Surfaces B: Biointerfaces*, 80:59–62, 2010.

[14] I. N. Sneddon. The relation between load and penetration in the axisymmetric boussinesq problem for a punch of arbitrary profile. *International Journal of Engineering Science*, 3:47–57, 1965.

[15] M. R. VanLandingham, J. S. Villarrubia, W. F. Guthrie, and G. F. Meyers. Nanoindentation of polymers: an overview. *Macromolecular Symposia*, 167:15–44, 2001.

[16] M. F. Doerner and W. D. Nix. A method for interpreting the data from depth-sensing indentation instruments. *Journal of Materials Research*, 1:601–609, 1986.

[17] W. C. Oliver and G. M. Pharr. An improved technique for determining hardness and elastic modulus using load and displacement sensing indentation experiments. *Journal of Materials Research*, 7:1564–1583, 1992.

[18] L. H. He and M. V. Swain. Nanoindentation derived stress-strain properties of dental materials. *Dental Materials*, 23:814–821, 2007.

[19] L. A. Darnell, M. F. Teaford, K. J. Livi, and T. P. Weihs. Variations in the mechanical properties of *Alouatta palliata* molar enamel. *American Journal of Physical Anthropology*, 141:7–15, 2010.

[20] L. Li, H. Pan, J. Tao, X. Xu, C. Mao, X. Gu, and R. Tang. Repair of enamel by using hydroxyapatite nanoparticles as the building blocks. *Journal of Materials Chemistry*, 18:4079–4084, 2008.

[21] B. R. H. Nizam, C. T. Lim, H. K. Chng, and A. U. J. Yap. Nanoindentation study of human premolars subjected to bleaching agent. *Journal of Biomechanics*, 38:2204–2211, 2005.

[22] Y.-R. Jeng, T.-T. Lin, and D.-B. Shieh. Nanotribological characterization of tooth enamel rod affected by surface treatment. *Journal of Biomechanics*, 42:2249–2254, 2009.

[23] M. R. Kumar, E. F. Merschrod S., and K. M. Poduska. Correlating mechanical properties with aggregation processes in electrochemically fabricated collagen membranes. *Biomacromolecules*, 10:1970–1975, 2009.

[24] O. Brennan, O. D. Kennedy, T. C. Lee, S. M. Rackard, and F. J. O'Brien. Biomechanical properties across trabeculae from the proximal femur of normal and ovariectomised sheep. *Journal of Biomechanics*, 42:498–503, 2009.

[25] T. Jämsä, J.-Y. Rho, Z. Fan, C. A. MacKay, S. C. Marks Jr., and J. Tuukkanen. Mechanical properties in long bones of rat osteopetrotic mutations. *Journal of Biomechanics*, 35:161–165, 2002.

[26] J. Y. Rho, P. Zioupos, J. D. Currey, and G. M. Pharr. Microstructural elasticity and regional heterogeneity in human femoral bone of various ages examined by nano-indentation. *Journal of Biomechanics*, 35:189–198, 2002.

[27] P. K. Zysset, X. E. Guo, C. E. Hoffler, K. E. Moore, and S. A. Goldstein. Elastic modulus and hardness of cortical and trabecular bone lamellae measured by nanoindentation in the human femur. *Journal of Biomechanics*, 32:1005–1012, 1999.

[28] M. Müller, M. Olek, M. Giersig, and H. Schmitz. Micromechanical properties of consecutive layers in specialized insect cuticle: the gula of *Pachnoda marginata* (Coleoptera, Scarabaeidae) and the infrared sensilla of *Melanophila acuminata* (Coleoptera, Buprestidae). *The Journal of Experimental Biology*, 211:2576–2583, 2008.

[29] I. Scholz, W. J. P. Barnes, J. M. Smith, and W. Baumgartner. Ultrastructure and physical properties of an adhesive surface, the toe pad epithelium of the tree frog, *Litoria caerulea* White. *The Journal of Experimental Biology*, 212:155–162, 2009.

[30] K. L. Johnson, K. Kendall, and A. D. Roberts. Surface energy and the contact of elastic solids. *Proceedings of the Royal Society A: Mathematical, Physical and Engineering Sciences*, 324:301–313, 1971.

[31] J.-W. Park. Probe chemistry effect on surface properties of asymmetric-phase lipid bilayers. *Colloids and Surfaces B: Biointerfaces*, 75:290–293, 2010.

[32] J. Zhang, S. Ebbens, X. Chen, Z. Jin, S. Luk, C. Madden, N. Patel, and C. J. Roberts. Determination of the surface free energy of crystalline and amorphous lactose by atomic force microscopy adhesion measurement. *Pharmaceutical Research*, 23:401–407, 2006.

[33] V. Chan, K.-K. Liu, C. L. Visage, B.-F. Ju, and K. W. Leong. Bioadhesive characterization of poly(methylidene malonate 2.12) microparticle on model extracellular matrix. *Biomaterials*, 25:4327–4332, 2004.

[34] H. Peisker and S. N. Gorb. Always on the bright side of life: anti-adhesive properties of insect ommatidia grating. *The Journal of Experimental Biology*, 213:3457–3462, 2010.

[35] R. S. Bradley. The cohesive force between solid surfaces and the surface energy of solids. *Philosophical Magazine Series 7*, 13:853–862, 1932.

[36] B. Derjaguin. Untersuchungen über die reibung und adhäsion, iv. *Kolloid-Zeitschrift*, 69(2):155–164, 1934.

[37] E. Barthel. Adhesive elastic contacts: JKR and more. *Journal of Physics D: Applied Physics*, 41:163001, 2008.

[38] D. Maugis. Adhesion of spheres: the JKR-DMT transition using a Dugdale model. *Journal of Colloid and Interface Science*, 150:243–269, 1992.

[39] X. Shi and Y.-P. Zhao. Comparison of various adhesion contact theories and the influence of dimensionless load parameter. *Journal of Adhesion Science and Technology*, 18:55–68, 2004.

[40] M. Boukallel, M. Girot, and S. Régnier. Characterization of cellular mechanical behavior at the microscale level by a hybrid force sensing device. *Journal of the Mechanical Behavior of Biomedical Materials*, 2:297–304, 2009.

[41] A. Synytska, E. Svetushkina, N. Puretskiy, G. Stoychev, S. Berger, L. Ionov, C. Bellmann, K.-J. Eichhorn, and M. Stamm. Biocompatible polymeric materials with switchable adhesion properties. *Soft Matter*, 6:5907–5914, 2010.

[42] Z. Wu, T. A. Baker, T. C. Ovaert, and G. L. Niebur. The effect of holding time on nanoindentation measurements of creep in bone. *Journal of Biomechanics*, 44:1066–1072, 2011.

[43] M. R. Ahmad, M. Nakjima, S. Kojima, M. Homma, and T. Fukuda. Nanoindentation methods to measure viscoelastic properties of single cells using sharp, flat, and buckling tips inside ESEM. *NanoBioscience, IEEE Transactions on*, 9:12–23, 2010.

[44] D.-G. Kim, S. S. Huja, H. R. Lee, B. C. Tee, and S. Hueni. Relationships of viscosity with contact hardness and modulus of bone matrix measured by nanoindentation. *Journal of Biomechanical Engineering*, 132:024502, 2010.

[45] H. Isaksson, S. Nagao, M. Malkiewicz, P. Julkunen, R. Nowak, and J. S. Jurvelin. Precision of nanoindentation protocols for measurement of viscoelasticity in cortical and trabecular bone. *Journal of Biomechanics*, 43:2410–2417, 2010.

[46] G. Balooch, G. W. Marshall, S. J. Marshall, O. L. Warren, S. A. S. Asif, and M. Balooch. Evaluation of a new modulus mapping technique to investigate microstructural features of human teeth. *Journal of Biomechanics*, 37:1223–1232, 2004.

[47] G. Constantinides, Z. I. Kalcioglu, M. McFarland, J. F. Smith, and K. J. V. Vliet. Probing mechanical properties of fully hydrated gels and biological tissues. *Journal of Biomechanics*, 41:3285–3289, 2008.

[48] P. C. Y. Lau, J. R. Dutcher, T. J. Beveridge, and J. S. Lam. Absolute quantitation of bacterial biofilm adhesion and viscoelasticity by microbead force spectroscopy. *Biophysical Journal*, 96:2935–2948, 2009.

[49] V. Vadillo-Rodriguez and J. R. Dutcher. Dynamic viscoelastic behavior of individual gram-negative bacterial cells. *Soft Matter*, 5:5012–5019, 2009.

[50] Y. Xu, G. Balooch, M. Chiou, E. Bekerman, R. O. Ritche, and M. T. Longaker. Analysis of the material properties of early chondrogenic differentiated adipose-derived stromal cells (ASC) using an *in vitro* three-dimensional micromass culture system. *Biochemical and Biophysical Research Communications*, 359:311–316, 2007.

[51] Y. Zhao, Z. Ge, and J. Fang. Elastic modulus of viral nanotubes. *Physical Review E*, 78:031914, 2008.

[52] W. H. Roos, M. M. Gibbons, A. Arkhipov, C. Uetrecht, N. R. Watts, P. T. Wingfield, A. C. Steven, A. J. R. Heck, K. Schulten, W. S. Klug, and G. J. L. Wuite. Squeezing protein shells: how continuum elastic models, molecular dynamics simulations, and experiments coalesce at the nanoscale. *Biophysical Journal*, 99:1175–1181, 2010.

[53] C. Carrasco, M. Castellanos, P. J. de Pablo, and Mauricio G. Mateu. Manipulation of the mechanical properties of a virus by protein engineering. *Proceedings of the National Academy of Sciences of the United States of America*, 105:4150–4155, 2008.

[54] M. M. Gibbons and W. S. Klug. Influence of nonuniform geometry on nanoindentation of viral capsids. *Biophysical Journal*, 95:3640–3649, 2008.

[55] Z. J. Donhauser, W. B. Jobs, and E. C. Binka. Mechanics of microtubules: effects of protofilament orientation. *Biophysical Journal*, 99:1668–1675, 2010.

[56] D. Carnelli, D. Gastaldi, V. Sassi, and R. Contro. A finite element model for direction dependent mechanical response to nanoindentation of cortical bone allowing for anisotropic post-yield behaviour of the tissue. *Journal of Biomechanical Engineering*, 132:081008, 2010.

[57] J. Zhang, G. L. Niebur, and T. C. Ovaert. Mechanical property determination of bone through nano- and micro-indentation testing and finite element simulation. *Journal of Biomechanics*, 41:267–275, 2008.

[58] Y. Zhao and T. C. Ovaert. Error estimation of nanoindentation mechanical properties near a dissimilar interface via finite element analysis and analytical solution methods. *Journal of Materials Research*, 25:2308–2316, 2010.

[59] A. Gautieri, S. Vesentini, A. Redaelli, and M. J. Buehler. Hierarchical structure and nanomechanics of collagen microfibrils from the atomistic scale up. *Nano Letters*, 11:757–766, 2011.

Chapter 2

Mininum Nanoindentation Method

We report a method to calculate soft material Young's moduli at the minimum indentation depth with high precision. An atomic force microscope (AFM) is employed to conduct nanoindentation experiments on soft materials. In the jump-to-contact process, the indenter-sample adhesion energy approximately equals the sample elastic deformation stored energy. Based on this relation, we calculate Young's moduli at minimum indentation depths (less than 10 nm depending on the material properties) that can be validly observed in the nanoindentation process. This makes our method especially useful in the characterization of nanoscale objects and the surface of materials, particularly soft materials. Measurements of polycarbonate and low-density polyethylene (LDPE) verify this method, yielding Young's moduli of 2.7 GPa and 0.27 GPa for these two materials respectively.

2.1 Introduction

Indentation is widely used to determine mechanical properties of materials. The emergence of the AFM pushed indentation techniques to a new stage with nanometer indentation depth control and nanonewton force measurement.[1] The indentation depth and force can be monitored continuously, with the resulting force versus indentation depth plot (force curve) providing information about the material deformation process during indentation. Nanoindentation has been carried out with different indentation depths ranging from several nanometers to micrometers.[2–4]

However, no study has been conducted on determining the minimum indentation depth needed to achieve nanoindentation. This is not only theoretically interesting but also practically useful, since minimum indentation is always desirable in measuring mechanical properties of nanoscale objects (such as a virus or cell).[5] Larger indentation depth may result in penetrating the whole object or at least can push past the elastic limit. The minimum indentation depth is also less destructive than larger indentation depth. Non-destructive indentation is particularly important with biological samples when the viability and/or integrity of the sample is vital for subsequent studies.[6] In addition to these issues with plastic deformation, soft materials often exhibit significant viscoelastic response to indentation, which can confound the extraction of a purely elastic modulus. Minimum indentation also minimizes the viscoelastic response of the material.

2.2 Theory

2.2.1 Nanoindentation Process and Force Curves

Figure 2.1 illustrates a schematic view of the nanoindentation process. Figure 2.2 is a cantilever deflection (d) versus indenter rest position (h) force curve obtained in this process, with d and h defined in Figure 2.3. When the indenter is far away from the sample surface (position A in Figure 2.1), the molecular force between the sample and the indenter is very weak and the deflection is zero (point A in Figure 2.2).

The cantilever deflection increases (cantilever bends downwards) with the de-

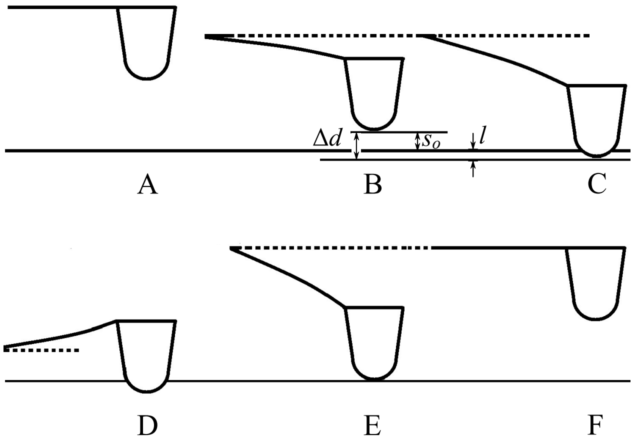

Figure 2.1: Schematic view of the cantilever during the nanoindentation process showing the approach (A–B), jump-to-contact (C), indentation (D), retraction (E), and jump-off-contact (F) stages.

crease of the indenter-sample distance according to the nonlinear Lennard-Jones potential.[7] At position B in Figure 2.1 (point B in Figure 2.2), the force gradient exceeds the spring constant of the cantilever. The cantilever will no longer be able to support itself and the indenter will jump to contact with the sample. The indenter-sample distance at position B is s_0 which is of great interest to our research and will be discussed later.

The indenter will continue to penetrate the sample until it reaches a quasistatic nanoindentation state (position C in Figure 2.1 and point C in Figure 2.2), in which the released adhesion energy between the indenter and the sample is balanced by the elastic deformation stored energy of the sample. The process from the beginning of the jump (B) to the point of reaching a quasistatic state (C) only takes around 2 ms as observed in our force curves. The jump distance is Δd and the penetration depth at position C is l as shown in Figure 2.1. The z-controller of the AFM moves the cantilever at a speed of 20 nm/s, which means the indenter rest position changes by 20 nm/s. Therefore, the difference between the rest indenter positions at B and C in Figure 2.1 is only 0.04 nm which can be neglected, with points B and C in Figure 2.2

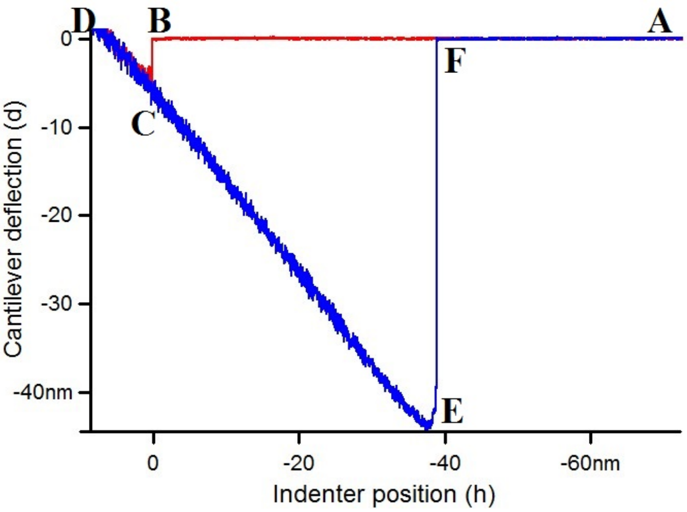

Figure 2.2: Experimental force curve with the approach (A–B), jump-to-contact (C), indentation (D), retraction (E), and jump-off-contact (F) stages marked. The red curve is the approach curve and the blue curve is the retraction curve.

almost vertically lined up. If the *z*-controller moved much faster, the jump-to-contact phenomenon would not be as obvious. Hence it is desirable to move the *z*-controller at a slow speed.

When the cantilever is further lowered, because of sample elastic deformation the cantilever deflection decreases to zero and then increases in the other direction (cantilever bends upwards) until it reaches the maximal indentation depth (position *D* in Figure 2.1 and point *D* in Figure 2.2). Then as the cantilever is slowly (20 nm/s) moved away from the sample, the cantilever deflection will decrease to zero and increase in the other direction (cantilever bends downwards) again until it reaches the maximal deflection (position *E* in Figure 2.1 and point *E* in Figure 2.2). At position *E* the adhesion force is smaller than the sum of cantilever and sample elastic deformation forces, and the cantilever will jump off of contact with the sample (position *F* in Figure 2.1 and point *F* in Figure 2.2).

Because of the jump-to-contact effect, any indentation depth less than the indentation depth l cannot be achieved. If the indenter immediately retracts after it

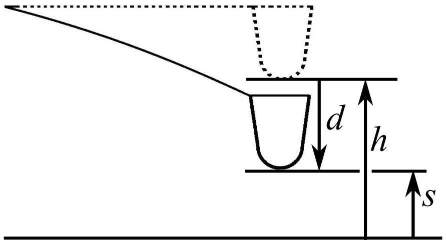

Figure 2.3: Schematic view of the cantilever during indentation, showing the definitions of cantilever deflection (d), indenter rest position (h), and indenter-sample distance (s). The arrows indicate the sign for each quantity: d is negative (deflection down from zero) while h is positive (distance from sample surface). Therefore, the indenter-sample distance s is $h + d$.

jumps to contact with the sample (position C in Figure 2.1 and point C in Figure 2.2), nanoindentation with minimum indentation depth is achieved.

2.2.2 Determination of the Jump-to-Contact Point

Molecular forces are short-range forces. For an indenter with a spherical profile and the indenter-sample separation much less than the radius of the indenter curvature, the interaction between the indenter and the flat sample before contact can be approximated as the interaction between a sphere with the same radius of the indenter curvature and a plane. Before the indenter contacts the sample, if the cantilever moves slowly at a constant velocity, air drag force and acceleration force can be neglected. Then the molecular force between the tip and the sample (right side of Equation 2.1) which depends on the indenter-sample distance ($h + d$) is equal to the cantilever deflection force (left side of Equation 2.1):[8]

$$kd = -\frac{AR}{6(h+d)^2} \tag{2.1}$$

We assume the value of the indenter rest position (h in Figure 2.3) is positive and the value of the cantilever deflection is negative. A is the Hamaker constant between the indenter and the sample. It is a parameter representing the microscopic Van der Waals force between macroscopic objects. Hamaker constants for different materials were calculated from Equation 2.2.

$$A_{12} = \sqrt{A_{11}A_{22}} \tag{2.2}$$

A_{11}, A_{22} and A_{12} are the sample-sample interaction Hamaker constant, gold-gold interaction Hamaker constant (the indenters were coated with gold) and sample-gold interaction Hamaker constant respectively.

One of the most challenging steps in nanoindentation is to determine indenter-sample distance. If the cantilever deflection d at one point is measured, the cantilever rest position h at that point can be calculated from Equation 2.1. The indenter-sample distance can then be obtained $(h + d)$. The indenter-sample distance of other points can be deduced from their relative distance to the determined point. This point should possess minimum percent error to correctly reflect the indenter-sample distance. However, the interaction between the indenter and sample is very weak even when they are tens of nanometers away. This would result in a value of d comparable to instrumental error. Therefore, an optimized reference point must be found to reduce the experiment percentage error. When $A = 0.1$ nN·nm, $R = 50$ nm, $k = 0.1$ nN/m and $h = 10$ nm, d is calculated to be 0.08 nm which is larger than our instrument error.

To obtain the value for d we can solve Equation 2.1. This yields three solutions for d (d_1, d_2 and d_3):

$$d_1 = \frac{1}{3}(-2h - \frac{2^{\frac{1}{3}}h^2}{(27c - 2h^3 + 3\sqrt{3}\sqrt{27c^2 - 4ch^3})^{\frac{1}{3}}} - \frac{(27c - 2h^3 + 3\sqrt{3}\sqrt{27c^2 - 4ch^3})^{\frac{1}{3}}}{2^{\frac{1}{3}}}) \tag{2.3}$$

$$d_2 = -\frac{2}{3}h + \frac{(1 + i\sqrt{3})h^2}{3 \times 2^{\frac{2}{3}}(27c - 2h^3 + 3\sqrt{3}\sqrt{27c^2 - 4ch^3})^{\frac{1}{3}}} + \frac{(1 - i\sqrt{3})(27c - 2h^3 + 3\sqrt{3}\sqrt{27c^2 - 4ch^3})^{\frac{1}{3}}}{6 \times 2^{\frac{1}{3}}} \tag{2.4}$$

$$d_2 = -\frac{2}{3}h + \frac{(1 - i\sqrt{3})h^2}{3 \times 2^{\frac{2}{3}}(27c - 2h^3 + 3\sqrt{3}\sqrt{27c^2 - 4ch^3})^{\frac{1}{3}}} + \frac{(1 + i\sqrt{3})(27c - 2h^3 + 3\sqrt{3}\sqrt{27c^2 - 4ch^3})^{\frac{1}{3}}}{6 \times 2^{\frac{1}{3}}} \tag{2.5}$$

where $c = \frac{AR}{6k}$.

We plot the real parts of d_1, d_2 and d_3 against h, shown in Figure 2.4 for $A = 0.1$ nN·nm, $R = 50$ nm and $k = 0.1$ nN/m.

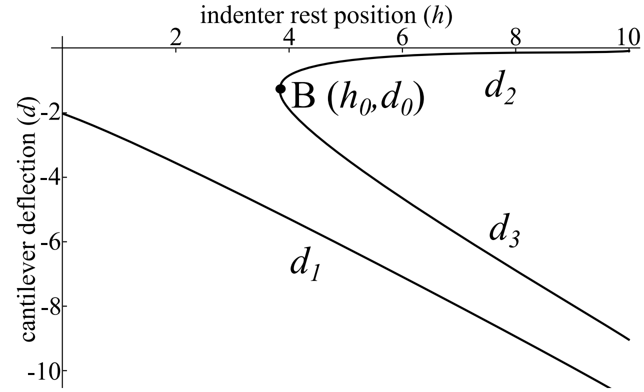

Figure 2.4: Plots of d_1, d_2 and d_3 (solutions to Equation 2.1) against h. Point B is the jump-to-contact point, also labeled B in Figs. 2.1 and 2.2.

When the indenter approaches the sample, the cantilever deflection increases according to d_2. When curve d_2 encounters curve d_3 at coordinate B $(h_0,\ d_0)$, the cantilever is unstable and will jump to contact with the sample. Therefore, the rest indenter position (h_0) and the cantilever deflection (d_0) at position B can be determined by solving $d_3 = d_2$.

$$d_0 = -\frac{c^{\frac{1}{3}}}{2^{\frac{2}{3}}} = -(\frac{AR}{24k})^{\frac{1}{3}} \tag{2.6}$$

$$h_0 = 3\frac{c^{\frac{1}{3}}}{2^{\frac{2}{3}}} = 3(\frac{AR}{24k})^{\frac{1}{3}} \tag{2.7}$$

d_0 represents the largest d value before the abrupt jump. The instrumental error is fixed, so d_0 possesses the minimum percent error. The relationship among s_0, Δd and indentation depth at position C (l) is illustrated in Figure 2.5.

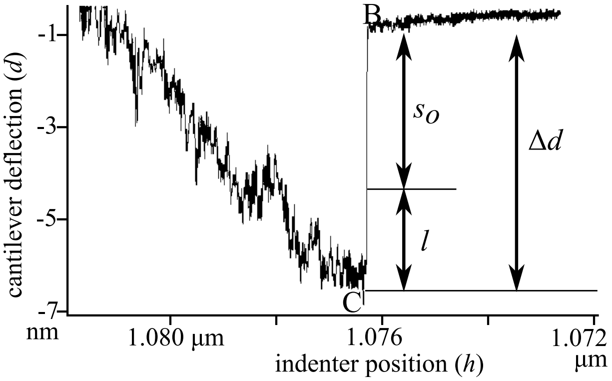

Figure 2.5: Experimental force curve expanding the jump-to-contact stage to emphasize the differences and connections between the cantilever deflection (Δd), penetration depth (l) and indenter-sample distance at point B (s_0).

The indenter-sample distance at position B (Figure 2.1) (s_0), defined by h_0 and d_0, is calculated from Eqs. 2.7 and 2.6:

$$s_0 = h_0 + d_0 = 2(\frac{AR}{24k})^{\frac{1}{3}} \tag{2.8}$$

2.2.3 The Jump-to-Contact Indentation Depth and Sample Elastic Deformation Stored Energy

The process of jump-to-contact happens in around 2 ms. Therefore the indenter rest positions are almost the same before and after the jump (0.04 nm difference). Because that difference is negligible, the indentation depth at position C (l in Figure 2.5) is equal to the difference between the indenter jump distance (Δd) and the indenter-sample distance s_0 at position B in Figure 2.1 (Equation 2.8). Δd can be determined from the force curve: it is the vertical distance from point B to point C.

$$l = \Delta d - s_0 = \Delta d - 2(\frac{AR}{24k})^{\frac{1}{3}} \tag{2.9}$$

For nanoindentation with an indentation depth of less than 10 nm, the indenter-sample indentation contact depth is approximately equal to the indentation depth. Based on our calculations, the mean contact pressure during the jump to contact process is much less than most soft material yield stresses, which is the criterion for fully elastic deformation.[9] If the deformation is assumed to be fully elastic, the final indentation depth (the residual indent depth after the indenter jumps off contact with the sample) is equal to zero. This elastic deformation assumption was verified by taking an AFM image after indentation.

The elastic deformation force F_e of the sample at indentation depth i can be determined by the Hertzian indentation model:[10]

$$F_e = \frac{4}{3}E^* R^{\frac{1}{2}} i^{\frac{3}{2}} \tag{2.10}$$

E^* is the reduced Young's modulus which can be calculated by the following equation:

$$\frac{1}{E^*} = \frac{1-{\nu_s}^2}{E_s} + \frac{1-{\nu_i}^2}{E_i} \tag{2.11}$$

ν_s and ν_i are Poisson's ratios for sample and indenter respectively and E_s and E_i are Young's moduli for sample and indenter respectively. The Young's modulus of the indenter (made of silicon nitride coated with a layer of gold) is much larger than most soft samples and the Poisson's ratio of gold is around 0.42.[11] Hence $\frac{1-{\nu_i}^2}{E_i}$ is insignificant compared with $\frac{1-{\nu_s}^2}{E_s}$ and can be neglected. Therefore the Young's modulus of the soft sample is related to the reduced Young's modulus by:

$$E_s = \frac{E^*}{1-{\nu_s}^2} \tag{2.12}$$

In the jump to contact process, the elastic deformation stored energy (G_e) is by definition the integral of the elastic deformation force (F_e, Equation 2.10) over the indentation depth:[12]

$$G_e = \int_0^l F_e \, \mathrm{d}i = \frac{8}{15} E_s(1-\nu_s^2) R^{\frac{1}{2}} (\Delta d - 2(\frac{AR}{24k})^{\frac{1}{3}})^{\frac{5}{2}} \tag{2.13}$$

2.2.4 The Jump-off-Contact Process and Work of Adhesion

The jump-off-contact process is illustrated in Fig 2.6. The work of adhesion per unit area (γ_a) can be determined by the adhesion force before the point of jump-off-contact F_p.[13] The Derjaguin-Muller-Toporov (DMT) model assumes the same contact area as the Hertzian model but with additional long-range adhesive forces beyond the contact area:

$$F_p = 2\gamma_a \pi R \tag{2.14}$$

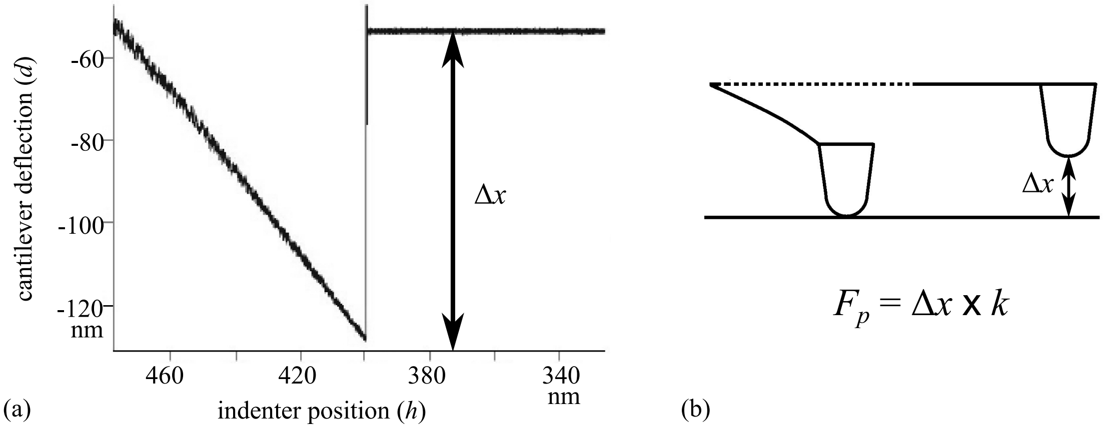

Figure 2.6: The jump-off-contact process shown in a force curve (a) and in a schematic of the cantilever position relative to the surface (b). k is the spring constant of the cantilever, and F_p is the adhesion force before the point of jump-off-contact.

while the Johnson-Kendall-Roberts (JKR) model calculates the adhesive forces within a contact area adjusted to account for deformation:

$$F_p = \frac{3}{2}\gamma_a \pi R \tag{2.15}$$

The work of adhesion is deduced from the jump-off-contact phenomenon rather than taking a value from a literature. This significantly reduces errors because the force curve directly reflects the actual interaction between the indenter and the sample.

We find that the JKR model provides more accurate results and use Equation 2.15. Analogous equations and results using the DMT model for the work of adhesion (Equation 2.14) are included in the Appendix (Table A.1)

The adhesion energy is by definition

$$G_a = \gamma_a S \tag{2.16}$$

where S is the area of contact between the indenter and the sample.

Table 2.1: Measured and literature mechanical parameters for polycarbonate and LDPE; superscript numbers indicate the reference for the source of literature values

Material	Poisson's ratio	Hamaker constant (nN·nm)	Calculated E (GPa)	E in literature (GPa)
Polycarbonate	0.37[14]	0.14	2.7 ± 0.2	2.20-2.65[15]
LDPE	0.4[16]	0.16	0.27 ± 0.06	0.2-0.4[16]

2.2.5 The Adhesion Energy during Jumping to Contact

Our indenters have spherical profiles at their tips (see Figure A.1 for a sample scanning electron micrograph showing the spherical geometry at the tip.). At nanometer indentation depth, the indentation depth is approximately equal to the contact depth. When the indentation depth at position C (l in Figure 2.1) is less than the radius of the indenter curvature (R), the contact surface can be viewed as a spherical cap with a height of l. The contact area is calculated as:

$$S = 2\pi Rl = 2\pi R(\Delta d - 2(\frac{AR}{24k})^{\frac{1}{3}}) \tag{2.17}$$

Combining Eqs. 2.15, 2.16 and 2.17 gives the adhesion energy:

$$G_a = \frac{4}{3}F_p(\Delta d - 2(\frac{AR}{24k})^{\frac{1}{3}}) \tag{2.18}$$

After the indenter jumps to contact with the sample the sample will deform to absorb the energy released by the work of adhesion, which originates from the adhesive force between the indenter and the sample. For soft materials, the deformation of the indenter is negligible and the energy absorbed by the elastic deformation of the indenter is neglected. At the same time, the cantilever deflection and cantilever momentum will retain some energy, and friction will also dissipate some energy. These energies are very small, accounting for less than 2% of the total energies as estimated in our calculations. Therefore when the indentation reaches the quasistatic state (position C in Figure 2.5), the elastic deformation stored energy (G_e) is approximately equal to the adhesion energy (G_a):

$$G_e = G_a \tag{2.19}$$

Combining Eqs. 2.13, 2.18 and 2.19, the Young's modulus of the sample E_s is obtained:

$$E_s = \frac{5}{2}|F_p|R^{-\frac{1}{2}}(\frac{1}{1-{\nu_s}^2})(\Delta d - 2(\frac{AR}{24k})^{\frac{1}{3}})^{-\frac{3}{2}} \tag{2.20}$$

2.3 Experimental Methods

Polycarbonate and low-density polyethylene (LDPE) were tested to verify the theory presented above. Fifteen force curves were taken in air for each of the materials using an Asylum Research MFP-3D AFM. We selected hydrophobic materials to avoid capillary forces between the tip and sample.[17] Two CSC17/CR-AU AFM tips from MikroMasch were used in the indentation tests. They are made of silicon and coated with a 20 nm Au film over a 20 nm Cr sublayer. Both have a radius of curvature of about 50 nm as measured with a scanning electron microscope. (See Figure A.1 for a sample scanning electron micrograph showing the spherical geometry at the tip.) The spring constants of the tips were determined by the thermal noise method.[18] The tip used to indent polycarbonate has a spring constant of 0.152 nN/nm and the tip used to indent polyethylene has a spring constant of 0.135 nN/nm. The jump-to-contact distance and the maximal attractive force before jump-off-contact were extracted from the force curves to calculate Young's moduli. A_{12} for polycarbonate-gold is 0.14 nN·nm and for LDPE-gold is 0.16 nN·nm as calculated from Equation 2.2.[19–21] Creep tests (see Figure A.2) indicate that there is no significant viscoelastic response for our samples.

2.4 Experimental Results

The calculated Young's moduli of polycarbonate and LDPE are shown in Table 2.1, along with other physical parameters. The Young's moduli calculated by our method are in good accordance with literature values, supporting our theory and experimental approach. Although the method requires use of tabulated Hamaker constants, there are many materials where the Hamaker constant (dependent on the chemistry of the interaction) is known but the elastic modulus (dependent on structure as well) is not known, such as for thin films nanostructures, or other complex structures.

2.5 Conclusions

We have developed a method to calculate soft material Young's moduli based on the jump-to-contact and jump-off-contact phenomena. With our method, the minimum indentation depth is used. This method has great advantages over traditional nanoindentation methods for its minimal destruction, minimal viscoelastic effects, and being able to be applied to smaller objects. The jump-to-contact phenomenon was quantified to yield the indenter-sample distance value which possesses the minimal percentage error. The jump-off-contact phenomenon provided direct indenter-sample interaction information and the most reliable value of the work of adhesion between the indenter and the sample. This method is highly accurate as verified by our experiments on two polymers with well-characterized Young's moduli.

Bibliography

[1] D. C. Lin and F. Horkay. Nanomechanics of polymer gels and biological tissues: A critical review of analytical approaches in the Hertzian regime and beyond. *Soft Matter*, 4:669–682, 2008.

[2] W. C. Oliver and G. M. Pharr. Measurement of hardness and elastic modulus by instrumented indentation: Advances in understanding and refinements to methodology. *Journal of Materials Research*, 19:3–20, 1 2004.

[3] H. Isaksson, S. Nagao, M. Malkiewicz, P. Julkunen, R. Nowak, and J. S. Jurvelin. Precision of nanoindentation protocols for measurement of viscoelasticity in cortical and trabecular bone. *Journal of Biomechanics*, 43:2410–2417, 2010.

[4] L. A. Darnell, M. F. Teaford, K. J. Livi, and T. P. Weihs. Variations in the mechanical properties of *Alouatta palliata* molar enamel. *American Journal of Physical Anthropology*, 141:7–15, 2010.

[5] Y. F. Dufrêne. Atomic force microscopy of fungal cell walls: an update. *Yeast*, 27:465–471, 2010.

[6] M. Baclayon, G. J. L. Wuite, and W. H. Roos. Imaging and manipulation of single viruses by atomic force microscopy. *Soft Matter*, 6:5273–5285, 2010.

[7] S. Rützel, S. I. Lee, and A. Raman. Nonlinear dynamics of atomic-force-microscope probes driven in Lennard-Jones potentials. *Proceedings of the Royal Society A: Mathematical, Physical and Engineering Sciences*, 459:1925–1948, 2003.

[8] S. Das, P. A. Sreeram, and A. K. Raychaudhuri. A method to quantitatively evaluate the Hamaker constant using the jump-into-contact effect in atomic force microscopy. *Nanotechnology*, 18:035501, 2007.

[9] A. C. Fischer-Cripps. *Nanoindentation.* Springer, New York, 3rd edition, 2011.

[10] S. Strasser, A. Zink, M. Janko, W. M. Heckl, and S. Thalhammer. Structural investigations on native collagen type I fibrils using AFM. *Biochemical and Biophysical Research Communications*, 354:27–32, 2007.

[11] N. Agraït, G. Rubio, and S. Vieira. Plastic deformation of nanometer-scale gold connective necks. *Physical Review Letters*, 74:3995–3998, May 1995.

[12] J. Gubicza, A. Juhász, P. Arató, P. Szommer, P. Tasnádi, and G. Vörös. Elastic modulus determination from depth sensing indentation testing. *Journal of Materials Science Letters*, 15:2141–2144, 1996.

[13] K. L. Johnson. *Contact Mechanics*. Cambridge University Press, Cambridge, 1985.

[14] M. H. Litt, P. J. Koch, and A. V. Tobolsky. Cold flow of glassy polymers. III. Temperature dependence of yield elongation in BPA polycarbonate. *Journal of Macromolecular Science, Part B*, 1:587–594, 1967.

[15] V. A. Soloukhin, J. C. M. Brokken-Zijp, O. L. J. van Asselen, and G. de With. Physical aging of polycarbonate: elastic modulus, hardness, creep, endothermic peak, molecular weight distribution, and infrared data. *Macromolecules*, 36:7585–7597, 2003.

[16] W. Martienssen and H. Warlimont. *Springer Handbook of Condensed Matter and Materials Data*. Springer, Berlin, 2005.

[17] T. Eastman and D. Zhu. Adhesion forces between surface-modified AFM tips and a mica surface. *Langmuir*, 12:2859–2862, 1996.

[18] J. L. Hutter. Comment on tilt of atomic force microscope cantilevers: effect on spring constant and adhesion measurements. *Langmuir*, 21:2630–2632, 2005.

[19] S. Biggs and P. Mulvaney. Measurement of the forces between gold surfaces in water by atomic force microscopy. *The Journal of Chemical Physics*, 100:8501–8505, 1994.

[20] R. H. French. Origins and applications of London dispersion forces and Hamaker constants in ceramics. *Journal of the American Ceramic Society*, 83:2117–2146, 2000.

[21] G. R. Morrison, H. Hedmark, and S. A. M. Hesp. Elastic steric stabilization of polyethylene-asphalt emulsions by using low molecular weight polybutadiene and devulcanized rubber tire. *Colloid and Polymer Science*, 272:375–384, 1994.

Chapter 3

Nanostructure and Nanomechanics of Segment-Long-Spacing Collagen Crystallites

Type I collagen segment-long-spacing crystallites (SLS) were precipitated by the addition of adenosine-5'-triphosphate (ATP) and subsequently investigated with atomic force microscopy (AFM). SLS exhibits a saddle-like shape with two bulged ends and a thinner middle section. Mechanical properties of SLS were studied by nanoindentation, using the minimum nanoindentation model developed to deduce material Young's moduli in the presence of capillary forces.

3.1 Introduction

Collagen monomers are helical structured proteins with short non-helical C- and N-termini.[1] Collagen monomers can assemble into different structures. Type I collagen will form periodically banded native fibres with a periodicity of about 67 nm *in* *vivo*.[2] In the presence of adenosine-5'-triphosphate (ATP), special aggregates called segment-long-spacing collagen crystallites (SLS) are formed *in vitro*.[3]

SLS has long been the subject of interest since its discovery in the 1950s.[3] It has a polarized structure with individual collagen monomers being packed laterally and in parallel with each other in register. In other words, all the C-termini of collagen monomers stack together to form the SLS C-terminus and all the N-termini of collagen monomers stack together to form the SLS N-terminus.[4] As a result, the length of SLS is approximately equal to the length of a collagen monomer. The in-register packing manner facilitates the study of collagen monomers since SLS displays some amplified properties of an individual collagen monomer such as charge distribution and surface morphology.[3] This makes it an ideal material to study higher hierarchical structures.

Transmission electron microscopy (TEM) revealed that stained SLS would show characteristic parallel banding patterns perpendicular to the length of the SLS. This banding pattern is different from the banding pattern of native collagen fibers. These bands correspond to the positions of charged and/or hydrophobic groups depending on the staining methods.[5, 6] Great effort was done to correlate the bands to the particular peptide fragments or amino acid residues.[7]

The structure of SLS was used to deduce the monomer packing pattern of native collagen fibers by quarterly superposing the same SLS TEM image several times to generate an optically synthesized image.[8] The banding pattern of this optically synthesized image is found similar to the reconstituted fibril banding pattern. This implies that the native fibrils are formed by quarterly stacking monomers in parallel. However, latter studies found that in native collagen fibrils, neighboring monomers are packed in a way to form a super twisted right-handed microfibril which interdigitates with adjacent microfibrils.[9] The inconsistency may be caused by the difference between the reconstituted fibrils and the native fibrils: the bands of reconstituted fibrils are perpendicular to the monomer length while the bands of native fibril are slightly incline along the the monomer length.[8, 10]

SLS is also of biological importance. Procollagen and collagen SLS are found in various organelles of living organisms.[11, 12] SLS was thought to be an intermediate form during procollagen processing and trafficking.[13] SLS protects procollagen from protease attack and thermal denaturation.[14, 15] SLS is also documented in both normal and pathological tissues.[16]

Atomic force microscopy (AFM) offers nanometer resolution, direct operation on the sample, minimum sample destruction, and minimal sample preparation, making it the ideal tool for the study of biomaterial nanostructures.[17] AFM revealed that SLS is a saddle-like structure with several small ridges between two major bumps.[4] Thanks to the capability of operating AFM in solution, the SLS assembly mechanism was also investigated.[18] AFM is also capable of carrying out indentation tests on the nanometer scale which is particularly useful for studying nanostructures like SLS crystallites. In this chapter, AFM is applied to study the structure and mechanical properties of SLS. To the best of our knowledge, no report on the mechanical properties of SLS has been published so far.

3.2 Materials and Methods

3.2.1 SLS Preparation

Nutragen type I collagen (Advanced BioMatrix) is bovine hide, pepsin extracted collagen with a concentration of 6.4 mg/ml and pH of 2. During a typical SLS preparation, 2 mg adenosine-5'-triphosphate (ATP) (Sigma) were dissolved into 922 μL deionized water in a 1.5 mL conical tube. 78 μL Nutragen collagen was then pipetted into the ATP solution and mixed thoroughly. The pH of the solution was adjusted to

3.5 with 0.01 M HCl. After collagen was added, the clear colourless solution turned cloudy within several minutes, a sign of SLS formation. The mixture was incubated in ambient conditions for one hour.

To prepare SLS samples for AFM study, 10 μL SLS suspension was diluted 100-fold. 0.1 ml of the diluted suspension was transfered to a fleshly cleaved mica sheet. Excess solution was absorbed by placing paper tissue near the edge of solution droplet. The mica sheet surface was dried for half an hour at room temperature before being analyzed by AFM.

3.3 AFM Image and Minimum Nanoindentation

An MFP-3D stand alone AFM (Asylum Research) was used for sample imaging and nanoindentation. CSC17/CR-AU AFM probes (MikroMasch) were used as the AFM tips. They have a tip radius of 50 nm. The cantilever spring constants were calibrated by the thermal noise method.[19] The sample-deposited mica sheet was scanned under contact mode.

3.3.1 Minimum Nanoindentation Method under Capillary Force

The nanoscale dimensions of the SLS crystallites pose a great challenge on how the indentation test should be carried out. Depending on samples, instruments and other factors, indentation depth can vary from several nanometers to tens of millimeters during a traditional indentation test. For the SLS samples, minimum indentation depths (less than 10 nanometers) created by a nanometer-sized indenter are required: larger indentation depth would damage the SLS samples and the effect of substrate needs to be considered, resulting in inaccuracy and complexity.

When an AFM tip approaches the sample surface, attractive forces (e.g. van der

Waals force, capillary force, electrostatic force) increase nonlinearly with the decrease of the sample-tip distance. These forces are balanced by the cantilever elastic deflection force. While the gradient of the attractive forces increase with the decrease of the sample-indenter distance, the spring constant of the cantilever remains unchanged. At one point, the gradient of the attractive forces exceeds the spring constant of the cantilever, resulting in the tip snapping to contact with the sample surface (Figure 3.2).

After jumping to contact with the sample, the attractive forces drive the tip into the sample to create indentation. The tip will keep indenting until reaching the point that the attractive forces are balanced by other repulsive forces in addition to the elastic deflection force of the cantilever. Most of that repulsive force is the elastic deformation force of the sample as a result of the indentation and the indentation depth at this point is the minimum indentation depth which can ever be achieved. Under ambient conditions, SLS is covered with a layer of water. This implies that capillary forces will act as the leading attractive force in the jump-to-contact process.[20, 21]

3.3.2 Capillary Force

Capillary force arise as the liquid meniscus forms between two hydrophilic solid surfaces approaching each other.[22] Figure 3.1 shows a schematic view of the indenter-sample interaction under capillary force. The two small circles with radius of r represent the liquid meniscus formed around the indenter. The bigger circle with a radius of R represents the indenter. d is the indentation depth. β is called the filling angle which defines the three phase (indenter, air and liquid) contact position. h is the liquid-indenter contact radius:

$$h = Rsin\beta \tag{3.1}$$

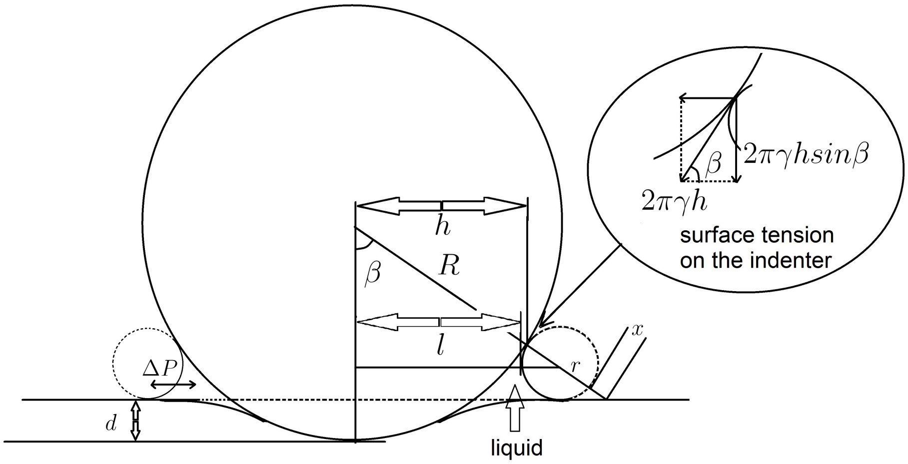

Figure 3.1: Indentation under the influence of capillary forces. The liquid meniscus and indenter sizes are not drawn to scale: the meniscus is enlarged for better view. R is the radius of curvature of the indenter, r is the liquid meniscus radius, l is the distance between the vertical tangent of the liquid meniscus and the vertical center line of the indenter, d is the indentation depth, ΔP is the capillary pressure, β is the filling angle, h is the indenter-liquid contact radius, $2\pi\gamma h$ is the indenter-liquid surface tension force and $2\pi\gamma h sin\beta$ is the vertical component of the indenter-liquid surface tension force.

l is azimuthal radius measure the distance between the vertical tangent of the liquid meniscus and the vertical center line of the indenter. When $r << R$, l can be approximately calculated as:

$$l \approx h = R sin\beta \tag{3.2}$$

Here it is assumed that both the contact angles of the liquid to the sample surface and the indenter are zero. This assumption may introduce some error since these angles are not absolutely zero.[22] However, for our experiments in which water is the liquid, these angles are very close to zero and this approximation should fairly represent the real situation.[23]

The meniscus curvature will induce a pressure difference (ΔP) across the water-air interface:

$$\Delta P = \gamma(\frac{1}{r} - \frac{1}{l}) \approx \gamma\frac{1}{r}\ (r << l) \tag{3.3}$$

where r is the liquid meniscus radius and γ is surface tension of water. This pressure difference exerts an attractive force F_a on the indenter:

$$F_a = \pi l^2 \Delta P = \pi \gamma R^2 sin^2 \beta \frac{1}{r} \tag{3.4}$$

There is also the surface tension on the indenter. The surface tension force is proportional to the length of the contact ($2\pi h$) and tangent to the liquid-sample contact point. However, only the vertical component of this force will be effective: the horizontal component is canceled out due to the shape of this contact profile (circle). Therefore, the net surface tension on the indenter F_s is

$$F_s = 2\pi\gamma h sin\beta = 2\pi\gamma R sin^2\beta \tag{3.5}$$

The capillary force is the sum of the two aforementioned forces:

$$F_c = F_a + F_s = \pi\gamma R sin^2\beta(2 + \frac{R}{r}) \tag{3.6}$$

β can be calculated according to the geometry of the sample-indenter contact:

$$cos\beta = \frac{R - d}{R + 2r + x} \tag{3.7}$$

x is an introduced parameter shown in Figure 3.1. r can be calculated according to the Kelvin equation:

$$-\frac{lnH}{\lambda_k} = \frac{1}{r} - \frac{1}{l} \tag{3.8}$$

in which H is the relative humidity and λ_k is the Kelvin length for water. In experimental conditions, at around 25 °C, $\lambda_k = 0.523$ nm. Because $l >> r$, Equation 3.8

can be simplified as

$$r = -\frac{\lambda_k}{lnH} \tag{3.9}$$

In the minimum indentation experiments, d is normally less than 10 nm, R is 50 nm for our indenter, and $x << R + 2r$, so Equation 3.7 can be modified to

$$cos\beta = \frac{R-d}{R-2\frac{\lambda_k}{lnH}} \tag{3.10}$$

By combining Equations 3.6, 3.9 and 3.10, the capillary force is obtained:

$$F_c = \pi\gamma R(1-(\frac{R-d}{R-2\frac{\lambda_k}{lnH}})^2)(2-R\frac{lnH}{\lambda_k}) \tag{3.11}$$

Here the relationship $sin^2\beta = 1 - cos^2\beta$ is applied.

3.3.3 Elastic Deformation under Capillary Force and Jump-to-Contact Phenomenon

From the discussion above it is clear that the capillary force is an attractive force between the indenter and the sample. This attractive force will create indentation on the sample. The deformation of the sample is mostly elastic due to the nanometer size indentation depth and can be calculated according to the Johnson-Kendall-Roberts (JKR) or Derjaguin-Muller-Toporov (DMT) models.

The DMT model of elastic deformation relates the reduced Young's modulus E^* to the force by:[24]

$$F_e = \frac{4}{3}E^*R^{0.5}d^{1.5} \tag{3.12}$$

The JKR model of elastic deformation results in a different expression:[25]

$$F_e = \sqrt{16\pi\gamma E^*a^3} \tag{3.13}$$

d is the indentation depth and a is the contact radius. For minimum indentation where $d << R$

$$a^2 = 2Rd \tag{3.14}$$

Equation 3.13 can be expressed as

$$F_e = \sqrt{16\pi\gamma E^*(2Rd)^{\frac{3}{2}}} \tag{3.15}$$

and E^* is defined as

$$\frac{1}{E^*} = \frac{1-\nu_s^2}{E_s} + \frac{1-\nu_{in}^2}{E_{in}} \tag{3.16}$$

where E_s and E_{in} are the sample and indenter Young's moduli respectively and ν_s and ν_{in} are their Poisson's ratios respectively. For our SLS samples and AFM tip, $E_s << E_{in}$ and ν_s and ν_{in} are around 0.3. Therefore, Equation 3.16 can be approximated as

$$\frac{1}{E^*} = \frac{1-\nu_s^2}{E_s} \tag{3.17}$$

The modified Tabor coefficient (instead of the conventional Tabor coefficient in Section 1.3.2) is introduced to determine which model is applicable under certain conditions when the capillary force is dominant over other van der Waals forces:[21]

$$\mu = (\frac{R\gamma^2}{2E^{*2}r^3})^{\frac{1}{3}} \tag{3.18}$$

When $\mu >> 1$, the JKR model should be applied. When $\mu < 1$, the DMT model should be applied. In this study, the DMT model is applicable based on our material and test conditions.

The cantilever deflection force is much smaller than the sample elastic deformation force and can be neglected. The sample elastic deformation is created predominantly by the capillary force without externally applied mechanical force which is the main force in a normal indentation test. The use of the capillary force as the main force for indentation implements the idea of nanoindentation with minimum indentation depth on hydrophilic surfaces. At the minimum indentation depth, the sample elastic deformation force equals the capillary force:

$$F_e = F_c \tag{3.19}$$

In the force curves, the minimum indentation depth is hard to discern because of the jump-to-contact phenomenon and subsequent indentation event (Figure 3.2). Under humid conditions, a layer of water will be adsorbed to the hydrophilic surface. During the jump-to-contact event, a liquid bridge forms between the indenter and the sample due to the water layers on the indenter and the sample surfaces. The formation of the liquid bridge creates the liquid meniscus, hence the capillary force simultaneously takes effect. This dramatically increases the force between the indenter and the sample. The capillary force is much larger than the cantilever deflection force so that the indenter snaps to contact with the sample (point A in Figure 3.2). It will keep penetrating the sample until the capillary force is balanced by the sample elastic deformation force, creating indentation depth d (point B in Figure 3.2).

In a force curve, the jump-to-contact distance Δd includes the indenter-sample separation before the jump S_0 and the indentation depth d. However, there is no clear boundary to distinguish one from the other. Furthermore, in the lower panel of Figure 3.2 it can be seen that the free cantilever reference position barely changes from A to B. Therefore, the indentation depth can not be deduced from this force curve.

This can be solved by conducting a reference jump-to-contact test on a hard

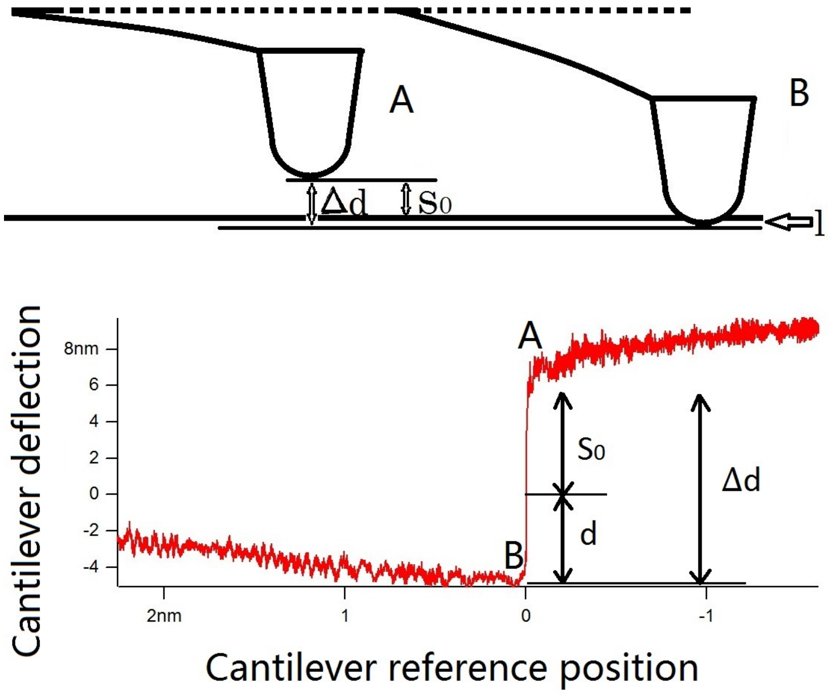

Figure 3.2: The jump-to-contact phenomenon under capillary force. The upper sketch shows the indenter jump-to-contact process. The lower sketch shows the jump-to-contact phenomenon measure by a force curve. The horizontal axis is the free (without external influence) cantilever reference position and the vertical axis is the cantilever deflection which measures the force on the indenter.

surface (like mica) on which the penetration is negligible under capillary force. Under the same humidity, capillary forces between the indenter and different surfaces are the same according to Equation 3.11. This implies that the indenter-sample separations between the indenter and different surfaces at the starting point of the jump-to-contact are the same. For mica, the jump-to-contact distance is the same as the indenter-sample separation at the starting point of jump-to-contact S_0 since the indenter will not penetrate the surface. For soft samples, the jump-to-contact distance is the indenter-sample separation at the starting point of jump-to-contact which is equal to the jump-to-contact distance on mica surface S_0 plus the indentation depth d. So the indentation depth on soft surface can be calculated:

$$d = \Delta d - S_0 \tag{3.20}$$

Combining Equations 3.6, 3.12, 3.17, 3.19 and 3.20, the sample elasticity can be obtained for DMT model:

$$E_s = \frac{3}{4}\pi\gamma R^{\frac{1}{2}}(1-\nu_s^2)(1-(\frac{R-\Delta d+S_0}{R-2\frac{\lambda_k}{lnH}})^2)(2-R\frac{lnH}{\lambda_k})\frac{1}{(\Delta d - S_0)^{\frac{3}{2}}} \tag{3.21}$$

Combining Equations 3.6, 3.15, 3.17, 3.19 and 3.20, the sample elasticity can be obtained for JKR model:

$$E_s = \frac{\pi\gamma(\frac{R}{2})^{\frac{1}{2}}}{32}(1-\nu_s^2)(1-(\frac{R-\Delta d+S_0}{R-2\frac{\lambda_k}{lnH}})^2)^2(2-R\frac{lnH}{\lambda_k})^2\frac{1}{(\Delta d - S_0)^{\frac{3}{2}}} \tag{3.22}$$

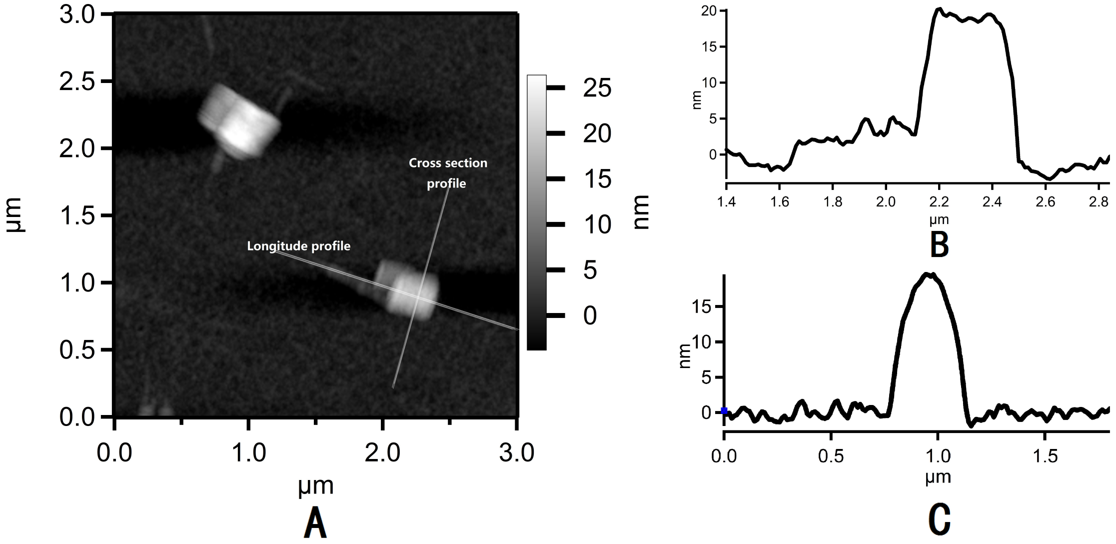

Figure 3.3: (A) AFM image of SLS. Straight lines indicate the location where surface profile is analyzed in the longitude direction (B) and cross section direction (C).

3.4 Results and Discussion

3.4.1 Morphology and Mechanical Properties of SLS

SLS should be cylindrical to maximize intermolecular interaction and minimize surface energy in solution. When it is deposited on mica, the structure is flattened to the mica surface by the attractive force between mica and the SLS: in Figure 3.3, the SLS cross section profile has a significantly larger width than height. We define here the longitudinal direction of an SLS along the monomer direction and the cross section perpendicular to the monomer.

The cross section and longitude profiles reveal that SLS is a saddle like structure with two big terminal ridges and several minor middle ridges. The length of the SLS is more than 350 nm which is longer than a collagen monomer which is about 300 nm. This discrepancy is understandable because the AFM images are the convolution of the tip geometry and the sample topology. The minor ridges are possibly caused

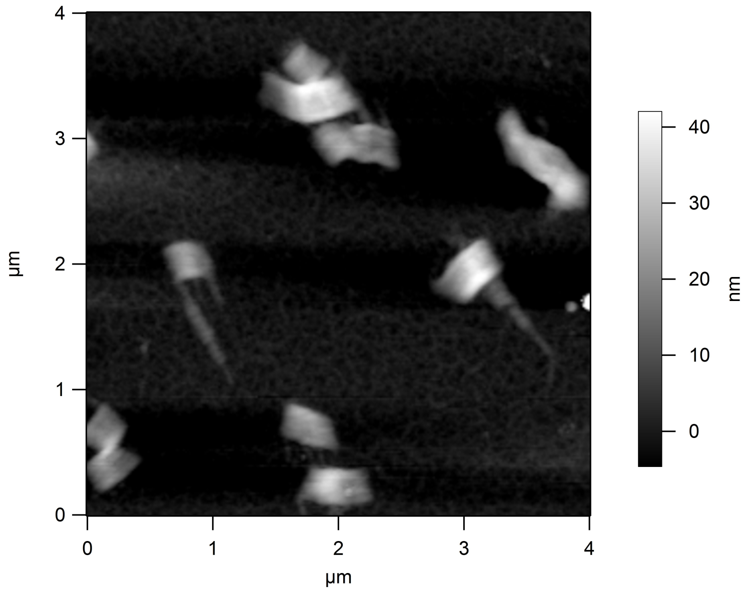

Figure 3.4: AFM image of SLS showing assocations between crystallites.

by local higher occupancy of amino acids with larger side chains. The two terminal major ridges are caused by the non-helical region of the N-terminus and C-terminus: the non-helical chains contains higher proportion of bigger amino acids and pack loosely which result in greater size compared with the helical regions. The two major ridges are not equal in size. In the monomer sequence, the C-terminus contains more non-helical amino acid residues than the N-terminus, and the non-helical amino acid residues in the C-termini may fold into a tight hairpin structure.[26] Therefore, the larger end may correspond to the C-terminus while the smaller end may correspond to the N-terminus. As a result, in the AFM images, the SLSs are trapezoidal (Figure 3.4).

Associations between SLS crystallites in AFM images such as Figure 3.4 could be a result of associations in solution or simply an artifact of colocation during drying. Even in the latter case, however, preferential orientation could imply a specific interaction between crystallites. In many cases they appear to align with smaller SLS crystallites attached to the N-terminus of larger ones.

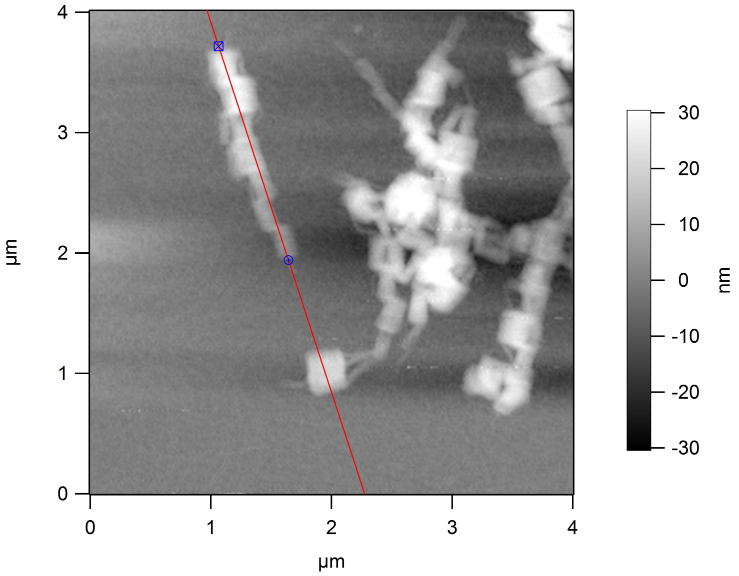

Figure 3.5: At a higher incubation temperature (35 °C), images show more SLS crystallites which also associate end-to-end in images of dried samples.

Incubation at elevated temperature results in more SLS formation and thus higher density of SLS in samples, resulting in images such as that seen in Figure 3.5. In analyzing these images, there is a dominance of longitudinal alignment with partial overlap of a consistent 50 nm. This overlap length is smaller than the displacement of the collagen monomers in the native fibril which is 67nm but larger than the terminal non-helical region length which is around 20nm. So one overlap contains about 40% helical structure and 60% non-helical structure. This arrangement increases the packing density and the interaction between adjacent SLSs in the overlap region.

Forty-one minimum nanoindentation force curves are taken at different locations of individual crystallites to ensure that the variability of the mechanical properties among different crystallites and different positions within one crystallite are carefully accounted for. The Young's modulus calculated from each force curve is plotted in Figure 3.6. The average SLS Young's modulus is calculated to be 0.41 ± 0.08 GPa. This value is close to the Young's modulus of type I collagen fibrils[27] and films.[28]

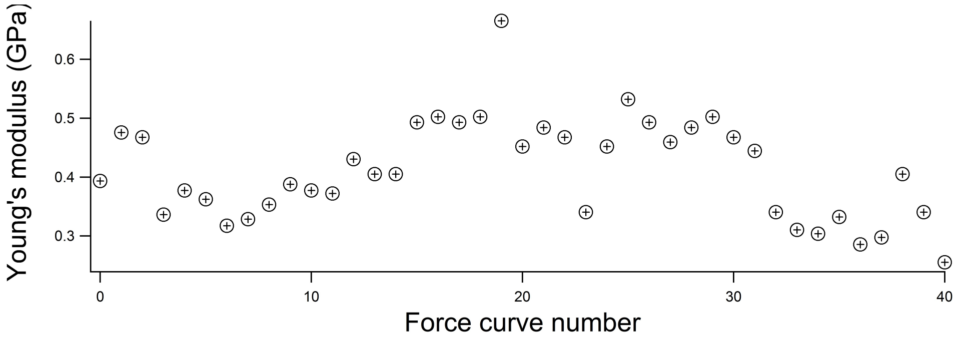

Figure 3.6: Distribution of the Young's modulus calculated from the 41 force curves.

The slight Young's modulus difference between the SLS prepared in this experiment and the type I collagen fibril reported in the literature can be explained by several reasons. First, the samples have different packing patterns. SLS are formed by monomers packing laterally in register while type I collagen fibrils are formed by monomer quarterly staggering. Second, the SLS samples and type I collagen fibrils may have different hydration states since the preparation methods are different. Third, additives used to prepare these two samples are different in terms of types and amount. Fourth, the sample substrates may be different for nanoindentation. Mica is used for SLS sample while other researcher use silicon wafers or glass slides. This would result in different interaction between the samples and substrates and potentially vary the mechanical behavior of the samples. Last but not least, the test methods are different. The SLS samples are tested with the novel minimum nanoindentation method while the fibrils are tested with traditional method. This minimum nanoindentation method resulted in a indentation depth less than 30% of the SLS thickness (Figure 3.3). This indentation depth is achieved under the capillary force without any additional externally imposed mechanical force which would create much large indentation depth value in a traditional nanoindentation test. Hence the substrate effect on the results is minimized.

Further analysis is carried out to check the difference in Young's moduli between end and middle regions by using Student's t-tests. 22 end region data points and 19 middle region data points in the total of 41 data points are tested. However, the p value (0.86) implies that there is no significant difference between them.

3.5 Summary

We proposed a method to obtain material Young's moduli at the minimum indentation under the influence of capillary force. This method is applied to measure the SLS Young's modulus and the result agrees with the literature value. The morphology of the SLS is studied. We revealed that the SLSs have trapezoidal shape and identified the C-terminus and N-terminus of the SLS. Under higher incubation temperature, images reveal chains of SLS crystallites. While this may simply reflect the larger number of crystallites formed under these conditions, which then dry adjacent to each other in the dried sample, the associations are consistent, which may imply a specific, favorable interaction between SLS crystallites.

Bibliography

[1] M. D. Shoulders and R. T. Raines. Collagen structure and stability. *Annual Review of Biochemistry*, 78:929–958, 2009.

[2] K. E. Kadler, A. Hill, and E. G. Canty-Laird. Collagen fibrillogenesis: fibronectin, integrins, and minor collagens as organizers and nucleators. *Current Opinion in Cell Biology*, 20:495–501, 2008. Cell-to-cell contact and extracellular matrix.

[3] F. O. Schmitt, J. Gross, and J. H. Highberger. A new particle type in certain connective tissue extracts. *Proceedings of the National Academy of Sciences of the United States of America*, 39:459–470, 1953.

[4] Y. Fujita, K. Kobayashi, and T. Hoshino. Atomic force microscopy of collagen molecules. Surface morphology of segment-long-spacing (SLS) crystallites of collagen. *Journal of Electron Microscopy*, 46:321–326, 1997.

[5] K. Kobayashi, T. Ito, and T. Hoshino. Correlation between negative staining pattern and hydrophobic residues of collagen. *Journal of Electron Microscopy*, 35:272–275, 1986.

[6] K. Kobayashi, J.-i. Niwa, T. Hoshino, and T. Nagatani. Electron microscopic visualization of collagen aggregates without chemical staining. *Journal of Electron Microscopy*, 41:235–241, 1992.

[7] R. R. Bruns and J. Gross. Band pattern of the segment-long-spacing form of collagen. Its use in the analysis of primary structure. *Biochemistry*, 12:808–815, 1973.

[8] A. J. Hodge and F. O. Schmitt. The charge profile of the tropocollagen macromolecule and the packing arrangement in native-type collagen fibrils. *Proceedings of the National Academy of Sciences of the United States of America*, 46:186–197, 1960.

[9] J. P. R. O. Orgel, T. C. Irving, A. Miller, and T. J. Wess. Microfibrillar structure of type I collagen *in situ*. *Proceedings of the National Academy of Sciences of the United States of America*, 103:9001–9005, 2006.

[10] S. Perumal, O. Antipova, and J. P. R. O. Orgel. Collagen fibril architecture, domain organization, and triple-helical conformation govern its proteolysis. *Proceedings of the National Academy of Sciences of the United States of America*, 105:2824–2829, 2007.

[11] R. R. Bruns, D. J. Hulmes, S. F. Therrien, and J. Gross. Procollagen segment-long-spacing crystallites: their role in collagen fibrillogenesis. *Proceedings of the National Academy of Sciences of the United States of America*, 76:313–317, 1979.

[12] L. Bonfanti, A. A. Mironov Jr., J. A. Martínez-Menárguez, O. Martella, A. Fusella, M. Baldassarre, R. Buccione, H. J. Geuze, A. A. Mironov Jr., and A. Luini. Procollagen traverses the golgi stack without leaving the lumen of cisternae: evidence for cisternal maturation. *Cell*, 95:993–1003, 1998.

[13] R. L. Trelstad, K. Hayashi, and J. Gross. Collagen fibrillogenesis: intermediate aggregates and suprafibrillar order. *Proceedings of the National Academy of Sciences of the United States of America*, 73:4027–4031, 1976.

[14] T. Koide and K. Nagata. Collagen biosynthesis. *Topics in Current Chemistry*, 247:85–114, 2005.

[15] E. Leikina, M. V. Mertts, N. Kuznetsova, and S. Leikin. Type I collagen is thermally unstable at body temperature. *Proceedings of the National Academy of Sciences of the United States of America*, 99:1314–1318, 2002.

[16] B. Eyden and M. Tzaphlidou. Structural variations of collagen in normal and pathological tissues: role of electron microscopy. *Micron*, 32:287–300, 2001.

[17] K.-C. Chang, Y.-W. Chiang, C.-H. Yang, and J.-W. Liou. Atomic force microscopy in biology and biomedicine. *Tzu Chi Medical Journal*, 24:162–169, 2012.

[18] M. F. Paige and M. C. Goh. Ultrastructure and assembly of segmental long spacing collagen studied by atomic force microscopy. *Micron*, 32:355–361, 2001.

[19] J. L. Hutter. Comment on tilt of atomic force microscope cantilevers: effect on spring constant and adhesion measurements. *Langmuir*, 21:2630–2632, 2005.

[20] T. Eastman and D. Zhu. Adhesion forces between surface-modified AFM tips and a mica surface. *Langmuir*, 12:2859–2862, 1996.

[21] Y. Xu, G. Balooch, M. Chiou, E. Bekerman, R. O. Ritche, and M. T. Longaker. Analysis of the material properties of early chondrogenic differentiated adipose-derived stromal cells (ASC) using an *in vitro* three-dimensional micromass culture system. *Biochemical and Biophysical Research Communications*, 359:311–316, 2007.

[22] H. Butt and M. Kappl. Normal capillary forces. *Advances in Colloid and Interface Science*, 146:4–60, 2009.

[23] H. Butt, W. J. P. Barnes, A. del Campo, M. Kappl, and F. Schonfeld. Capillary forces between soft, elastic spheres. *Soft Matter*, 6:5930–5936, 2010.

[24] V. M. Muller, B. V. Derjaguin, and Y. P. Toporov. On two methods of calculation of the force of sticking of an elastic sphere to a rigid plane. *Colloids and Surfaces*, 7:251–259, 1983.

[25] I. Sridhar, K. L. Johnson, and N. A. Fleck. Adhesion mechanics of the surface force apparatus. *Journal of Physics D: Applied Physics*, 30:1710–1719, 1997.

[26] J. P. Orgel, T. J. Wess, and A. Miller. The *in situ* conformation and axial location of the intermolecular cross-linked non-helical telopeptides of type I collagen. *Structure*, 8:137–142, 2000.

[27] C. A. Grant, D. J. Brockwell, S. E. Radford, and N. H. Thomson. Tuning the elastic modulus of hydrated collagen fibrils. *Biophysical Journal*, 97:2985–2992, 2009.

[28] M. R. Kumar, E. F. Merschrod S., and K. M. Poduska. Correlating mechanical properties with aggregation processes in electrochemically fabricated collagen membranes. *Biomacromolecules*, 10:1970–1975, 2009.

Chapter 4

Fibrillogenesis and Nanomechanics of Type I Collagen Fibrils

Type I collagen fibrils prepared with the “cold start” method form with a sequential process, as revealed by monitoring fibril morphology with the atomic force microscope (AFM) at different stages. Three distinctive growth stages can be defined. The fibrils are polar in nature with transition from unipolar structure to bipolar structure. The Oliver-Pharr method is applied to extract the indentation Young’s modulus of individual fibrils. The bending modulus of collagen fibrils is deduced from their persistence length. A significant difference is found between these two mechanical parameters. This could be attributed to the fibril packing pattern, hydration states and substrate effects.

4.1 Introduction

Collagen is an indispensable component of most mammalian connective tissues. There are more than 26 different types of collagen.[1] Type I and type II collagen are the most abundant collagen and can be found in bone, skin and tendon. Defects (*e.g.* mutation) in collagen can lead to various health problems like osteogenesis imperfecta and Caffey's disease.[2, 3] Damage or degradation of these collagen containing tissues can also cause serious medical condition like arthritis.[4] The treatment of collagen related disease and tissue repairing need more understanding in collagen.[5] Research on collagen is beneficial for health and medical care.[6]

Type I and type II collagen are macromolecules about 300 nm long and 1.5 nm in diameter.[5] They can form larger fibrils with a periodic banded structure (so-called D-banding, with a repeat every 67 nm).[7] The periodicity of this banded structure is about one-fourth of the length of a monomer and is therefore purported to arise from a quarter-stagger arrangement of monomers. The monomers are right-handed coils consisting of three left-handed peptide helices. All of their peptide chains are composed of repeating Gly-X-Y units, with Gly being glycine residue and X and Y representing other amino acid residues. The other amino acid residuals are mostly proline or hydroxyproline residues. A type I collagen monomer contains two collagen $\alpha 1$(I) chains and one collagen $\alpha 2$(I) chain. The spatial relationship among the two $\alpha 1$(I) and one $\alpha 2$(I) peptide chains was solved by comparing the charge distribution of model monomers and SLS.[8] The collagen monomer starts with one $\alpha 2$(I) chain followed by another $\alpha 2$(I) chain and then the $\alpha 2$(I) chain on the N terminus.

For type II collagen, all three peptides are collagen $\alpha 1$(II) chains. This may result in their ultimate different roles in connective tissue. For example, type I collagen associates with hydroxyapatite, making bones strong and flexible to support body weight and stress,[9] while type II collagen associates with proteoglycans, making bone joints elastic and resilient to resistive friction.[10]

Their different mechanical properties in macroscopic objects promotes us to investigate their mechanical properties in microscopic forms such as fibrils. A better understanding of the micro fibril mechanical properties is crucial for tissue repair, treatment of diseases caused by genetic defect, and biomimetic material research. This chapter presents results on type I collagen.

To determine the mechanical properties, several parameters can be considered. Young's modulus is one of the most common and important parameters.[11] Collagen fibrils are anisotropic materials.[12] They are formed by packing individual collagen monomers laterally and longitudinally which means one can not expect the Young's modulus along the fibril E_1 being the same as the Young's modulus transverse to the fibril E_2 (Figure 4.1). There are also other moduli like shear moduli.[13] They are more complicated to obtain, and hence will not be addressed here.

The diameters of collagen fibrils range from several nanometers to a few micrometers.[14–17] Their lengths vary from more than 300 nm (the length of a single collagen monomer) to several hundreds of micrometers. Their small size poses technique challenge for experiment setup since locating and manipulating these kind of small objects is not an easy task. Several methods are developed to extract Young's moduli of small objects based on different theories and techniques. In the early days, microcomponent mechanical behavior was deduced from the mechanical properties of macroscale bulk objects.[18] Naoki and Singo performed X-ray diffraction on force-loaded collagen fibers.[19] Because the X-ray diffraction pattern reflects the monomer lattice spacing, they deduced the strain of the collagen monomers under different stress and obtained the Young's modulus of individual collagen monomers along the molecular axis.

The invention of atomic force microscopes (AFMs) enabled researchers to locate and manipulate nanometer-sized objects. Nanoindentation experiments were carried out with the AFM to determine the Young's modulus transverse to the collagen fibril axis.[20, 21] Tensile tests of a collagen fibril were implemented by attaching one end of the fibril to a substrate and the other end to the AFM cantilever.[22] When stretching the fibril, a force versus cantilever position plot is obtained. Then Young's modulus along the fibril axis can be calculated from this plot. The bending behavior of a single collagen fibril was also investigated by several researchers.[23–25] This bending test can generate bending Young's modulus, a measurement of fibril flexibility. The bending Young's modulus can also be calculated from the hydrodynamic behaviour of fibrils in fluid[26] . In other studies, fibril persistence length was derived from fibril conformations observed under the microscope and was further used to compute the bending modulus.[27]

In this study, nanoindentation tests are performed on individual collagen fibrils to obtain transverse Young's moduli. The trajectories of the collagen fibrils in the AFM images are analyzed to obtain bending Young's moduli.

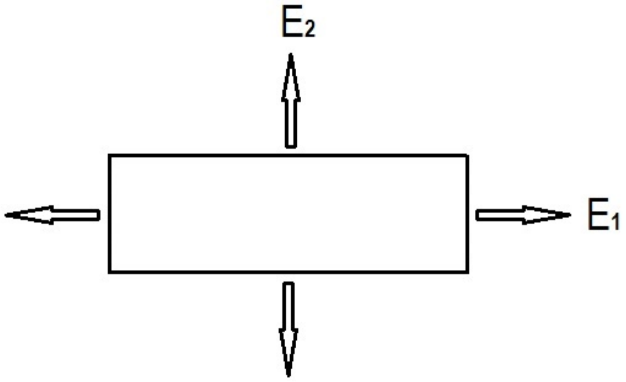

Figure 4.1: Young's moduli of a fiber in different directions. The collagen monomers stagger with each other in the horizontal direction. This anistropic structure results in different mechanical properties in the horizontal direction and the vertical direction.

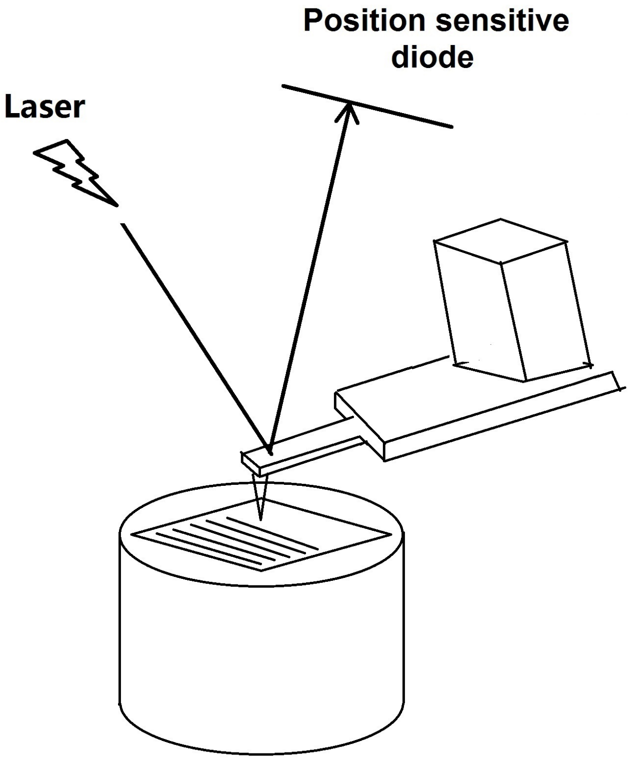

Figure 4.2: A schematic of the atomic force microscope (AFM).

4.2 Theory

4.2.1 Atomic Force Microscope and Nanoindentation

The AFM is a special microscope developed to map the sample surface profile at nanometer resolution (Figure 4.2).[28] During operation, a sharp probe which is fixed to one end of a cantilever is scanned over a chosen area on the sample. The gap between the probe and sample is controlled to nanometer scale. In that close range, several forces may present, including van der Waals forces, electrostatic forces, capillary forces. At some distance, one type of force may be more prominent than others since the mathematical force-distance relationships differ from one another.[29–31] These forces deflect the cantilever. By recording the deflection of the cantilever, the total force between the probe and the sample can be quantified:

$$F = k \times d \tag{4.1}$$

where F is the force between the probe and sample, k is the cantilever spring constant, and d is the the cantilever deflection.

The measurement of the cantilever deflection is achieved by projecting a beam of laser light on the end of the cantilever. The laser beam is then reflected to a photodiode panel which can detect the position of the reflected laser spot on the photodiode. The probe-sample force induces the cantilever deflection and in turn changes the laser spot position on the photodiode.

The probe-sample force can be finely adjusted with nanonewton accuracy by mounting the cantilever on a piezoelectric tube whose length will change proportionally to the applied electric potential.[28] The cantilever then moves vertically to the appropriate probe-sample distance to apply a given force. Additional piezoelectric elements control the lateral movement of the probe or the sample. To generate a sample surface profile image, the probe-sample force is set to a certain value. Then as the lateral piezoelectric elements move, the vertical piezoelectric tube will adjust the probe-sample distance to maintain a constant interaction force. All coordinates (x, y, z) of the probe at each sample point are recorded and stored to produce the sample surface profile image.

There are different operation modes for AFM.[32–34] Contact mode and tapping mode are most common. In tapping mode, the cantilever is oscillated slightly above its resonant frequency so that the probe is in intermittent contact with the sample. In contact mode, the probe is not oscillated but kept in constant contact with the sample. In this study, tapping mode is applied to characterize the sample morphology.

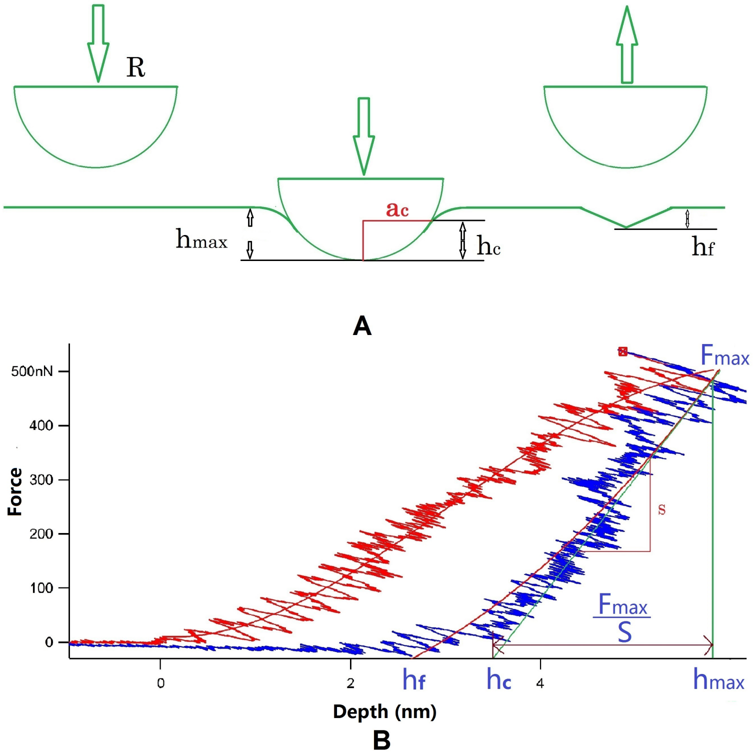

Figure 4.3: Nanoindentation process schematic (A) and sample force curve (B).

The AFM allows researchers to carry out nanoindentation tests with sub-nanometer depth and sub-nanonewton force resolution. In nanoindentation testing, the ultra sharp AFM probe acts as the indenter. During the loading and unloading process, the indenter-sample force and indenter position are recorded. These values are then plotted to make a force curve graph (Figure 4.3).

As outlined in Figure 4.3A, when performing a nanoindentation test the indenter is pressed into the sample surface to create sample deformation. Then the indenter is moved back, leaving a residual indent if there is plastic deformation. The maximal indentation depth is h_{max}, which is larger than the contact depth h_c because of sample surface deflection near the indenter. The contact radius is a_c from which the contact area can be calculated. The final indentation depth is h_f which is caused by inelastic deformation of the sample. The force curve in Figure 4.3B is generated by plotting force *vs.* indentation depth. The red curve is the approaching curve and the blue curve is the retracting curve. S is the stiffness which is obtained by measuring the slope of the tangent at the maximum unloading point. h_c is also shown in this plot.

Several theories are proposed to analyze the force curve and calculate the material Young's modulus.[35–38] The Oliver-Pharr method is most commonly used.[39] A mentioned above, because of sample surface deflection due to elastic deformation near the indenter, the contact depth (h_c) is smaller than the maximum indentation depth (h_{max}). For a spherical indenter (the apex of our AFM probe is treated as a half sphere), they are related as

$$h_c = h_{max} - 0.75\frac{F_{max}}{S} \tag{4.2}$$

Based on the geometry of the indenter (half sphere with a radius of r), the contact radius a_c can be calculated:

$$a_c = \sqrt{r^2 - (r - h_c)^2} \tag{4.3}$$

The projected area of contact A is

$$A = \pi a_c^2 \tag{4.4}$$

The contact area A and measured stiffness S are related to the reduced Young's modulus (E_r):

$$E_r = \frac{\sqrt{\pi}}{2}\frac{S}{\sqrt{A}} \tag{4.5}$$

E_r is determined from the indenter Young's modulus E_{in} and Poisson's ratio ν_{in}

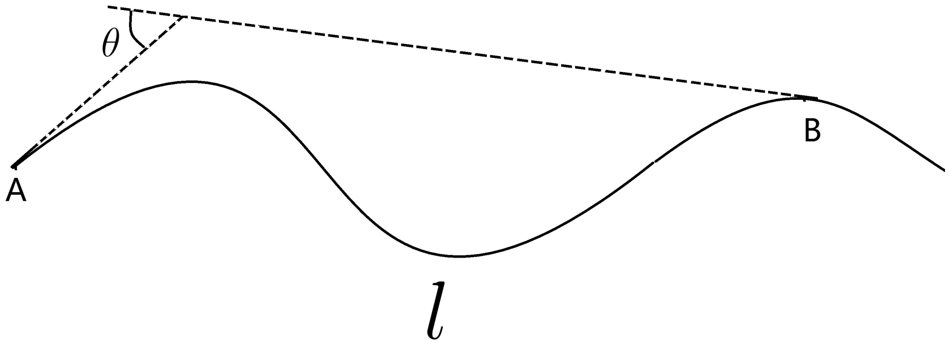

Figure 4.4: Geometrical parameters used in calculating persistence length. θ is the angle between the tangent at point A and the tangent at point B. l is the contour length between A and B.

and the sample Young's modulus E_s and Poisson's ratio ν_s. They are related as

$$\frac{1}{E_r} = \frac{1-\nu_{in}^2}{E_{in}} + \frac{1-\nu_s^2}{E_s} \tag{4.6}$$

For biological samples, $E_s << E_{in}$, ν_s is between 0.2 and 0.5 and ν_{in} is around 0.3. So Equation 4.6 can be approximated as

$$\frac{1}{E_r} = \frac{1-\nu_s^2}{E_s} \tag{4.7}$$

Combining Equations 4.2, 4.3, 4.4, 4.5 and 4.7, the sample Young's modulus is obtained

$$E_s = \frac{(1-\nu_s^2)S}{2\sqrt{r^2 - (r - h_{max} + 0.75\frac{F_{max}}{S})^2}} \tag{4.8}$$

4.2.2 Persistence Length

Persistence length measures the flexibility of a filament.[40] In solution, a long and soft filament will respond to the random impacts from the solvent leading to thermal fluctuations along the filament. As a result, the filament will adopt a conformation which can be represented by the trajectory of a single particle undergoing Brownian motion. Therefore, the configuration of a filament in solution can be explained by statistical thermodynamics. The persistence length (L_p) and contour length (l) (Figure 4.4) are related as:[27]

$$\langle \cos\theta \rangle_{3D} = \exp\left(\frac{-l}{L_p}\right) \tag{4.9}$$

$3D$ indicates that the filament is in three-dimensional space. θ is the angle between two tangent vectors separated by contour distance l along the filament. Equation 4.9 indicates that the correlation between these two tangent vectors decays exponentially with contour distance.

In an AFM image, the filament trace can be viewed as the projection of the 3D filament conformation onto 2D space. Accordingly, Equation 4.9 must be modified to account for this difference:[41]

$$\langle \cos\theta \rangle_{2D} = exp\left(\frac{-l}{2L_p}\right) \tag{4.10}$$

This equation can be further simplified as[41]

$$\langle \theta^2 \rangle_{2D} = \frac{l}{L_p} \tag{4.11}$$

The persistence length L_p, bending modulus E_b and filament diameter d are related:[22]

$$L_p = \frac{\pi E_b}{64 k_b T} \times d^4 \tag{4.12}$$

k_b is the Boltzmann constant and d is the filament diameter.

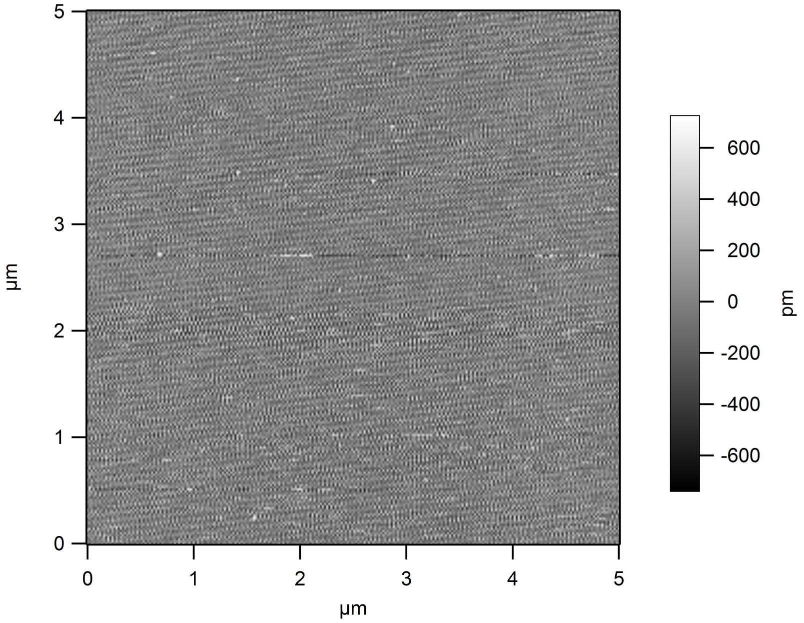

Figure 4.5: AFM image of a mica surface

4.3 Materials and Experimental Methods

Type I collagen (Advanced Biomatrix, with brand name Nutragen) is supplied as 6 mg/ml bovine hide collagen dissolved in 0.01 N HCl. Collagen fibrils are prepared by the "cold start" process.[42] In this method, collagen is mixed with buffer solution (containing 0.1 M K_2HPO_4 and 0.1 M KH_2PO_4) to make a solution with 0.05 M K_2HPO_4, 0.05 M KH_2PO_4 and 0.1 mg/ml collagen. The solution pH is adjusted to 7.0 by adding 0.01 M HCl or 0.01 M NaOH solutions. The sample is then incubated in a closed conical tube at 35 °C in a water bath. The solution pH stays around 7 during the experiment process.

Every 10 minutes, 10 μl solution is removed and diluted 100 times with ultrapure water. Then 10-20 μl of diluted solution is deposited on a freshly cleaved mica surface with a pipette. The cleaved mica surface provides a flat substrate which minimizes the effect of substrate roughness and improves image quality. (The subnanometer flatness of cleaved mica is shown in Figure 4.5.) The sample is dried with a stream of dry, filtered compressed air for about 5 minutes and then mounted on the AFM stage for analysis.

All AFM experiments are performed under ambient conditions using an Asylum Research MFP-3D. The AFM tips are MikroMasch NSC35/CR-AU tips with a factory specified radius of approximately 50 nm. The apex of the tip is a half sphere which is verified by scanning electron microscopy (Figure A.1). The spring constant of the cantilever is determined by the thermal noise method.[43] Tapping mode is employed for fibril imaging and nanoindentation is performed on individual fibrils to generate force curves. Persistence length is analyzed with the software 2D Single Molecules.[44] The fibril contour is drawn by tracing along the fibril direction. Then the program equally subdivides the contour curves into variable length vectors. These vectors are then analysed by Equation 4.10 to calculate persistence length.

4.4 Results and Discussion

4.4.1 Fibrillogenosis of Type I Collagen

The type I collagen fibrillogenesis mechanism is investigated by preparing AFM samples from incubated solution every 10 minutes. The results are shown in Figure 4.6. Three fibrillogenesis stages can be distinguished from the AFM images in Figure 4.6. The observation is consistent with literature.[45] Some fibrils formed after 10 minutes of incubation (panel A) show that a fibril has a tapered end and a blunt end. After 20 minutes of incubation (panel B), some fibrils have a tapered end and a blunt end while others, especially longer fibrils, have two tapered ends. After 30 minutes of incubation, the association between different filaments can be seen in panel C. After 40 minutes of incubation, most fibrils are too long to be completely captured within the image (panel D). However, the fibril ends which do appear in the image are mostly tapered.

4.4.1.1 Stage I, Unipolar Structured Fibrils

After 10 minutes, there are lots of filaments around 330 nm long and 1-2 nm high (Figure 4.6 A), corresponding to the dimensions of a collagen monomer. (AFM images are the convolution of the AFM probe geometry and sample surface features.[46] Therefore, the diameters should be measured by the heights rather than the widths.) The filaments with larger length could be aggregates of several collagen monomers, formed by staggering two or more monomers laterally. These aggregates serve as nucleation centers for further fibrillogenesis.

Most filaments possess a tapered end and a blunt end. For the collagen monomer, the end with an unreacted amino group is called the N-terminus and the end with an unreacted carboxyl group is call the C-terminus. The C-terminus is always larger than the N-terminus.[47] Two reasons may contribute to this morphology. First, there are more non-helical amino acid residues in the C-terminus. Second, the two $\alpha 1$ chains in the C-terminus may fold into into a tight hairpin structure. Therefore, in a single collagen monomer the thin end corresponds to the N-terminus and the blunt end corresponds to the C-terminus. In a fibril, all the monomer C-termini will point to one end of the fibril and all the monomer N-termini will point to the other end of the fibril. The fibril end with monomer C-termini is assigned as the fibril C-terminus and the fibril end with monomer N-termini is assigned as the fibril N-terminus.[48] The fibril growth will only occur on the N-terminus in stage I fibrillogenesis.[45] This growth pattern makes the fibril N-terminus tapered and the C-terminus blunt. So in the AFM image, the filament tapered ends correspond to the N-termini and the blunt ends correspond to the C-termini. This alignment is called C-N unipolar arrangement.

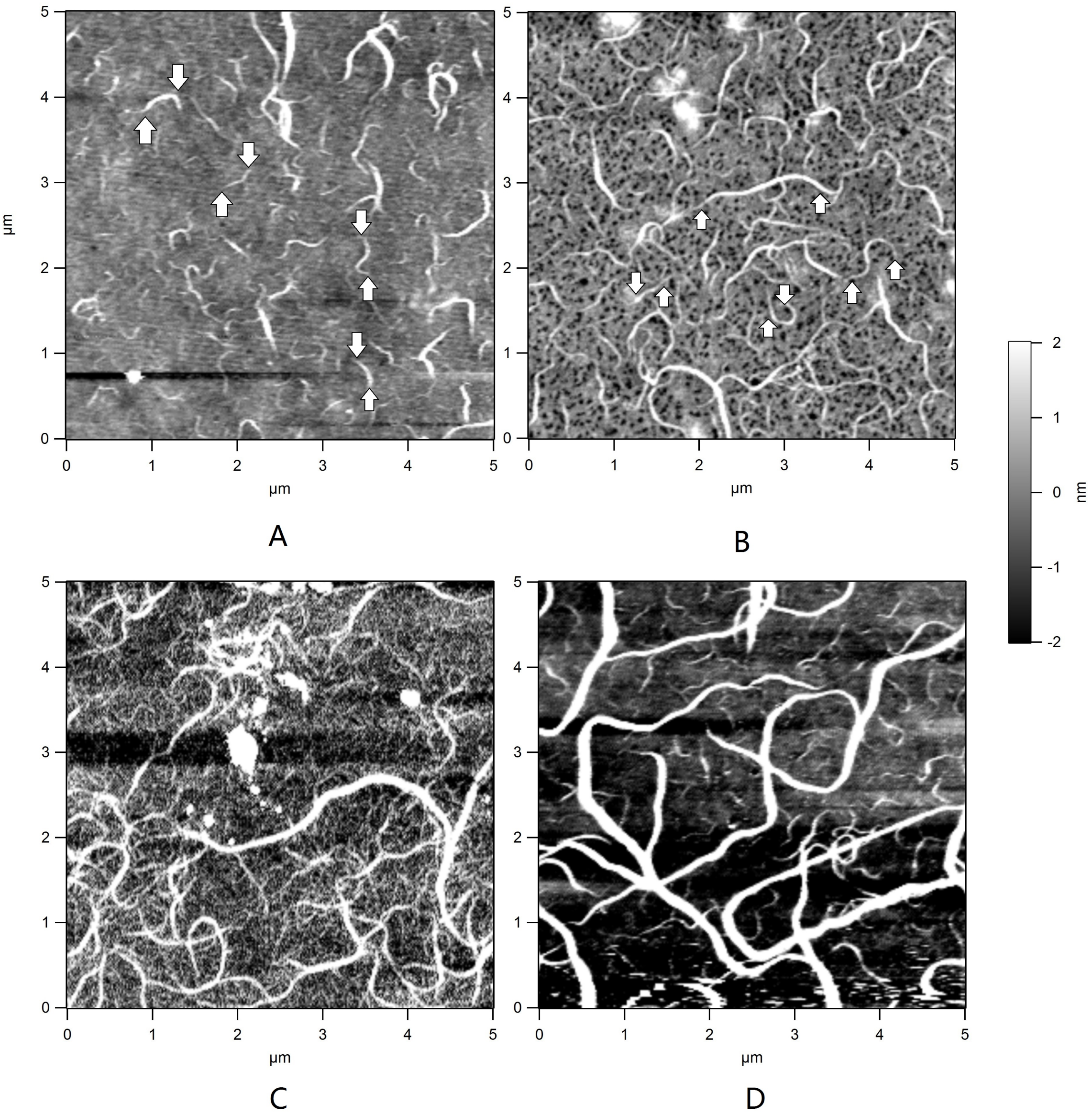

Figure 4.6: Fibrillogenosis process of collagen fibrils after (A) 10 minutes, (B) 20 minutes, (C) 30 minutes, and (D) 40 minutes of incubation. Upward pointing arrows indicate the tapered ends (N-termini) and downward pointing arrows indicate the blunt ends (C-termini).

4.4.1.2 Stage II, Bipolar Structured Fibrils

After 20 minutes, filaments in their different development stages can be seen in the AFM images (Figure 4.6 B). There are some short stage I aggregates with a tapered end and a blunt end. These filaments are less than 600 nm long. Other filaments grow to an intermediate stage. Their length reaches between 800 nm and 1200 nm. Their diameters increase a little, but not so significant as the increase in length. The tapered ends become more tapered and the blunt ends become slightly rounded. This growth pattern indicates that stage I filaments would grow preferably longitudinally rather than laterally. The more tapered N-terminus suggests that the fibril growth occurs mostly in the N-terminus. The slightly rounded C-terminus may be due to staggering in monomer packing along with the N-terminus preferred growth.[45, 49]

For the longer filaments, both ends become tapered. This implies that both ends of a filament are N-termini.[45] This development stage is called stage II. The alignment in this stage is N-N bipolar. So there is a transition from the C-N unipolar alignment to N-N bipolar alignment. For most stage II filaments, one end is more tapered than the other. The more tapered end may evolve from the the early stage filament N-terminus which grows faster. The less tapered end could be developed from the C-terminus which needs time to start grow in the C-terminus direction.

After 30 minutes, filaments grow thicker and longer (Figure 4.6 C). They can reach more than 3 μm in length and 5 nm in diameter. This is another intermediate stage between stage II and stage III (mature fibrils).[50] Most monomers disappear in this intermediate stage. With more monomers being consumed, filament growth would depend on absorbing surrounding aggregates. This can be confirmed by the association among different filaments in the AFM image.

4.4.1.3 Stage III, Mature Fibrils

After 40 minutes (Figure 4.6 D) fibril length reaches more than 5 μm (extending beyond the image boundaries). The fibril diameter also increases to more than 10 nm. Samples incubated longer than 40 minutes show minimal change in filament dimensions, implying that mature (stage III) collagen fibrils form by 40 minutes of incubation. Only tapered ends can be observed in the AFM images: the mature fibrils prepared in this study are N-N bipolar fibrils.

4.4.1.4 Driving Forces for Fibrillogenesis

The hydrophobic groups in the collagen monomer tend to interact with each other in solution. Intramolecular hydrophobic interaction is negligible since the monomer bending stiffness (see Section 4.4.2) prevents hydrophobic groups within the same monomer from interacting with each other. There is no such steric restriction for the intermolecular hydrophobic interactions. The intermolecular hydrophobic interactions induce the monomers to associate with each other and form fibrils instead of a globular structure which would be more likely if intramolecular interactions were strong.

The fibrillogenesis process is driven by entropy.[51] When fibrils grow, more hydrophobic groups in the collagen monomers are buried inside the fibrils. This leaves only the hydrophobic groups on the surface of the fibrils exposed to water. Aggregation leads to a decrease in entropy of the collagen. However, more water molecules are "freed" from bonding to collagen when fibrils form, resulting in an increase of the entropy of water. The increase of water entropy is larger than the decrease of the collagen entropy, such that the total entropy increases in the fibrillogenosis process. This drives the collagen monomers and small aggregates to associate to form fibrils. However, the entropy increase is not so significant when mature fibrils associate (fewer water molecules are freed per collagen monomer in the mature fibrils), limiting the

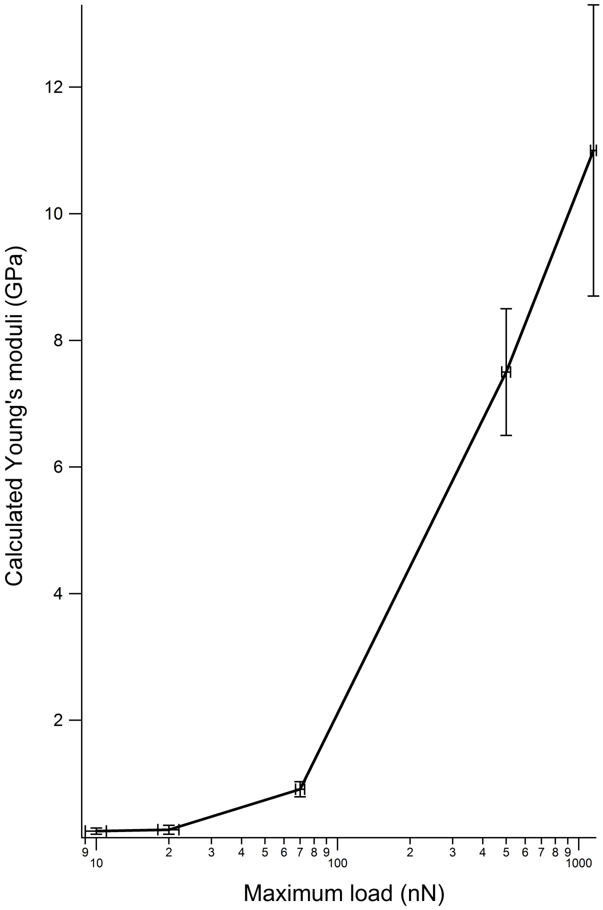

Figure 4.7: The effect of maximum load on calculated Young's moduli.

mature fibril size.

4.4.2 Mechanical Properties

4.4.2.1 Fibril Young's Moduli

Nanoindentation on individual fibrils requires optimization of measurement conditions because of the small diamaters of the fibrils. In particular, we investigate the effects of maximum load and fibril diameter on the calculated Young's moduli.

Figure 4.7 shows the effect of maximum load on the calculated Young's moduli. When the maximum loads are small (10-20 nN), the calculated Young's moduli

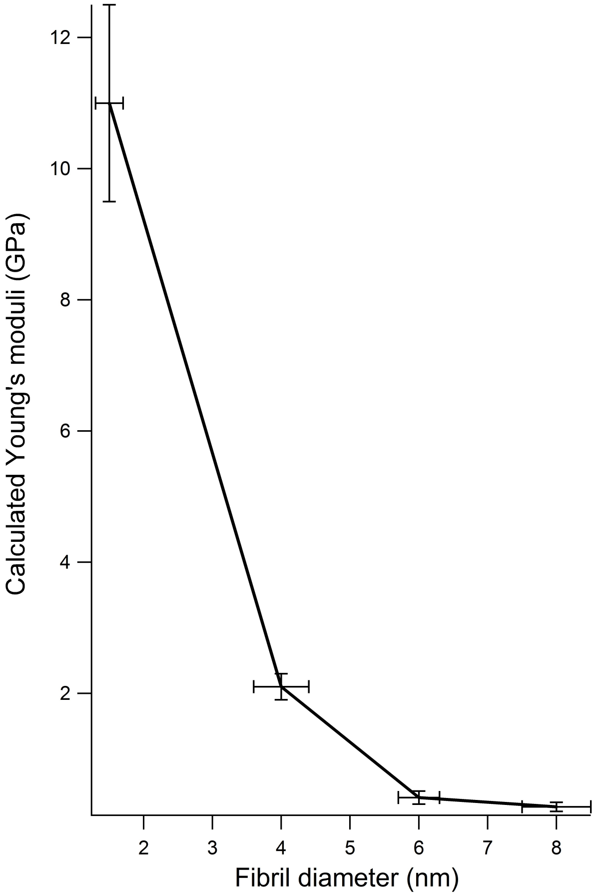

Figure 4.8: The effect of fibril diameter on calculated Young's moduli.

are close to each other ($p = 0.64$). As the maximum load increases, the calculated Young's moduli increase accordingly. This suggests that under small maximum load, the maximum load has negligible effect on calculated Young's moduli. Under larger maximum load, the maximum load will distort the calculated Young's modulus and make it larger than the real value. Under larger maximum load the indenter can penetrate the fibrils and make contact with the mica substrate. The calculated Young's moduli will therefore contain contributions from the mica substrate. The calculated error also increases for larger maximum load due to a greater contribution from the substrate. The range of possible Young's moduli increases since the measured Young's modulus increases from the Young's modulus of collagen to the Young's modulus of collagen and substrate combined. To avoid this, a small maximum load should be applied. Too small a maximum load should also be avoided since the the adhesion force may become comparable to the maximum load and make the calculated Young's modulus smaller than the real value.

Figure 4.8 illustrates the effect of fibril diameter on calculated Young's moduli. When fibril diameter increases, the calculated Young's modulus decreases. Under the same maximum load (20 nN), the contribution from the substrate is higher for fibrils with smaller diameter. The error bar is also larger for smaller fibrils. Both of the aforementioned phenomena can be attributed to the large deformation on small samples and the following inevitable substrate effect. Hence larger fibrils are more favorable in the nanoindentation test. Under optimum conditions (small maximum load and larger fibrils), the calculated Young's modulus of the fibrils is 0.27 ± 0.07 GPa. This value is in accordance with the literature value for hydrated type I collagen fibrils[20, 49] .

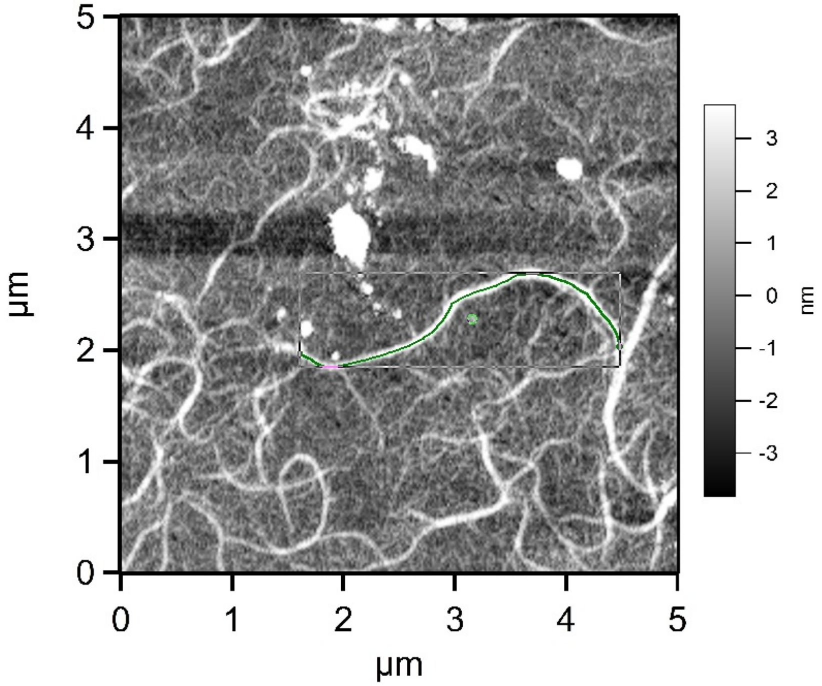

Figure 4.9: An example of persistence analysis with "2D Single Molecules".[44]

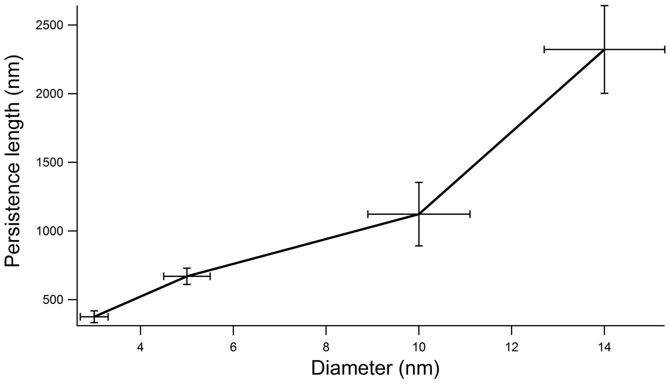

Figure 4.10: Persistence length L_p versus diameter d.

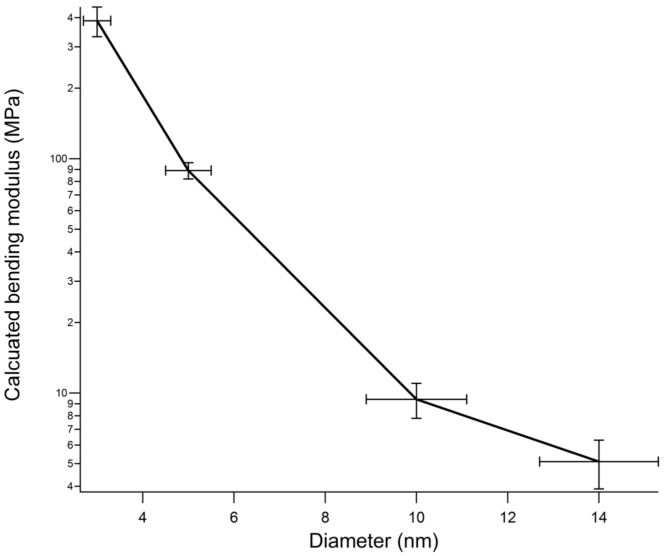

Figure 4.11: Bending modulus E_b versus diameter d.

4.4.2.2 Fibril Bending Moduli

The persistence length is calculated with the aid of the persistence length calculation application incorporated in the 2D Single Molecules[44] software. The contours of individual fibrils are selected (Figure 4.9) and the persistence length is computed.

A plot of persistence length against fibril diameter (Figure 4.10) shows that the persistence length increases as the diameter increases. This would be expected from Equation 4.12, which indicates that the persistence length should scale as the 4th power of the diameter for a given bending modulus. However, the relation is not that simple. When bending moduli are calculated according to Equation 4.12, using the experimentally measured values of L_p and d, they turn out to be dependent on fibril diameter as well. Figure 4.11 shows that the bending modulus decreases as the diameter increases.

The decrease of the bending modulus with the increase of the fibril diameter may be related to the internal structure of the fibrils. The collagen monomer bending modulus is the result of the compact association of three coiled peptides held together by hydrogen bonding,[5] which suggests that the individual monomer bending modulus could be fairly large. As the monomers aggregate to form fibrils, the forces between monomers are weaker than those within the monomer, primarily hydrophobic interactions. (Note that there is no chemical crosslinking present in our protocol.) As the fibril grows through additional weak association, the bending modulus decreases.

Above certain diameters (3 nm), the bending modulus become very low. The low bending modulus value originates from several factors. First, the fibrils are anisotropic due to the monomer lateral aggregation. Second, defects along the fibrils will concentrate the stress locally and significantly decrease the bending modulus.[52] Third, the AFM images of the fibrils reflect the fibril configuration in solution. When fibrils are deposited on the mica surface, their fully hydrated state 3D shape is "projected" to 2D space. So the bending modulus calculated from the persistence length applies to the fibrils in solution. The "projection" would also shorten the persistence length hence reduce the bending modulus. Fourth, when the fibril-containing solution is deposited on the mica surface, the interaction force between the substrate and the fibrils and the dewetting effect can distort the fibril profile, resulting in shorter persistence length and hence smaller apparent bending modulus.

4.5 Conclusions

Three different growth stages in the type I collagen fibrillogenesis process are confirmed. The fibril growth is mostly limited to the N-termini which serve as a growth center. The monomers first form C-N unipolar fibrils. A transition step occurs on the C-termini of the C-N unipolar structures after the fibrils reach a larger size, turning C-N unipolar fibrils to N-N bipolar fibrils. The mature fibrils assume N-N bipolar structure based on the AFM images.

The calculated fibril Young's moduli decrease when their diameters increase and, for the same fibril, the Young's moduli increase when the maximum loads increase. These two trends are explained by substrate effects: smaller fibrils and larger maximum loads inevitably add more contribution from the the very stiff substrate, distorting the real Young's moduli. Under experimental conditions optimized to minimize both substrate contributions and adhesion interactions, the fibril Young's modulus is calculated to be 0.27 ± 0.07 GPa.

The fibril bending moduli decrease with increasing fibril diameter. The fibril is formed primarily by hydrophobic interactions between collagen monomers. This interaction is much weaker than the association among the three entangled peptide chains in a monomer. When more collagen monomers attach to the fibril to form a larger fibril, more weaker hydrophobic interactions are added to the fibril. Hence the bending modulus decreases.

The bending moduli are in general very low. This is attributed to the fibril's anisotropic structure, defects, the hydration state and substrate effect.

Bibliography

[1] M. Dong, S. Xu, M. H. Büger, H. Birkedal, and F. Besenbacher. Temporal assembly of collagen type II studied by atomic force microscopy. *Advanced Engineering Materials*, 9:1129–1133, 2007.

[2] K. Beck, V. C. Chan, N. Shenoy, A. Kirkpatrick, J. A. M. Ramshaw, and B. Brodsky. Destabilization of osteogenesis imperfecta collagen-like model peptides correlates with the identity of the residue replacing glycine. *Proceedings of the National Academy of Sciences of the United States of America*, 97:4273–4278, 2000.

[3] J. Caffey. Infantile cortical hyperostosis; a review of the clinical and radiographic features. *Proceedings of the Royal Society of Medicine*, 50:347–354, 1957.

[4] A. Augello, R. Tasso, S. M. Negrin, R. Cancedda, and G. Pennesi. Cell therapy using allogeneic bone marrow mesenchymal stem cells prevents tissue damage in collagen-induced arthritis. *Arthritis & Rheumatism*, 56:1175–1186, 2007.

[5] M. D. Shoulders and R. T. Raines. Collagen structure and stability. *Annual Review of Biochemistry*, 78:929–958, 2009.

[6] P. Carmeliet. Angiogenesis in health and disease. *Nature medicine*, 9:653–660, 2003.

[7] E. A. G. Chernoff and D. A. Chernoff. Atomic force microscope images of collagen fibers. *Journal of Vacuum Science & Technology A: Vacuum, Surfaces, and Films*, 10:596–599, 1992.

[8] E. Bender, F. H. Silver, K. Hayashi, and R. L. Trelstad. Type I collagen segment long spacing banding patterns. Evidence that the alpha 2 chain is in the reference or a position. *Journal of Biological Chemistry*, 257:9653–9657, 1982.

[9] D. A. Wah and J. T. Czernuszka. Collagen-hydroxyapatite composites for hard tissue repair. *European Cells and Materials*, 11:43–56, 2006.

[10] J. E. Scott. Proteoglycan-fibrillar collagen interactions. *Biochemical Journal*, 252:313–323, 1988.

[11] J. Y. Rho, R. B. Ashman, and C. H. Turner. Young's modulus of trabecular and cortical bone material: Ultrasonic and microtensile measurements. *Journal of Biomechanics*, 26:111–119, 1993.

[12] K. Hasegawa, C. H. Turner, and D. B. Burr. Contribution of collagen and mineral to the elastic anisotropy of bone. *Calcified Tissue International*, 55:381–386, 1994.

[13] D. T. Reilly and A. H. Burstein. The elastic and ultimate properties of compact bone tissue. *Journal of Biomechanics*, 8:393–405, 1975.

[14] B. R. William, A. R. Gelman, D. C. Poppke, and K. A. Piez. Collagen fibril formation. *The Journal of Biological Chemistry*, 253:6578–6585, 1978.

[15] K. G. Vogel and J. A. Trotter. The effect of proteoglycans on the morphology of collagen fibrils formed *in vitro*. *Collagen and Related Research*, 7:105 – 114, 1987.

[16] D. E. Birk and R. L. Trelstad. Extracellular compartments in tendon morphogenesis: collagen fibril, bundle, and macroaggregate formation. *The Journal of cell biology*, 103:231–240, 1986.

[17] G. D. Pins, D. L. Christiansen, R. Patel, and F. H. Silver. Self-assembly of collagen fibers. Influence of fibrillar alignment and decorin on mechanical properties. *Biophysical Journal*, 73:2164–2172, 1997.

[18] D. L. Butler, M. D. Kay, and D. C. Stouffer. Comparison of material properties in fascicle-bone units from human patellar tendon and knee ligaments. *Journal of Biomechanics*, 19:425–432, 1986.

[19] N. Sasaki and S. Odajima. Stress-strain curve and Young's modulus of a collagen molecule as determined by the X-ray diffraction technique. *Journal of Biomechanics*, 29:655–658, 1996.

[20] M. P. E. Wenger, L. Bozec, M. A. Horton, and P. Mesquida. Mechanical properties of collagen fibrils. *Biophysical Journal*, 93:1255–1263, 2007.

[21] A. J. Heim, W. G. Matthews, and T. J. Koob. Determination of the elastic modulus of native collagen fibrils via radial indentation. *Applied Physics Letters*, 89:181902, 2006.

[22] J. S. Graham, A. N. Vomund, C. L. Phillips, and M. Grandbois. Structural changes in human type I collagen fibrils investigated by force spectroscopy. *Experimental Cell Research*, 299:335–342, 2004.

[23] L. Yang, K. O. van der Werf, C. F. C. Fitié, M. L. Bennink, P. J. Dijkstra, and J. Feijen. Mechanical properties of native and cross-linked type I collagen fibrils. *Biophysical Journal*, 94:2204–2211, 2008.

[24] A. J. Heim, T. J. Koob, and W. G. Matthews. Low strain nanomechanics of collagen fibrils. *Biomacromolecules*, 8:3298–3301, 2007.

[25] L. Yang, K. O. van der Werf, B. F. J. M. Koopman, V. Subramaniam, M. L. Bennink, P. J. Dijkstra, and J. Feijen. Micromechanical bending of single collagen fibrils using atomic force microscopy. *Journal of Biomedical Materials Research Part A*, 82:160–168, 2007.

[26] C. H. Wiggins, D. Riveline, A. Ott, and R. E. Goldstein. Trapping and wiggling: elastohydrodynamics of driven microfilaments. *Biophysical journal*, 74:1043–1060, 1998.

[27] F. Gittes, B. Mickey, J. Nettleton, and J. Howard. Flexural rigidity of microtubules and actin filaments measured from thermal fluctuations in shape. *The Journal of Cell Biology*, 120:923–934, 1993.

[28] G. Binnig, C. F. Quate, and C. Gerber. Atomic force microscope. *Physical Review Letters*, 56:930–933, Mar 1986.

[29] A. Dalgarno and A. E. Kingston. Van der Waals forces. *Proceedings of the Physical Society*, 73:455–464, 1959.

[30] H. J. Butt. Measuring electrostatic, van der Waals, and hydration forces in electrolyte solutions with an atomic force microscope. *Biophysical Journal*, 60:1438–1444, 1991.

[31] S. K. Lamoreaux. Demonstration of the Casimir force in the 0.6 to 6 μm range. *Physical Review Letters*, 78:5–8, 1997.

[32] I. Manoubi, F. Najar, S. Choura, and A. H. Nayfeh. Nonlinear dynamical analysis of an AFM tapping mode microcantilever beam. In *MATEC Web of Conferences*, volume 1, page 04002. EDP Sciences, 2012.

[33] A. Gannepali, D. G. Yablon, A. H. Tsou, and R. Proksch. Mapping nanoscale elasticity and dissipation using dual frequency contact resonance AFM. *Nanotechnology*, 22:355705, 2011.

[34] J. P. Killgore and D. C. Hurley. Low-force AFM nanomechanics with higher-eigenmode contact resonance spectroscopy. *Nanotechnology*, 23:055702, 2012.

[35] K. L. Johnson. *Contact Mechanics*. Cambridge University Press, Cambridge, 1985.

[36] I. N. Sneddon. The relation between load and penetration in the axisymmetric boussinesq problem for a punch of arbitrary profile. *International Journal of Engineering Science*, 3:47–57, 1965.

[37] M. F. Doerner and W. D. Nix. A method for interpreting the data from depth-sensing indentation instruments. *Journal of Materials Research*, 1:601–609, 1986.

[38] J. S. Field and M. V. Swain. A simple predictive model for spherical indentation. *Journal of Materials Research*, 8:297–306, 1993.

[39] W. C. Oliver and G. M. Pharr. An improved technique for determining hardness and elastic modulus using load and displacement sensing indentation experiments. *Journal of Materials Research*, 7:1564–1583, 1992.

[40] H. H. Lovelady, S. Shashidhara, and W. G. Matthews. Solvent specific persistence length of molecular type I collagen. *Biopolymers*, 101:329–335, 2014.

[41] C. K. P. Loong, H.-X. Zhou, and P. B. Chase. Persistence length of human cardiac α-tropomyosin measured by single molecule direct probe microscopy. *PloS one*, 7:e39676, 2012.

[42] S. Kunii, K. Morimoto, K. Nagai, T. Saito, K. Sato, and B. Tonomura. Actinidain-hydrolyzed type I collagen reveals a crucial amino acid sequence in fibril formation. *Journal of Biological Chemistry*, 285:17465–17470, 2010.

[43] J. L. Hutter. Comment on tilt of atomic force microscope cantilevers: effect on spring constant and adhesion measurements. *Langmuir*, 21:2630–2632, 2005.

[44] Y. Roiter and S. Minko. 2D Single Molecules. Freeware, available for download at http://people.clarkson.edu/sminko, 2006.

[45] K. E. Kadler, D. F. Holmes, J. A. Trotter, and J. A. Chapman. Collagen fibril formation. *Biochemical Journal*, 316:1–11, 1996.

[46] A. T. Winzer, C. Kraft, S. Bhushan, V. Stepanenko, and I. Tessmer. Correcting for AFM tip induced topography convolutions in protein-DNA samples. *Ultramicroscopy*, 121:8–15, 2012.

[47] J. P. Orgel, T. J. Wess, and A. Miller. The *in situ* conformation and axial location of the intermolecular cross-linked non-helical telopeptides of type I collagen. *Structure*, 8:137–142, 2000.

[48] D. F. Holmes, J. A. Chapman, D. J. Prockop, and K. E. Kadler. Growing tips of type I collagen fibrils formed *in vitro* are near-paraboloidal in shape, implying a reciprocal relationship between accretion and diameter. *Proceedings of the National Academy of Sciences of the United States of America*, 89:9855–9859, 1992.

[49] A. Gautieri, S. Vesentini, A. Redaelli, and M. J. Buehler. Hierarchical structure and nanomechanics of collagen microfibrils from the atomistic scale up. *Nano Letters*, 11:757–766, 2011.

[50] D. E. Birk, E. I. Zycband, D. A. Winkelmann, and R. L. Trelstad. Collagen fibrillogenesis *in situ*. *Annals of the New York Academy of Sciences*, 580:176–194, 1990.

[51] K. E. Kadler, Y. Hojima, and D. J. Prockop. Assembly of collagen fibrils *de novo* by cleavage of the type I pC-collagen with procollagen C-proteinase. assay of critical concentration demonstrates that collagen self-assembly is a classical example of an entropy-driven process. *The Journal of Biological Chemistry*, 262:15696–15701, 1987.

[52] M. A. Hossein, M. Shahverdi, and M. Roohnia. The effect of wood knot as a defect on modulus of elasticity (moe) and damping correlation. *Notulae Scientia Biologicae*, 3:145–149, 2011.

Chapter 5

Fibrillogenesis and Nanomechanics of Type II Collagen Fibrils

Type II collagen fibrils prepared by the “cold start” method follow a sequential process similar to that observed for type I collagen, with mature fibrils reaching up to 12 nm in diameter. However, the type II collagen fibrils prepared are significantly shorter compared with type I collagen. At the early growth stage, the fibrils have unipolar structure. Then some turn to bipolar while others remain unipolar. As with the type I collagen fibrils, the bending modulus (deduced from the persistence length) is significantly smaller than the indentation Young’s modulus (calculated with the Oliver-Pharr method). A large number of type II collagen monomers are also observed in the sample without incubation, allowing for a calculation of monomer bending moduli in addition to the fibril properties.

5.1 Introduction

Collagen is a protein family of more than 26 members.[1] Most of them are fibrous protein, although some, such as type VI collagen, may carry globular domains.[2] Unlike most globular proteins, the most important role collagen plays is a structural function. Type II collagen plays an important role in cartilage and bone joints: it accounts for 50%-90% of all the proteins in these tissues.[3] Although other types of collagen may not be so abundant, they also play a very important role in animal bodies. Type III collagen is the main ingredient of granulation tissue and reticular fiber,[4, 5] and type IV collagen presents in basement membranes.[5] Type V collagen associates with type I collagen to enhance fibril growth in fibrillogenesis.[6] Type VI collagen is also a major constituent of cornea along with type I collagen.[7] All types of collagen have their own unique functions.

While type II collagen has different functions and presents in different tissues than with type I collagen (although they sometimes may present in the same tissue), their compositions are very similar. Type II collagen monomers are rope-like macromolecules. They are about 300 nm long and 1.5 nm in diameter. Each monomer contains three collagen alpha-2(I) peptide chains. The peptide chains have a unique amino acid sequence which consists of repeating units Gly-X-Y. Gly denotes a glycine residue and X and Y denote other amino acids. In many cases, X and Y are proline or hydroxyproline. This special sequence ensures the peptides chains will fold into left handed α helices.

Three α helices subsequently twist together to form a right handed coil: the collagen monomer. It takes several steps to generate collagen monomers.[8] In the endoplasmic reticulum, collagen peptides are synthesized, modified and folded to form triple helical procollagen monomers. Then the procollagen monomers are transferred to the Golgi complex where they are decorated with oligosaccharides and subsequently packed in secretory vesicles. The packed procollagen is secreted to extracellular space. Collagen peptidases remove some non-helical amino acid residues on both ends of the procollagen to produce tropocollagen. With the aid of other biomolecules, tropocollagen monomers pack laterally and longitudinally to form collagen fibrils.

As the second most abundant collagen, the type II collagen in cartilage helps to bear stress and reduce friction. Damage or mutation of type II collagen can cause serious health problems like joint dysfunction and arthritis,[9] with which the patient will suffer severe pain and difficulty in movement. Type II collagen consists of more than half the dry weight of the articular cartilage.[10] The articular cartilage is truly a biological engineering marvel. With relatively small contact area, the cartilage contact surfaces in a bone joint need to sustain body weight, absorb sudden shock force and resist friction.[11] To achieve this, type II collagen orients tangentially in the cartilage surface layer to cope with the high shear stress and friction. It lays randomly in the middle layer to deal with moderate shear stress and compressive stress. In the deep layer, it aligns perpendicularly to handle high compressive stress. In this regard, it is curious to know how the collagen orientation affects its performance under different types of stress.

Young's modulus is a measurement of material resistance against applied stress.[12] This mechanical property has long been the focus of many studies on collagen and collagen containing materials. Wenger *et al.* performed nanoindentation tests on rat tail tendon collagen fibrils and found that the Young's modulus is between 5 GPa and 11.5 GPa.[13] Yadavalli *et al.* found that collagen fibrils assembled from collagen monomers have a much smaller Young's modulus of around 1 GPa. They attribute this disparity to the assumption that the fiber is not fully formed.[14] Yang *et al.* performed bending tests on single collagen fibrils and deduced the Young's modulus to be about 5.4 GPa.[15] Minary-Jolandan and Yu applied dynamic nanoindentation on the gap and overlap regions of collagen fibril and revealed nanomechanical heterogeneity in these regions.[16] Chung *et al.* studied the thin film formed from collagen fibrils and concluded that Young's modulus is dependent on the hydration states.[17] So the results are greatly influenced by the collagen sources, collagen sample forms, test methods, fibril heterogeneity, hydration states and other factors.

However these studies are primarily devoted to type I collagen. Since type II collagen is the second most abundant collagen and forms some crucial tissues, it is worth taking a closer look at it. In this chapter, the comprehensive study on type II collagen properties, especially the mechanical properties, is unprecedented.

5.2 Materials and Methods

5.2.1 Sample Preparation

Recombinant type II collagen from HT1080 cells[18] was kindly supplied by Dr. Nancy Forde of Simon Fraser University. Samples were prepared as described in Section 4.3, creating "snapshots" of the fibrillogenesis process for analysis by AFM.

5.2.2 Young's Modulus and Bending Modulus

The fibrils are formed by individual collagen monomers staggering themselves laterally and longitudinally to each other. This makes the fibrils mechanically anisotropic: the mechanical property measured transverse to a fibril would be different from that measured along the fibril. Nanoindentation tests carried out on the fibrils measures compression stiffness transverse to the fibrils, with Young's moduli (E_s) calculated according to the method in Chapter 4 (Equation 4.8). We again use 0.3 for Poisson's ratio and 50 nm for the indenter radius. The bending modulus is extracted from the persistence length (extracted with the software 2D Single Molecules[19]), according to chapter 4.

5.3 Results and Discussion

5.3.1 Fibrillogenesis of Type II Collagen

Type II collagen fibrillogenesis is investigated by comparing AFM images of fibril samples with different amounts of incubation time (Figure 5.1).

Before incubation (Figure 5.1A), most of the filaments in the AFM image are around 1.5-2.0 nm high, 350 nm long and 50 nm wide. The height is close to a single collagen monomer diameter and the length is in the range of a single collagen monomer. However, the filament width does not match any dimension of a single collagen monomer.

One drawback of the AFM is that an AFM image is the convolution of the tip geometry and sample morphology, as depicted schematically in Figure 5.2. The three circles in Figure 5.2 represent the AFM tip (the apex of the AFM tip used in the experiment is spherical) at different positions in relation to the sample (black half disk). At position A, the tip comes into contact with the sample and it begins to rise. At position B, the tip reaches the highest point of the sample. At position C, the tip comes out of contact with the sample. The trajectory of the tip (dotted line) which is used to generate AFM image does not directly represent the contour of the sample (half disk).

Only at the highest point on the sample (position B in Figure 5.2) does the recorded value match the real dimension. Therefore, the filament height in the AFM image is a more reliable parameter and it can represent the diameter of the real fibrils. Both the filament width and length are enlarged by around 50 nm because of

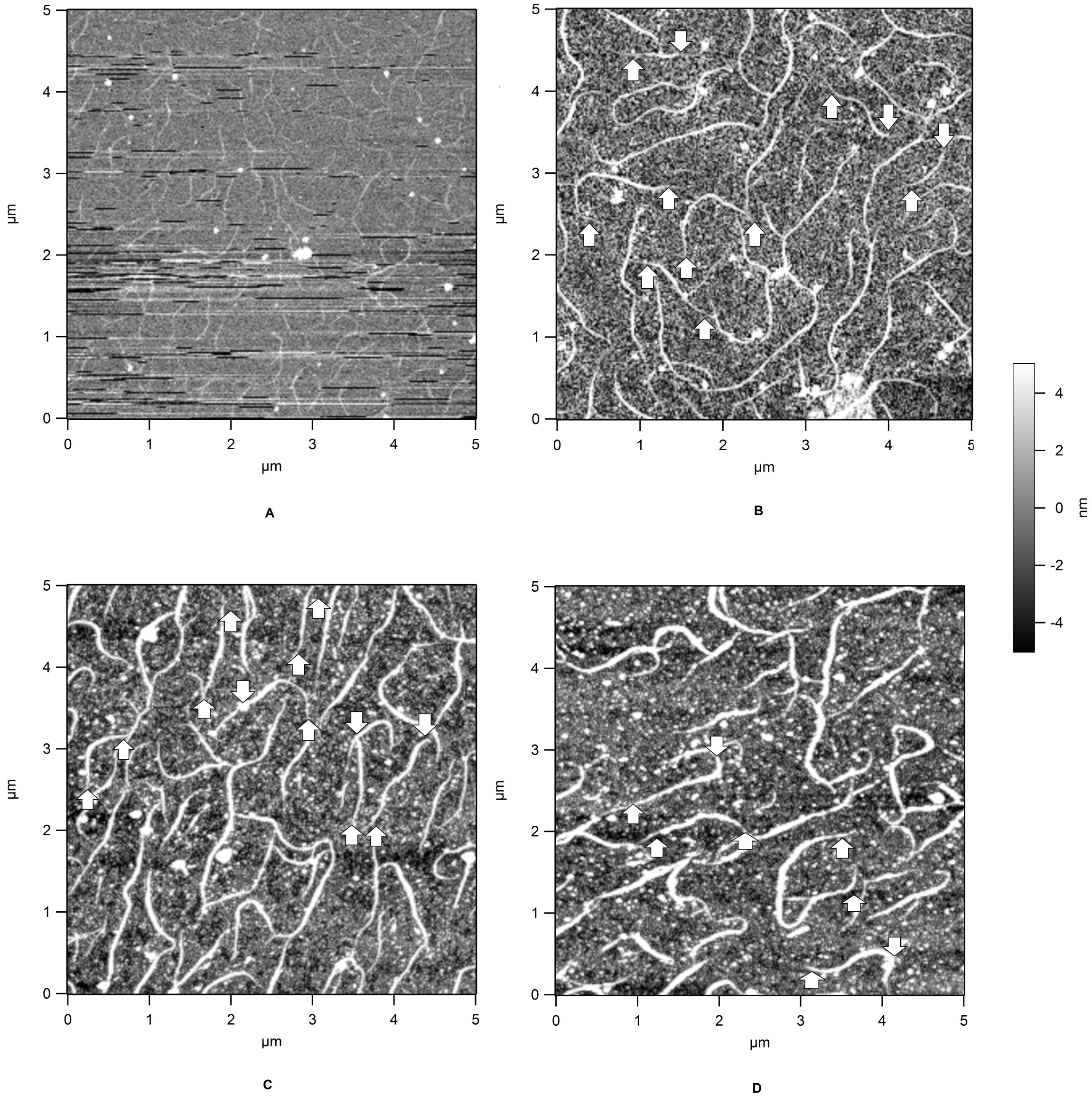

Figure 5.1: Fibrillogenesis process of type II collagen (A) before incubation, and after (B) 10 minutes, (C) 20 minutes, and (D) 30 minutes of incubation. The upward pointing arrows show tapered ends and downward pointing arrows show blunt ends.

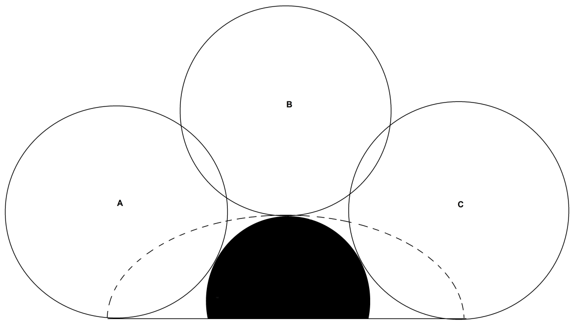

Figure 5.2: The AFM image is a convolution of the tip geometry and sample morphology.

the convolution, which is consistent with each other. Considering that the filament height and the deconvoluted length match the dimension of a single collagen monomer and there is no other material with similar dimension, we can conclude that these filaments are single collagen monomers.

After 10 minutes, the filaments grow to 1-3 μm long and around 8 nm high (Figure 5.1 B). Some shorter filaments (less than 1.5 μm long) have one tapered end and one slightly blunt end. As discussed in Chapter 4, the collagen monomer has two different ends: the N-terminus with a free amine group and the C-terminus with a free carboxyl group. When monomers associate to form fibrils, the growth always starts at the N-terminus.[20] The N-terminus serves as the growth center and fibrils extend their length in the N-terminal direction. Later-added monomers will point their N-termini to the same direction of the growth center N-termini. The fibrils formed this way will have their monomer N-termini pointing in one direction and C-termini pointing in the other direction. This fibril structure is called the C-N unipolar structure. This N-terminus exclusive growth pattern causes the C-terminus become blunt and the N-terminus become tapered.

For some longer fibrils (more than 2 μm), both of their ends become tapered. This is the result of growth on the fibril C-terminus.[21] After the fibril reaches a larger diameter, there are more groups that can associate with monomers on the C-terminus. The association force will become strong enough to support monomers to attach to the fibril C-terminus. The C-terminus become another growth center. At this growth center, the later-added monomers will align their molecular direction opposite to the direction of the fibril which they attach to. This new growth center acts as a transition point where the fibril C-terminus changes to a new fibril N-terminus. This results in the C-N unipolar fibril structure turning into N-N bipolar fibril structure.

After 20 minutes, the fibril height increases to around 9 nm (Figure 5.1 C). However, there is no evident change in their length. Both C-N unipolar fibrils and N-N bipolar fibrils can be seen.

After 30 minutes, the fibril height increases to around 10 nm and their length seems unchanged (Figure 5.1 D). No significant change can be observed under further incubation. Therefore, the fibrils become mature after 30 minutes of incubation. As before, both C-N unipolar fibrils and N-N bipolar fibrils are observed.

Compared with type I collagen fibrils, type II collagen fibrils are shorter and smaller. It is reported that type II collagen fibrils are harder to form than type I collagen fibrils.[22] The ultimate cause of this difference must relate to their slightly different amino acid sequences. According to Equation 4.12, persistence lengths will be shorter for fibrils with smaller radii, when other parameters are the same. Therefore, thinner fibrils have better flexibility. This would be preferred in cartilage, where flexibility is more important than stiffness.

The relatively short length and smaller diameter of the type II collagen fibrils did not change upon prolonged incubation time. No substantial difference is observed between the fibrils incubated for 30 minutes and the fibrils incubated for 24 hours.

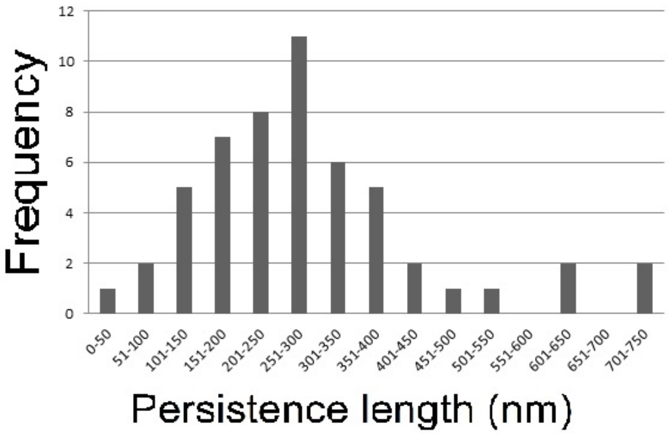

Figure 5.3: Histogram of persistence length distribution

5.3.2 Monomer and Fibril Persistence Lengths and Bending Moduli

The large number of monomers in Figure 5.1A provide the opportunity to investigate collagen monomer persistence length and subsequently derive the bending modulus. In total, the persistence lengths of 53 identifiable monomers were calculated. The monomer persistence length frequency was obtained by counting the number of monomers in a certain range of persistence length and is plotted in Figure 5.3. The histogram plot approximately resembles a normal distribution. Given enough monomer counts, the monomer persistence length distribution should follow a normal distribution because the variation of the persistence length is the result of random collisions between solvent molecules and the monomers. The average persistence length is 286 ± 52 nm.

The persistence length extracted from images of filaments with diameters of around 1.5 nm (monomer), 7 nm, 9 nm and 11 nm are plotted against the filament diameters in Figure 5.4. The bending moduli are calculated according to Equation 4.12 and plotted against diameter in Figure 5.5. Similar to the type I collagen filaments,

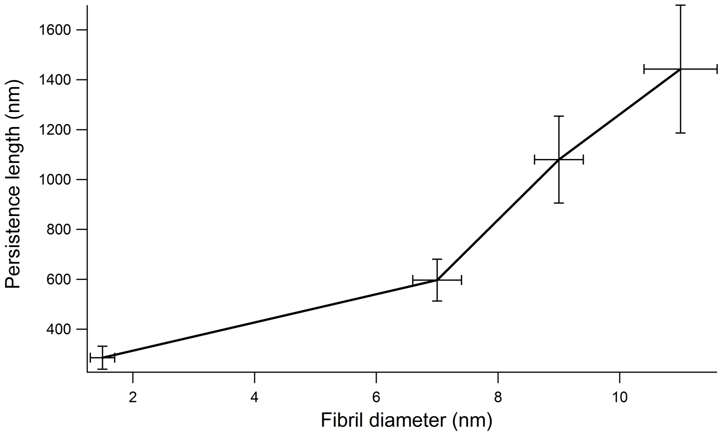

Figure 5.4: Persistence length vs. fibril diameter.

the type II collagen filament persistence increases against diameter while bending modulus decreases against diameter.

Type-II collagen monomers have a bending modulus of 4.7 GPa. As the monomers form fibrils, the bending modulus decreases significantly: the fibrils with diameter of 11 nm have a bending modulus of around 8 MPa ($p < 0.0001$ when compared to the monomers). This difference is related to the structure of the monomers and fibrils. A monomer is constructed from three strands of peptide chains interlocked by highly ordered hydrogen bonds: for each Gly-X-Y triplet, there is an interstrand $N - H_{(Gly)}...O = C_{(X/Y)}$ hydrogen bond.[23] In contrast, a fibril is formed by hydrophobic interactions, with the force between monomers in a fibril being far smaller than the interstrand hydrogen bonding within a monomer. This results in the significant decrease of bending modulus when fibril diameter increases.

The fibril Young's modulus calculated from nanoindentation tests according to Equation 4.8 is 0.5±0.1 GPa which is slight higher ($p = 0.005$) than the type I collagen Young's modulus (see Chapter 4). The type II collagen fibrils have higher Young's modulus than the type I fibrils. This may due to the slight structure difference between type I and type II collagen which leads to slightly different monomer interactions

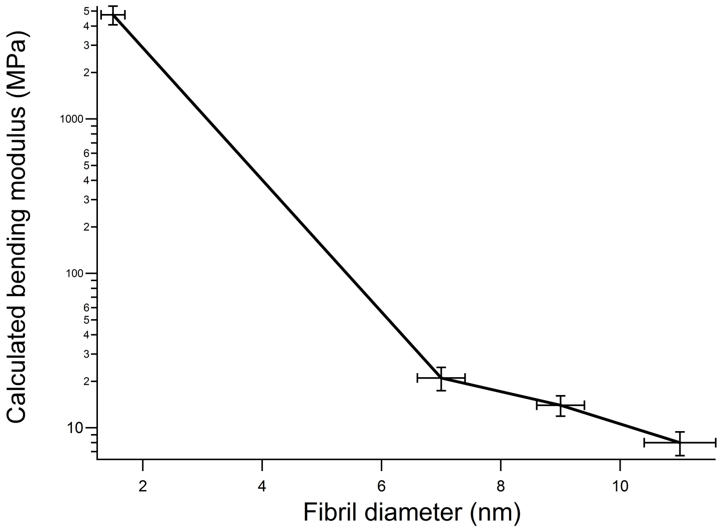

Figure 5.5: Bending modulus vs. fibril diameter.

when fibrils are formed. Comparison of the bending modulus and Young's modulus to literature values can not be proceeded due to lack of literature values. This is the first of its kind to carry out research on this subject.

As in the case of the type I collagen fibrils, the bending modulus of type II collagen fibrils is very low after fibrils reach larger diameter. This arises from structural reason as well as test method. First, the fibrils are highly anisotropic because of the quarterly staggering pattern of collagen monomers. Second, defects (e.g. misalignment of monomers) would significantly increase stress at some particular location and reduce the bending modulus.[24] Third, the persistence length reflects the structure of fully hydrated collagen fibrils in solution, so the derived bending modulus from persistence length reflects the mechanics of a fibril in a fully hydrated state. Fourth, when depositing collagen fibrils on a mica surface, the collagen fibrils are under forces like substrate attraction forces and dewetting effects which would distort the natural curvature of the fibrils.

5.4 Conclusions

The fibrillogenesis process of type II collagen proceeds in three stages. C-N unipolar fibrils are formed at the beginning. In the following step, some of the C-N unipolar fibrils are converted to N-N bipolar fibrils while other C-N unipolar fibrils keep unchanged. This is different from the type I collagen fibrillogenesis in which all C-N unipolar fibrils are converted to N-N bipolar fibrils. The mature type II collagen fibrils are smaller and significantly shorter than mature type I collagen fibrils. These discrepancies in fibrillogenesis and dimension between type I and type II collagen are attributed to their difference in amino acid sequence.

Type II collagen monomer persistence lengths approximately follow a normal distribution based on 53 monomers, with an average persistence length of 286 ± 52 nm. The bending modulus is 4.7 ± 0.7 GPa. The fibril persistence lengths increases with respect to diameter while their bending moduli decrease with respect to diameter due to the stronger intramonomer (and weaker intermonomer) interactions.

The fibril Young's modulus measured by nanoindentation is 0.5 ± 0.1 GPa, slightly larger than the type I collagen fibrils.

The low bending modulus is the result of fibril anisotropy, defects, hydration state and substrate effect.

Bibliography

[1] M. Dong, S. Xu, M. H. Büger, H. Birkedal, and F. Besenbacher. Temporal assembly of collagen type II studied by atomic force microscopy. *Advanced Engineering Materials*, 9:1129–1133, 2007.

[2] H.-J. Kuo, C. L. Maslen, D. R. Keene, and R. W. Glanville. Type VI collagen anchors endothelial basement membranes by interacting with type IV collagen. *Journal of Biological Chemistry*, 272:26522–26529, 1997.

[3] C. Lee, S. Grad, S. Wimmer, and M. Alini. The influence of mechanical stimuli on articular cartilage tissue engineering. *Topics in tissue engineering*, 2:1–32, 2005.

[4] C. S. Chamberlain, E. M. Crowley, H. Kobayashi, K. W. Eliceiri, and R. Vanderby. Quantification of collagen organization and extracellular matrix factors within the healing ligament. *Microscopy and Microanalysis*, 17:779–787, 8 2011.

[5] H. Zeng, C. MacAulay, B. Palcic, and D. I. McLean. Spectroscopic and microscopic characteristics of human skin autofluorescence emission. *Photochemistry and photobiology*, 61:63–645, 1995.

[6] D. E. Birk, J. M. Fitch, J. P. Babiarz, K. J. Doane, and T. F. Linsenmayer. Collagen fibrillogenesis *in vitro*: interaction of types I and V collagen regulates fibril diameter. *Journal of Cell Science*, 95:649–657, 1990.

[7] D. R. Zimmermann, B. Trüeb, K. H. Winterhalter, Rudolf Witmer, and René W. Fischer. Type VI collagen is a major component of the human cornea. *FEBS Letters*, 197:55–58, 1986.

[8] H. Lodish, A. Berk, S. L. Zipursky, P. Matsudaira, D. Baltimore, and J. Darnell. *Molecular Cell Biology.* New York: W. H. Freeman, 2000.

[9] C.-H. Hsieh, Y.-H. Lin, S. Lin, J.-J. Tsai-Wu, C.H. Herbert Wu, and C.-C. Jiang. Surface ultrastructure and mechanical property of human chondrocyte revealed by atomic force microscopy. *Osteoarthritis and Cartilage*, 16:480–488, 2008.

[10] K. A. Athanasiou, E. M. Darling, and J. C. Hu. Articular cartilage tissue engineering. *Synthesis Lectures on Tissue Engineering*, 1:1–182, 2009.

[11] J.M. Clark. The organisation of collagen fibrils in the superficial zones of articular cartilage. *Journal of Anatomy*, 171:117–130, 1990.

[12] K. L. Johnson. *Contact Mechanics.* Cambridge University Press, Cambridge, 1985.

[13] M. P. E. Wenger, L. Bozec, M. A. Horton, and P. Mesquida. Mechanical properties of collagen fibrils. *Biophysical Journal*, 93:1255–1263, 2007.

[14] V. K. Yadavalli, D. V. Svintradze, and R. M. Pidaparti. Nanoscale measurements of the assembly of collagen to fibrils. *International Journal of Biological Macromolecules*, 46:458–464, 2010.

[15] L. Yang, K. O. van der Werf, B. F. J. M. Koopman, V. Subramaniam, M. L. Bennink, P. J. Dijkstra, and J. Feijen. Micromechanical bending of single collagen fibrils using atomic force microscopy. *Journal of Biomedical Materials Research Part A*, 82:160–168, 2007.

[16] M. Minary-Jolandan and M.-F. Yu. Nanomechanical heterogeneity in the gap and overlap regions of type I collagen fibrils with implications for bone heterogeneity. *Biomacromolecules*, 10:2565–2570, 2009.

[17] K. Chung, K. Bhadriraju, T. A. Spurlin, R. F. Cook, and A. L. Plant. Nanomechanical properties of thin films of type I collagen fibrils. *Langmuir*, 26:3629–3636, 2010.

[18] A. Fertala, A. L. Sieron, A. Ganguly, S. W. Li, L. Ala-Kokko, K. R. Anumula, and D. J. Prockop. Synthesis of recombinant human procollagen II in a stably transfected tumour cell line (HT1080). *Biophysical Journal*, 298:31–37, 1994.

[19] Y. Roiter and S. Minko. 2D Single Molecules. Freeware, available for download at http://people.clarkson.edu/sminko, 2006.

[20] K. E. Kadler, D. F. Holmes, J. A. Trotter, and J. A. Chapman. Collagen fibril formation. *Biochemical Journal*, 316:1–11, 1996.

[21] D. F. Holmes, J. A. Chapman, D. J. Prockop, and K. E. Kadler. Growing tips of type I collagen fibrils formed *in vitro* are near-paraboloidal in shape, implying a reciprocal relationship between accretion and diameter. *Proceedings of the National Academy of Sciences of the United States of America*, 89:9855–9859, 1992.

[22] D. E. Birk and F. H. Silver. Collagen fibrillogenesis *in vitro*: comparison of types I, II, and III. *Archives of biochemistry and biophysics*, 235:178–185, 1984.

[23] M. D. Shoulders and R. T. Raines. Collagen structure and stability. *Annual Review of Biochemistry*, 78:929–958, 2009.

[24] M. A. Hossein, M. Shahverdi, and M. Roohnia. The effect of wood knot as a defect on modulus of elasticity (moe) and damping correlation. *Notulae Scientia Biologicae*, 3:145–149, 2011.

Chapter 6

Conclusions

6.1 Summary

Collagen is the most abundant protein in mammal bodies, with type I and type II being the most prominent.[1] They play important roles in bones, joints and cartilage, endowing these connective tissues with flexibility, tensility and compressibility. My doctoral research has led to a greater understanding of collagen aggregate structure and properties while also developing new approaches to measure and analyze mechanical properties of soft materials.

Under proper conditions, collagen can form fibrils (fibrillogenosis), ranging from several hundred nanometers to micrometers long.[2–4] With the aid of atomic force microscopy (AFM), I demonstrated three distinctive stages present in this process: unipolar structure, bipolar structure and mature fibrils. My observations also found that fibrils in different growth stages differ in structure and dimension. Compared with type I collagen fibrils, type II collagen fibrils are significantly shorter. This is consistent with findings in biological systems and may ultimately be attributed to their difference in amino acid sequence. This work paves the way for further study on type I and type II collagen fibrillogenosis process.

The mechanical properties are of particular interest to this study since it is the most important function of connective tissues. To characterize the mechanical response of fibrils with nanoscale diameter, I performed nanoindentation on individual fibrils with AFM to obtain force curves. The force curves were analyzed with the Oliver-Pharr method[5] to yield Young's moduli. I found that type I and type II collagen fibrils have similar Young's moduli and bending moduli. Their Young's moduli are considerably larger than their bending moduli due to fibril anisotropy. These results revealed important information of type I and type II collagen fibril mechanical properties.

I developed a novel minimum nanoindentation method to minimize substrate effects and characterize the superficial layer of samples. Minimum loading force is achieved by indenting samples with only the adhesion force between the indenter and samples. This results in minimum indentation depth of less than 10 nm and negligible sample destruction. This method is highly reproducible and accurate. This research enables true surface analysis on hydrophobic surfaces.

I also developed another minimum indentation model to account for hydrophilic surfaces under capillary effects. The minimum loading force is the capillary force between the indenter and the hydrophilic surface. This model was then applied to study the nanomechanics of segment-long-spacing (SLS) crystallites, an aggregate of type I collagen which has not been characterized mechanically before.

6.2 Future Directions

6.2.1 Method Development

The minimum nanoindentation methods have wide application. The minimum loading force ensures minimal destruction and substrate effects on samples when characterization is carried out. This is especially important for biological samples like cells which are small and fragile. For example, minimum nanoindentation methods can be applied to study the response of cancer cells to drugs. Cancer cells have different mechanical properties compared with normal cells.[6] By monitoring the cancer cell mechanical properties over the course of treatment, the efficiency of the drug can be evaluated. In this case, the minimum nanoindentation methods will prevent the cells from damage and the cell will not be affected by repeating nanoindentation tests.

The minimum indentation methods can be further improved. First, the nanoindentation methods can be extended to the intermediate regions between the two extreme conditions, hydrophobic surfaces and hydrophilic surfaces, which are discussed in the thesis. To achieve this, capillary and surface adhesion forces should be accounted for at the same time. Second, other indenter-sample contact models can also be incorporated in the minimum nanoindentation methods beside the JKR model and the DMT model.[7, 8] Third, the minimum loading force can also be adjusted to accommodate the desired application. This can be accomplished by attaching different-sized spheres to the end of the cantilever or modify the indenter surface with a layer of materials with different Hamaker constant.[9, 10] Last but not least, similar minimum indentation methods can also be developed and verified for application in solution.[11]

The methods to obtain mechanical properties of anisotropic material described in Chapters 4 and 5 can also be applied to many other materials. Different hydration states will result in different Young's modulus values. It is interesting to compare the moduli under the different hydration states. By performing nanoindentation tests in solution, this can be achieved.

6.2.2 Biomaterials Studies

The type I SLS crystallites exhibit interesting shape and have their own biological importance. It is worth checking the driving force for the end-to-end association between different SLS. The overlap length of the adjacent SLS is also very reproducible, which could suggest a unique and specific banding pattern such as that found in native and FLS collagen fibrils.[12] Now that the methods have been developed and tested, more detailed nanomechanical mapping could identify structural variations within the SLS crystallite which could promote inter-crystallite interactions.

Type II collagen has similar structure to type I collagen. An inevitable question is, would type II collagen form similar SLS crystallites? If so, what are the differences between type I and type II SLS? Are there similar truncations in aggregation as I have observed for fibril formation? Nanomechanical mapping could also reveal structural differences between the two, which could reflect different requirements and hence roles in biological systems.

Bibliography

[1] R. Mayne and R. E. Burgeson. *Structure and Function of Collagen Types.* Elsevier, Orlando, Florida, 1987.

[2] D. E. Birk, J. M. Fitch, J. P. Babiarz, K. J. Doane, and T. F. Linsenmayer. Collagen fibrillogenesis *in vitro*: interaction of types I and V collagen regulates fibril diameter. *Journal of Cell Science*, 95:649–657, 1990.

[3] B. R. William, A. R. Gelman, D. C. Poppke, and K. A. Piez. Collagen fibril formation. *The Journal of Biological Chemistry*, 253:6578–6585, 1978.

[4] K. G. Vogel and J. A. Trotter. The effect of proteoglycans on the morphology of collagen fibrils formed *in vitro*. *Collagen and Related Research*, 7:105 – 114, 1987.

[5] W. C. Oliver and G. M. Pharr. An improved technique for determining hardness and elastic modulus using load and displacement sensing indentation experiments. *Journal of Materials Research*, 7:1564–1583, 1992.

[6] M. Li, L. Q. Liu, N. Xi, Y. C. Wang, Z. L. Dong, X. B. Xiao, and W. J. Zhang. Atomic force microscopy imaging and mechanical properties measurement of red blood cells and aggressive cancer cells. *Science China Life Sciences*, 55:968–973, 2012.

[7] D. Maugis. Adhesion of spheres: the JKR-DMT transition using a Dugdale model. *Journal of Colloid and Interface Science*, 150:243–269, 1992.

[8] U. D. Schwarz. A generalized analytical model for the elastic deformation of an adhesive contact between a sphere and a flat surface. *Journal of Colloid and Interface Science*, 261:99–106, 2003.

[9] Q. S. Li, G. Y. H. Lee, C. N. Ong, and C. T. Lim. AFM indentation study of breast cancer cells. *Biochemical and Biophysical Research Communications*, 374:609–613, 2008.

[10] G. Lomboy, S. Sundararajan, K. Wang, and S. Subramaniam. A test method for determining adhesion forces and Hamaker constants of cementitious materials using atomic force microscopy. *Cement and Concrete Research*, 41:1157–1166, 2011.

[11] C. Argento and R. H. French. Parametric tip model and force–distance relation for Hamaker constant determination from atomic force microscopy. *Journal of Applied Physics*, 80:6081–6090, 1996.

[12] K. E. Kadler, D. F. Holmes, J. A. Trotter, and J. A. Chapman. Collagen fibril formation. *Biochemical Journal*, 316:1–11, 1996.

Appendix A

Mininum Nanoindentation Method

A.1 JKR versus DMT Models for the Work of Adhesion

There are different models for the adhesion between indenter and sample. The Derjaguin-Muller-Toporov (DMT) model adds a contribution from long-range adhesive forces to the Hertzian model but otherwise keeps the same contact geometry. This results in a calculated adhesive force F_p of

$$F_p = 2\gamma_a \pi R \tag{A.1}$$

The Johnson-Kendall-Roberts (JKR) model takes a slightly different approach, calculating the adhesive forces within the contact area only, but adjusting that area to account for deformation. This results in a calculated adhesive force of

$$F_p = \frac{3}{2}\gamma_a \pi R \tag{A.2}$$

In both cases, γ_a is the work of adhesion per unit area and R is the radius of curvature of the indenter.

From these two ways of calculating γ_a we arrive at two possible equations for the Young's modulus of the same E_s. The DMT model yields

$$E_s = \frac{15}{8}|F_p|R^{-\frac{1}{2}}(\frac{1}{1-{\nu_s}^2})(\Delta d - 2(\frac{AR}{24k})^{\frac{1}{3}})^{-\frac{3}{2}} \tag{A.3}$$

while the JKR model results in

$$E_s = \frac{5}{2}|F_p|R^{-\frac{1}{2}}(\frac{1}{1-{\nu_s}^2})(\Delta d - 2(\frac{AR}{24k})^{\frac{1}{3}})^{-\frac{3}{2}} \tag{A.4}$$

The resulting values for the elastic moduli extracted from the force curves using these two models are collected in Table A.1 for the polycarbonate and low-density polyethylene (LDPE) samples. The JKR model yields more accurate results, but both approaches are reasonable.

Table A.1: Comparison of the elastic modulus calculated with the DMT *vs.* JKR models for the work of adhesion

Material	Calculated E (JKR) (GPa)	Calculated E (DMT) (GPa)	E in literature (GPa)
Polycarbonate	2.7 ± 0.2	2.0 ± 0.15	2.20-2.65[a]
LDPE	0.27 ± 0.06	0.2 ± 0.05	0.2-0.4[b]

[a] V. A. Soloukhin, J. C. M. Brokken-Zijp, O. L. J. van Asselen and G. de With, *Macromol.*, 2003, **36**, 7585–7597.
[b] W. Martienssen and H. Warlimont, *Springer Handbook of Condensed Matter and Materials Data*, Springer, Berlin, 2005.

A.2 Scanning Electron Micrograph of the Indenter

The indenter is spherical at the tip (the portion of the indenter which would be in contact with the sample with our minimal indentation method), as see in Figure A.1. The scanning electron micrograph was obtained with a FEI Quanta 400 at 12.5 kV and 16488X magnification.

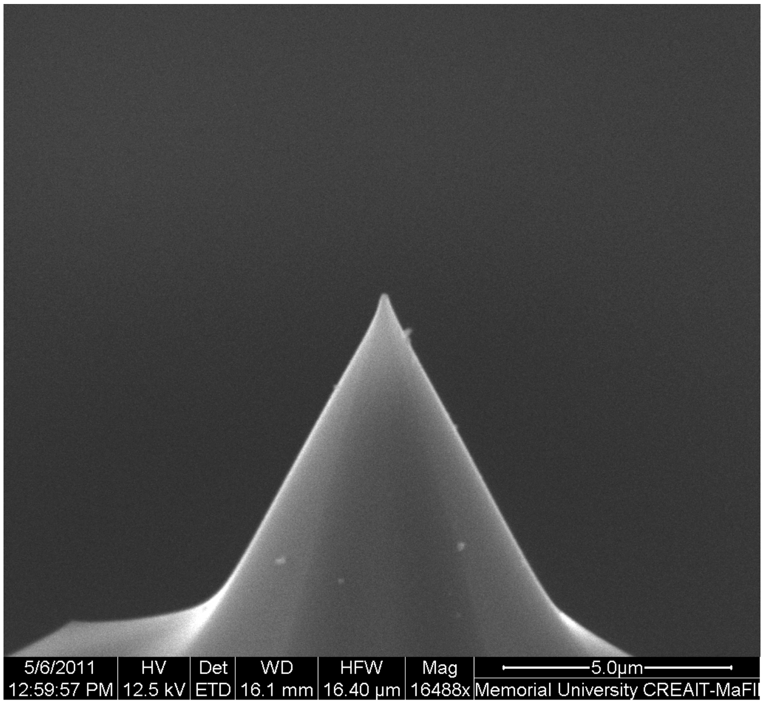

Figure A.1: Scanning electron micrograph of an AFM tip. The spherical profile of the tip is clearly defined. The scale bar is 5.0 μm.

A.3 Creep Test for Viscoelasticity

A creep test was used to check for viscoelastic response, wherein a dwell period follows the initial indentation. During that dwell time the indenter may continue to sink into the sample. This phenomenon is called creep and is associated with viscous, viscoelastic, or viscoplastic samples. After the initial snap to contact the tip load was kept constant while monitoring the indentation depth. This test was performed with an Asylum Research MFP-3D AFM and a CSC17/CR-AU AFM tip from MikroMasch.

In the creep tests, the indentation depth did not change when the indentation pressure was kept constant (Figure A.2, indicating that viscoelastic response can be neglected under our measurement conditions for these materials.

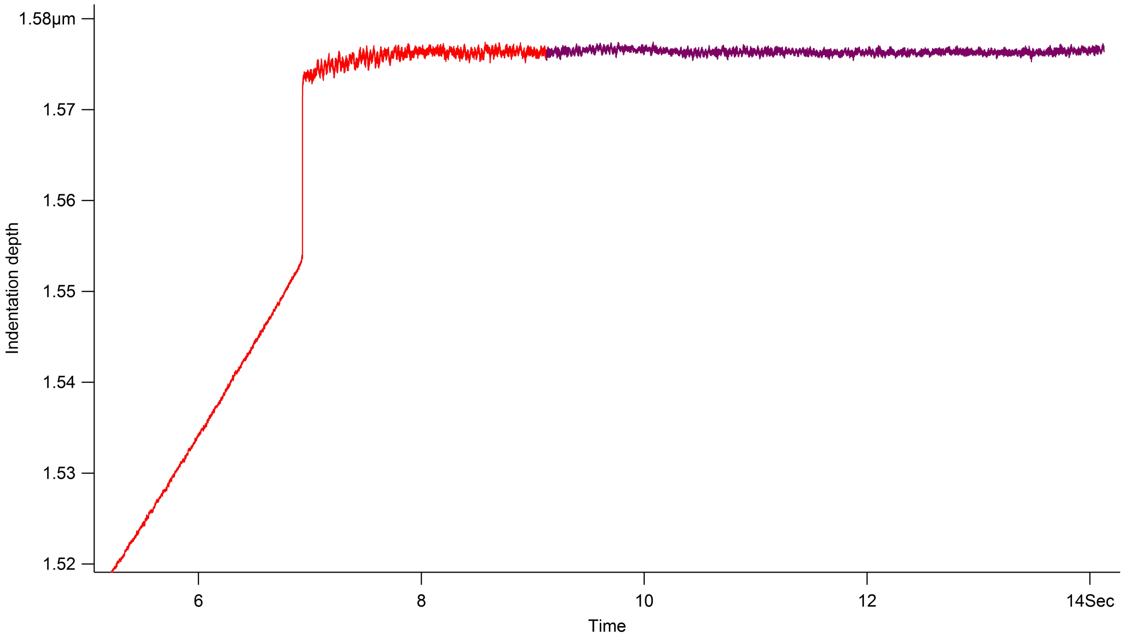

Figure A.2: A typical creep test force curve, this one on LDPE. The red trace shows the indenter approaching the sample surface, snapping into contact with the sample, and then ramping to a predetermined indentation pressure. The purple trace shows the indentation depth versus time when indentation pressure is kept constant.